Dissertation

submitted to the

Combined Faculty of Mathematics, Engineering and Natural Sciences

of Heidelberg University, Germany

for the degree of

Doctor of Natural Sciences

Put forward by

Moto Togawa, M.Sc.

born in: Düsseldorf

Oral examination: 30-01-2025

Spectroscopy on trapped highly charged ions with soft X-ray synchrotron and FEL radiation

Referees: apl. Prof. Dr. José R. Crespo López-Urrutia

apl. Prof. Dr. Jörg Evers

Abstract

Spectroscopic investigation of highly charged ions (HCI) in the X-ray regime enables precise benchmarking of theoretical calculations including effects of bound-state quantum electrodynamics and nuclear origin. It further aids in extracting properties and dynamics of hot astrophysical plasmas by means of plasma modeling. In the framework of this cumulative thesis, an electron beam ion trap has been combined with bright X-ray light sources, such as synchrotrons and X-ray free-electron lasers (XFEL) to investigate HCIs with X-rays of various properties.

In particular, high-precision transition energy measurements of astrophysically relevant diagnostic lines of light lithium-like elements and neon-like iron have been performed with ppm precision, made possible by resolving a key issue in monochromator-based X-ray absorption spectroscopy. These improved transition energy measurements not only allow to test theoretical predictions but also nail down the doppler velocity of astrophysical plasma to few km/s. Furthermore, two techniques for assessing transition oscillator strengths have been developed. A novel synchrotron-based approach using the Hanle effect in the soft X-ray regime for measuring femto- to picosecond lifetimes of allowed transitions in helium-like nitrogen is demonstrated. Second, a pioneering lifetime measurement of femtosecond transitions of helium-like neon and fluorine using an all-X-ray pump-probe technique at an XFEL is presented. Finally, an investigation of well-controlled multi-photon ionization in neon-like krypton producing charge-states well beyond the single-photon ionization limit is presented, which served as a basis for the lifetime measurement.

Zusammenfassung

Spektroskopische Untersuchungen hochgeladener Ionen (HCI) im Röntgenbereich ermöglichen eine präzise Überprüfung theoretischer Berechnungen, einschließlich der Effekte der Quantenelektrodynamik und des nuklearen Ursprungs. Darüber hinaus helfen sie, Eigenschaften und Dynamiken heißer astrophysikalischer Plasmen durch Plasmamodellierung zu extrahieren. Im Rahmen dieser kumulativen Dissertation wurde eine Elektronenstrahlionenfalle mit leistungsstarken Röntgenlichtquellen, wie Synchrotronen und Freie-Elektronen-Lasern (XFEL), kombiniert, um HCIs mit Röntgenstrahlen unterschiedlicher Eigenschaften zu untersuchen. Insbesondere wurden hochpräzise Übergangsenergiemessungen astrophysikalisch relevanter diagnostischer Linien leichter lithiumartiger Elemente und neonartigen Eisens mit ppm-Genauigkeit durchgeführt. Dies wurde ermöglicht, indem ein zentrales Problem der monochromatorbasierten Röntgenabsorptionsspektroskopie gelöst wurde. Diese verbesserten Übergangsenergiemessungen erlauben nicht nur die Überprüfung theoretischer Vorhersagen, sondern bestimmen auch die Dopplergeschwindigkeit astrophysikalischer Plasmen auf wenige Kilometer pro Sekunde genau. Darüber hinaus wurden zwei Techniken zur Bestimmung von Oszillatorstärken entwickelt. Ein neuartiger, synchrotronbasierter Ansatz zur Messung von Lebensdauern im Femto- bis Pikosekundenbereich für erlaubte Übergänge in heliumartigem Stickstoff unter Verwendung des Hanle-Effekts im weichen Röntgenbereich wird demonstriert. Zweitens wird eine neue Lebensdauermessung von femtosekundenkurzen Übergängen in heliumartigem Neon und Fluor mittels einer rein Röntgen-basierten Pump-Probe-Technik an einem XFEL vorgestellt. Schließlich wird eine Untersuchung der kontrollierten Mehrphotonenionisation in neonartigem Krypton präsentiert, die Ladungszustände weit über die Grenze der Einphotonenionisation hinaus erzeugt und die Grundlage für die Lebensdauermessung bildete.

Contents

Chapter 1

Introduction

All things are made of atoms, and everything living things do can be understood in terms of the jigglings and wigglings of atoms.

Richard P. Feynman, The Feynman Lectures on Physics

Since Isaac Newton's famous prism experiments, Fraunhofer's discovery of the enigmatic lines in the spectrum of the sun, since the realization that atoms emit characteristic lines making their spectra figuratively an imprint of themselves, spectroscopy has been established as one of the main techniques in all of science. In pursuit of higher and higher precision and accuracy, countless discoveries have been made.

One of the most important series of discoveries started from the aforementioned spectral observations of the sun by Fraunhofer [1]. He discovered a prominent deep yellow absorption feature marking the spectral landscape produced by the spectrum of the sun. That was in 1814. Many lines have been mapped by Fraunhofer, but only decades later the source of all has been identified by Kirchhoff and Bunsen. Their systematic experiments looked into the characteristic lines produced by elements introduced into a flame [2], observing that some elements do absorb light of the same wavelengths as observed by Fraunhofer decades earlier. This is how the famous sodium D absorption line was identified. With the advent of high-resolution spectrometers, it was found that the sodium D line is in fact a doublet. Another few decades later, in 1925, Uhlenbeck and Goudsmit postulated the existence of an electron spin, very similar to a classical top. This postulation predicted the finestructure of the $3p_{1/2}$ and $3p_{3/2}$ levels. Similar doublet structures have been observed in all alkaline elements although at different wavelengths. The doublet structure of the next lighter alkaline, lithium, would then be caused by the splitting of the $2p_{1/2}$ and $2p_{3/2}$ levels. Precision investigations of these kinds of finestructure splittings are essential as they allow for very accurate tests of theory.

Another series of discoveries started in 1879. Astronomers used the opportunity of a solar

Property	Scaling
Atomic radius	Z^{-1}
Ionization potential	Z^2
Transition energy	Z^2
Finestructure splitting	Z^4
Lamb shift	Z^4
Oscillator strength	Z^0
Radiative transition probability	Z^4

Table 1.1. *List of the scaling behavior of various atomic quantities with respect to the nuclear charge number Z.*

eclipse to study emission of the solar corona, the outermost layer of the sun's atmosphere. Among others, a strong green line at 530 nm was observed. Astronomers were puzzled. At that time, Kirchhoff's and Bunsen's spectral analysis had lead to the identification of most lines in the spectrum of the sun. However, none of the known elements could reproduce the emission of the bright green coronal line. It was therefore considered as line from a hypothetical new element, *coronium*. It took another sixty years until Edlén and Grotian identified that this coronal emission is produced by highly charged ions (HCI). At that time spectroscopic studies of multiply charged ions were limited. But it was already known that certain atomic properties follow a power law with respect to their atomic number, when followed along the isoelectronic sequence (see Tab. 1.1). From a compilation of existing experimental data, Edlén looked into the Z^4 scaling of the finestructure splitting of the $3s^2 3p^2$ doublet (see Fig. 1.1). By extrapolating the known wavelengths of the isoelectronic sequence of aluminum, Edlén determined that the green coronal line matches perfectly well with the emission of the thirteen-fold ionized iron ions. It took time for experimental techniques to catch up with Edlén's predictions, but this marks one of the first spectroscopic observation of highly charged ions.

This highlights how electronic transitions are by no means limited to the neutral elements listed on the periodic table. The remarkable aspect here is that by removing electrons from the nucleus, a new and unique atomic system emerges. There exists an entire *hot periodic table* [3] whose constituents, the highly charged ions, produce unique spectral features that are yet to be fully explored. While one might assume that highly charged ions are rare due to their scarcity on Earth, the majority of matter in the universe is actually highly ionized. Studying the characteristic line emission of highly charged ions across the electromagnetic spectrum is crucial for understanding the ubiquitous sources of such emissions, including the solar corona, accretion disks around black holes, and supernova remnants. The spectral

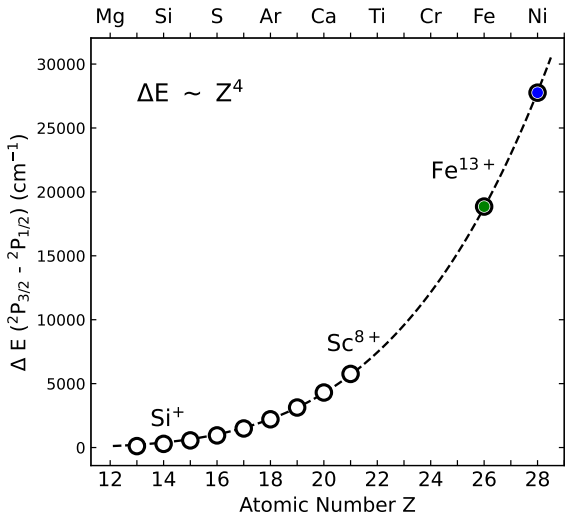

Figure 1.1. *A simplified depiction of the line identification work by Edlén. Precise laboratory measurements of the $3s^2 3p^2$ doublet splitting along the isoelectronic sequence have been combined with the observed wavelength of the coronal lines. The well known power law scaling of the finestructure has been exploited to identify the green coronal line as emission from Fe^{13+}. Data from Ref. [4].*

lines of highly charged ions provide insight into the constituents of the emitting source. By comparing the observed line positions to their rest-frame energies, measured under laboratory conditions on Earth, we can determine the velocity of the emitter, while line ratios offer valuable information about plasma density. These techniques not only enhance our understanding of extraterrestrial light sources, but the pursuit of accuracy and precision also deepens our comprehension of fundamental light-matter interactions.

In the following, I would like to continue with an overview of the research topics, which have been covered within the framework of this thesis. Section 1.1 provides an overview of precision transition energy measurements on HCIs in the (soft) X-ray range. Section 1.2 will be dedicated to lifetime measurements in HCIs. As atomic or ionic lifetimes are generally measured either in the energy domain by means of *natural linewidth* measurements or *lifetime* measurements in the time domain, we highlight their respective strength and weaknesses of both approaches. A different method for obtaining lifetimes exploiting the so-called *Hanle effect* is then discussed in section 1.3. Finally, an introductory section on nonlinear physics in HCIs takes place, highlighting this literally powerful technique's ability to probe transient states, which are not accessible with conventional spectroscopy techniques. Following this introductory chapter, three selected publications covering precision spectroscopy and lifetime measurements on HCIs are presented in Chapter 2. Continuing with a presentation of still unpublished work in Chapter 3 on two studies of HCIs using an X-ray Free Electron Laser. This thesis closes with a discussion and outlook in Chapter 4 and a summary of the results in Chapter 5.

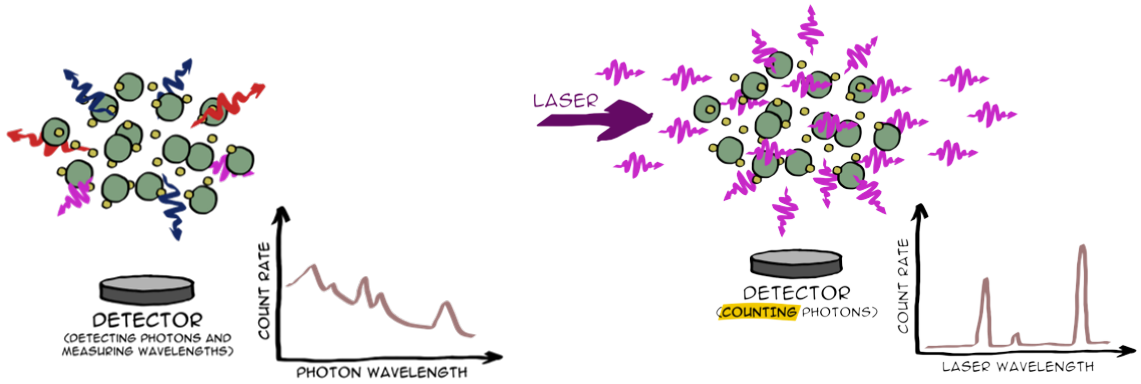

Figure 1.2. *Schematic representation of conventional spectroscopy (left) and laser spectroscopy (right). [Illustration by S. Bernitt]*

1.1 Transition energy measurements in HCIs

Following the isoelectronic sequence to higher and higher atomic numbers at some point leads to an alienation of the spectrum. This well-known phenomenon is caused by to the ways angular momenta of electrons couple to each other when exposed to Coulomb fields of various strengths. At low atomic number Z, i.e. for light elements, so called LS-coupling takes place, while for higher Z, heavier elements spin-orbit interaction takes over and jj coupling schemes do represent the electronic levels in a more suitable way. This transition is paralleled to how the various energy terms in the Dirac Hamiltonian scale with increasing atomic number. The Lamb-shift, which is one way quantum electrodynamics induces their influence to measurable quantities, is known to increase by four orders of magnitude from hydrogen to hydrogen-like uranium. This underlines the effectiveness of spectroscopy of HCIs for improving our understanding of bound-state quantum electrodynamics (BSQED) [5, 6, 7, 8]. Over the past decades, electron beam ion traps (EBIT), electron-cyclotron resonance ion sources (ECRIS) and storage-ring-based spectroscopy have proven to be effective approaches to measure X-ray transitions in HCIs to high accuracy. Storage-ring-based spectroscopy on HCI by means of ion-atom collisions [9, 10] have been reported. For medium-Z elements high spectroscopic accuracies of few of parts per million (ppm) have been obtained by analyzing the emission of HCIs, produced by an ECRIS, with a crystal spectrometers and by using the well-known line positions of helium- and hydrogen-like ions as references. [11].

1.1.1 Reference-free X-ray spectroscopy

Another approach to obtain high-accuracy absolute transition energy measurements are so called reference-free measurement techniques. Two methods, known to provide high-accuracy,

reference-free measurements in the X-ray regime, have been reported. In the first technique, demonstrated by Kubiček *et al.* [12], applies the Bond technique [13] with laser-assisted referencing to precisely determine Bragg reflection angles, culminating in an accuracy of only 1.5 ppm at approximately 3100 eV . Another technique, reported by Amaro *et al.*[14], relates the measured wavelength to the well-known lattice spacing of a silicon crystal, which is then related to the SI definition of the meter by using helium-neon lasers. They report accuracies in transition energy measurements ranging from 2.3 ppm to 6.4 ppm for transition energies between 2400 eV and 3100 eV [15]. As for most crystal- or grating-based spectrometers energy dispersiveness as well as reflective properties drastically decrease below 1 keV, which makes conventional spectroscopy of soft X-ray transitions difficult.

1.1.2 X-ray absorption spectroscopy

First demonstrated by Epp *et al.*[16], over the past almost two decades FEL and synchrotron radiation based spectroscopy techniques on HCIs have been developed. By counting fluorescence photons as a function of the incident photon energy, these synchrotron radiation based measurements do not rely on the energy resolution of the detector (see Fig. 1.2), but on the monochromatic property of the incident radiation, which can be additionally improved by employing a monochromator in the lightpath of the undulator radiation. For absolute transition energy measurement, one can use lines of simple HCIs for precise calibration [17, 18, 19]. Efforts to improve the resolution lead the demonstration of resolving power $E/\Delta E$ of more than twenty thousand [20, 21]. This work revealed that at this level of precision a systematic source of error introduced by the X-ray monochromator can affect the calibration of the photon energy in a noticeable way [22, 23]. It was one of the main motivations for this thesis to address this particular source of error and to reach an improved experimental precision of measured transition energies in the soft X-ray regime, to allow precision benchmarking of state-of-the-art atomic structure predictions [24, 25, 26].

1.2 Lifetime measurements in HCIs

The previous section highlighted the importance of transition energy measurements in HCIs and the prospects of understanding the fundamental interaction of matter and light. However, transition energies, or line positions, are not the only information one can gain from spectra. All spectral lines come in unique intensities, which are of fundamental origin just as their line positions. Line intensities are a direct result of transition probabilities. The higher the line intensity, the more probable a given transition is. These probabilities are quantified by the A coefficient, following a term coined by Einstein. Another, more intuitive, descrip-

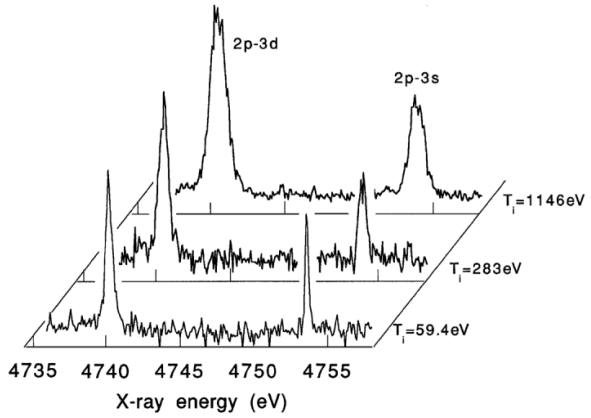

Figure 1.3. *2p - 3d and 2p - 3s transition resolved by an crystal spectrometer. A reduction of the ion temperature leads to noticeable narrowing of both lines. Figure adopted from Ref. [27].*

tion of the line intensity is given by the oscillator strength f. It results from the comparison of the A coefficient to the rate of emission of a classical, single electron oscillator γ_{cl}:

$$f_{21} = -\frac{1}{3} A_{21}/\gamma_{cl}. \tag{1.1}$$

Converting an experimentally measured intensity to the underlying A coefficient is however tedious. For that reason experiments often look into line ratios of two or more line intensities. This is a quantity, which can be easily compared to its respective theoretically predicted value. In cases, where line ratios do not provide the sought out information, one has to measure the transition probability with other approaches. A concept often used is not far away from the classical, single electron oscillator. The radiative decay process can be described in terms of a damped oscillator. The dampening is linked to the decay rate or *lifetime*, which is the inverse of the Einstein A coefficient (assuming a two-level system, i.e. no other competing decay channels). Furthermore, the damped oscillator is closely connected to a Lorentzian line shape with a width, referred to as the *natural line width*.
In the following, a review of available techniques to measure lifetimes focusing on applications in the (soft) X-rays is presented. Their individual strengths and limitations are highlighted.

1.2.1 Linewidth measurement

The natural linewidth Γ is closely connected to the lifetime τ of a state through the well-known Heisenberg uncertainty principle $\Gamma \cdot \tau = \hbar$. The inverse relationship of the natural linewidth and the lifetime makes linewidth measurement especially suited for fast decaying transitions, for which τ is too small for direct observation, but Γ becomes large. A pioneering experiment in this field has been presented by Beiersdorfer *et al.* [27]. Neon-like Cs ions have been produced and trapped in an EBIT. The energy of the electron beam was set sufficiently high to allow efficient production of the target ions as well as to collisionally populate the $3d_{5/2}$ level. Those excited ions relax mainly by an E1 transition to the $2p_{3/2}$

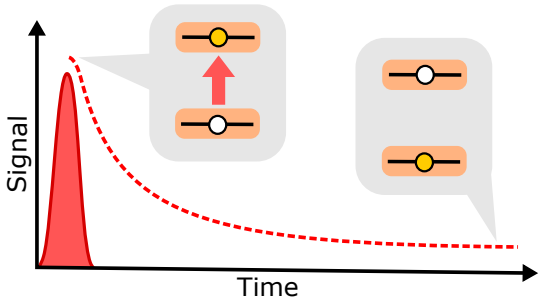

Figure 1.4. *Schematic view of a lifetime measurement by means of electronic timing. The exponential decay of a quasi instantaneously populated state is monitored until the entire population has decayed.*

level by emission of a fluorescence photon. The experiment utilized a crystal spectrometer to measure the line. The recorded lineshape comprises not only of the natural linewidth but also the instrument profile (response function) and the thermal broadening. The key to the successful measurement of the natural linewidth was therefore the application of evaporative cooling by decreasing the electrostatic trapping potential of the EBIT allowing hot ions to be passively removed from the trap. This resulted in a resolving power E/E_{FWHM} of approximately twenty thousand (see Fig. 1.3).

Other methods employ spectroscopy with synchrotron radation [28, 20], which is technically equal to what has been discussed in the previous section. Since highly monochromatized synchrotron radiation does not only increase accuracy of centroid determination, but also allow to resolve the natural linewidth. Effectively hitting two targets with one arrow. These techniques work well for few femtosecond down to attosecond lifetimes. Their corresponding linewidth ranges in the hundreds of meV range, which can be resolved. Limitations of this technique appear when lifetimes surpass tens of femtoseconds. First of all, their associated natural widths are found in the meV range, resolving power of more than one hundred thousand become necessary. Such high resolutions have not been demonstrated so far. Furthermore, the contribution of instrumental and thermal broadening dominates the line profile near the centroid. To observe the Lorentzian wings, one must look farther away from the centroid, where these broadening effects are less significant. This requires a very high signal-to-noise ratio to clearly detect the wings, as they are subtle and can easily be obscured by noise [20].

1.2.2 Electronic timing

Longer lived levels must be approached by other means. In the following, we will discuss lifetime measurements performed in the time domain, i.e. recording the characteristic exponential decay of a selected excited population. A population can be selectively excited by using a short laser pulse to transfer part of the population to an excited state (see Fig.1.4). A recent example of selective excitation in a time-resolved lifetime measurement has been presented by Kimura *et al.* [29] who measured a 3.80 (38) ns lifetime of an E1 transition at

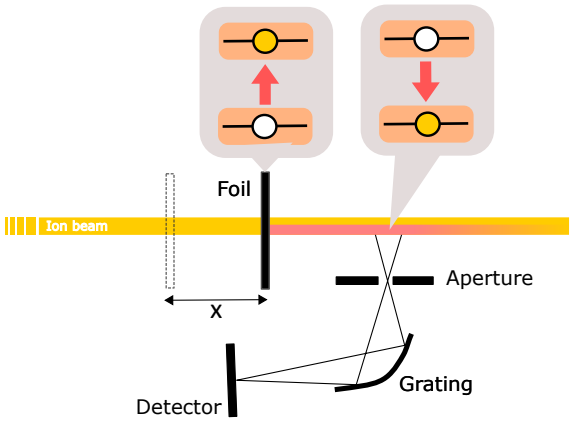

Figure 1.5. *Schematic view of a Beam-foil Spectroscopy set-up. A relativistic ion bunch passes through a thin foil. A fraction of the ions leave the foil excited. The fluorescence emitted by the decaying ions is recorded at a fixed position along the beam trajectory. The decay can be tracked by displacements of the foil.*

approximately 30 eV. The authors used a few-nanosecond long optical pulse tuned to resonantly transfer population to the target state. Synchronously with the incoming pulse, a photo sensitive detector (PSD), set-up behind a grating, records XUV spectra from ions inside the EBIT in a time-resolved manner. Similar techniques have been reported in the optical [30] as well as X-ray regime, using the electron beam itself to populate the ions of the target charge and excited state and by employing magnetic trapping (i.e. turning off the electron beam) during fluorescence detection [27, 31, 32, 33, 34, 35, 36]. The short-time limit for this technique is given by the time resolution of the detection, which is typically on the order of a few nanoseconds.

1.2.3 Beamfoil spectroscopy

Even faster transitions can be measured by means of beamfoil spectroscopy [34]. This technique is performed exclusively in ion storage ring facilities, where ions are accelerated to relativistic speed. These ions are sent through a thin (typically carbon) foil which alters the ionization balance within the ion bunch and can also leave ions in excited states. As soon as the ions leave the foil, the excited population starts their decay process. A spectrometer placed at a fixed position, as depicted in Fig. 1.5, records fluorescence. Key to this technique is that the decay curve is spatially mapped on top of the ion beam trajectory. Therefore, linear displacements of the foil along the beam trajectory will lead to a exponential decrease of the signal detected. The short-time limit hampering the electronic timing technique is lifted by not measuring the decay curve in ”one go”, but by sampling the decay curve in consecutive measurements. This technique is limited by the mechanical translation of the foil. Accurate movements can be achieved down to few micrometers, which corresponds to few picoseconds in time-of-flight [37].

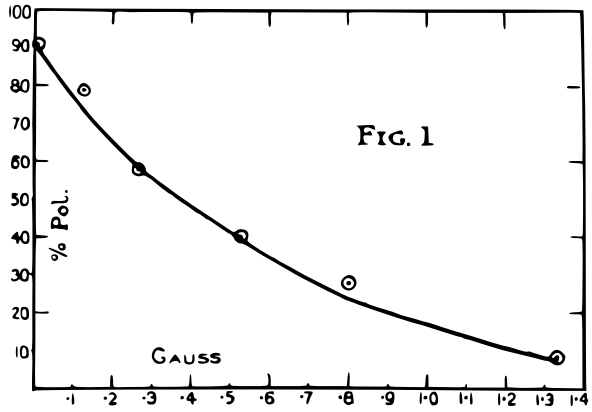

Figure 1.6. *First (Hanle) curve recorded by Wood and Ellet [42]. Percentages of polarization are shown as a function of fractions of a Gauss. Polarization is recovered at zero Gauss. Minute increases in the external field rapidly decrease the degree of polarization.*

1.2.4 Pump-probe spectroscopy

Thus far, we have discussed various techniques that enable the measurement of atomic lifetimes across a broad spectrum. However, we lack methods to measure lifetimes that fall between those accessible by linewidth measurements ($\tau <$ fs) and beam-foil techniques ($\tau >$ ps). This leaves a gap spanning three orders of magnitude, where, to the best of my knowledge, no successful lifetime measurements of X-ray transitions have been performed. One approach, known to offer the necessary time resolution to cover this range, is pump-probe spectroscopy [38, 39]. A technique involving two light pulses, where a dynamic process is initiated in an atomic, ionic, or molecular target by a short laser pulse. The temporal evolution of the system after a waiting period is probed by a second laser pulse. Repeating this process for different waiting times between the two pulses allows to fully recover the time evolution of the system investigated. This has been up to now mostly limited by the available laser frequencies, such that the development of high-harmonic generation allowed to realize pump-probe experiments with *attosecond resolution* in the XUV range. For X-ray transitions, there are no cavity-based lasers due to a lack of normal-incidence mirrors which offer the right reflective and transmissive properties. In recent years, so-called X-ray free electron lasers have been developed, which provide the right properties for their application to pump-probe measurements for ultrafast dynamics [40, 41]. We present a first successful electronic lifetime measurement by means of an all X-ray pump-probe experiment in Chapter 4.

1.3 Hanle effect

At a similar time when Uhlenbeck and Goudsmit postulated the existence of the electron spin, a young (PhD) student named Wilhelm Hanle was working in the laboratory of James Frank on an experiment, which is now regarded as one of the key experiments bridging the gap between old quantum theory and modern quantum theory. He was studying a, at the

time, perplexing phenomenon of resonance fluorescence and their associated polarization. Decades earlier Wood [43] discovered that light resonantly scattered from atomic mercury vapor under an angle of ninety degrees is completely unpolarized. Interestingly, a similar experiment conducted by Lord Rayleigh in 1922 [44] showed contradicting results, as the scattered light kept some of their initial polarization. Wood and Ellet [42] again considered this puzzle and discovered that the different polarization degrees did depend on the orientation of the experiment with respect to the earth's magnetic field. After compensating the external field by means of a solenoid, the observed scattered light was almost completely polarized as it is the case for nonresonantly scattered light (Rayleigh Scattering). Hanle initially provided a first classical explanation relating the excitation of the magnetic sublevels to oscillations of the electron. The classical model allowed for some kind of understanding of the effect, but could not be seamlessly brought together with old quantum theory, as in it quantum systems could only exist in pure states. To fully explain the effect, it required the introduction of the concept of *coherent excitation*, allowing for interference of the two magnetic sublevels if the spacing of the levels is of the order of h/τ. By varying the magnetic field the overlap of the levels can be arbitrarily adjusted, thereby so-called Hanle-curves are obtained (see Ref. 1.6). While the Hanle effect has primarily been considered in the literature as a method for measuring optical transitions, the advent of high-resolution lasers has shifted attention toward more versatile laser spectroscopy techniques. However, in the (soft) X-ray regime, the Hanle effect has been revisited as a valuable tool in a demonstration experiment to measure picosecond lifetimes.
Publication 3 in Chapter 3 presents this novel way of using the Hanle effect without the need to tune the magnetic field.

1.4 Nonlinear spectroscopy

With the advent of X-ray free electron lasers, ultra-intense and ultra-short X-ray pulses have been made available. In combination with micrometer-level focusing ability, the probability of atoms absorbing several photons per pulse can be close to one [45]. One is not limited to do spectroscopy on transitions involving the groundstate (or metastable states). The conditions present at XFELs allow the production and interaction with transient states on very short time scales [46, 47]. These studies enable to test atomic theory in multiply excited states, which are essential for all kinds of precision calculations based on configuration interaction methods, which are only scarcely studied experimentally due to their complexity. By understanding and controlling these ultrafast ionization processes, one could minimize radiation damage, which a key limitation in many XFEL based experiments as for example in imaging of biologically relevant macromolecules [48].

Chapter 2

Selected publications

The first two publications in Sections 2.1 and 2.2 address precision transition energy measurements using soft X-ray synchrotron radiation (see Chapter 1.1.2). The third publication, presented in Section 2.3, introduces a novel method for lifetime measurements based on the Hanle effect (see Chapter 1.3).

2.1 High-accuracy measurements of core-excited transitions in light Li-like ions

A general systematic uncertainty affecting monochromator based soft X-ray spectroscopy has been characterized and corrected. This resulted in a spectroscopic accuracy for light lithium-like ions that is comparable to current *ab initio* predictions. The article was published in *Physical Review A*.

AUTHORS **Moto Togawa**, Steffen Kühn, Chintan Shah, Vladimir A. Zaytsev, Natalia S. Oreshkina, Jens Buck, Sonja Bernitt, René Steinbrügge, Jörn Seltmann, Moritz Hoesch, Christoph H. Keitel, Thomas Pfeifer, Maurice A. Leutenegger, José R. Crespo López-Urrutia
PUBLICATION STATUS Published 4 September 2024

JOURNAL REFERENCE Phys. Rev. A 110, L030802

DIGITAL OBJECT IDENTIFIER https://doi.org/10.1103/PhysRevA.110.L030802

AUTHOR'S CONTRIBUTIONS **MT** and SK prepared and organized the experiment. **MT**, SK, CS, SB, RS and JRCLU took the data. JB, JS, MH operated the synchrotron radiation beamline. **MT** analyzed the data. **MT** and JRCLU wrote the manuscript. VZ and NO per-

formed theoretical calculations. All authors took part in the critical review of the manuscript before and after submission.

ABSTRACT The transition energies of the two $1s$-core-excited soft X-ray lines (dubbed *q* and *r*) from $1s^2 2s^1 S_{1/2}$ to the respective upper levels $1s(^2S)2s2p(^3P)^2P_{3/2}$ and $^2P_{1/2}$ of Li-like oxygen, fluorine and neon were measured and calibrated using several nearby transitions of He-like ions. The major remaining source of energy uncertainties in monochromators, the periodic fluctuations produced by imperfect angular encoder calibration, is addressed by a simultaneously running photoelectron spectroscopy measurement. This leads to an improved energy determination of 5 parts per million, showing fair agreement with previous theories as well as with our own, involving a complete treatment of the autoionizing states studied here. Our experimental results translate to an uncertainty of only 1.6 km/s for the oxygen line *qr*-blend used to determine the outflow velocities of active galactic nuclei, ten times smaller than previously possible.

Letter

High-accuracy measurements of core-excited transitions in light Li-like ions

Moto Togawa,[1,2,3,*] Steffen Kühn,[1] Chintan Shah,[4,5,1,†] Vladimir A. Zaytsev,[1] Natalia S. Oreshkina,[1] Jens Buck,[6] Sonja Bernitt,[7,8,9,1] René Steinbrügge,[10] Jörn Seltmann,[10] Moritz Hoesch,[10] Christoph H. Keitel,[1] Thomas Pfeifer,[1] Maurice A. Leutenegger,[4] and José R. Crespo López-Urrutia[1,‡]

[1]*Max-Planck-Institut für Kernphysik, Saupfercheckweg 1, 69117 Heidelberg, Germany*
[2]*European XFEL, Holzkoppel 4, 22869 Schenefeld, Germany*
[3]*Heidelberg Graduate School for Physics, Ruprecht-Karls-Universität Heidelberg, Im Neuenheimer Feld 226, 69120 Heidelberg, Germany*
[4]*NASA/Goddard Space Flight Center, 8800 Greenbelt Road, Greenbelt, Maryland 20771, USA*
[5]*Center for Space Sciences and Technology, University of Maryland, Baltimore County, 1000 Hilltop Circle, Baltimore, Maryland 21250, USA*
[6]*Institut für Experimentelle und Angewandte Physik, Christian-Albrechts-Universität zu Kiel, Kiel, Germany*
[7]*GSI Helmholtzzentrum für Schwerionenforschung, Planckstraße 1, 64291 Darmstadt, Germany*
[8]*Helmholtz Institute Jena, Fröbelstieg 3, 07743 Jena, Germany*
[9]*Institute for Optics and Quantum Electronics, Friedrich Schiller University Max-Wien-Platz 1, 07743 Jena, Germany*
[10]*Deutsches Elektronen-Synchrotron (DESY), Notkestrasse 85, 22607 Hamburg, Germany*

(Received 18 October 2023; revised 28 May 2024; accepted 7 August 2024; published 4 September 2024)

The transition energies of the two $1s$ core-excited soft x-ray lines (dubbed q and r) from $1s^2 2s\ ^1S_{1/2}$ to the respective upper levels $1s(^2S)2s2p(^3P)\ ^2P_{3/2}$ and $^2P_{1/2}$ of Li-like oxygen, fluorine, and neon were measured and calibrated using several nearby transitions of He-like ions. The major remaining source of energy uncertainties in monochromators, the periodic fluctuations produced by imperfect angular encoder calibration, is addressed by a simultaneously running photoelectron spectroscopy measurement. This leads to an improved energy determination of 5 parts per million, showing fair agreement with previous theories as well as with our own, involving a complete treatment of the autoionizing states studied here. Our experimental results translate to an uncertainty of only 1.6 km/s for the oxygen line qr blend used to determine the outflow velocities of active galactic nuclei, ten times smaller than previously possible.

DOI: 10.1103/PhysRevA.110.L030802

High-resolution grating spectrometers onboard the Earth-orbiting x-ray telescopes Chandra and XMM-Newton have enabled the detection of inner-shell x-ray absorption lines in ionized outflows of active galactic nuclei (AGN) and the neutral interstellar medium (ISM) and warm-hot intergalactic medium (WHIM) [1–4]. They reveal the physical conditions of the ionized absorbing medium, among others the velocities of outflows, plasma densities, and temperatures [5–7]. The strongest $1s$-$2p$ inner-shell absorption lines of light Li-like ions (referred to as q, r, following the notation of Gabriel) are among the most important lines observed in such environments. However, inaccurate transition energies introduced systematic uncertainties, e.g., discrepancies of up to 1.3 eV, have been seen in predictions of q and r of oxygen at ∼560 eV. This caused a velocity uncertainty of 700 km/s, as large as the outflow velocities in nearby active galaxies, which hampered the understanding of multicomponent outflows [8,9]. Uncertain transition energies also hindered the disentanglement of absorption from different charge states of oxygen in the ISM [10]. Experiments at the Lawrence Livermore National Laboratory Electron Beam Ion Trap (LLNL EBIT) [11] reduced the uncertainty to 20–40 km/s, but individual core-excited fine-structure levels were not resolved. The q and r lines of Ne^{7+} have also been proposed as electron-density diagnostics in flares of stellar coronae, but suffer both from their overlap with L-shell lines from iron and theoretical uncertainties [12]. Similar problems occur with the x-ray lines q and r emitted following dielectronic recombination of heliumlike ions needed for determining electron densities and temperatures in magnetically confined fusion plasmas [12–14]. The utility of the aforementioned cases depends on the quality of the utilized atomic data.

Unfortunately, Li-like ions still challenge contemporary calculations, which have uncertainties at the few-meV level for core-excited levels [15–18], far greater than in H-like and He-like systems [19,20]. With few exceptions [21,22], earlier x-ray measurements could not benchmark predictions [23] of the core-excited states [$1s(^2S)2s2p(^3P)\ ^2P_{3/2}$ and $^2P_{1/2}$] due to limited resolution [11,24–26]. Machado *et al.* [21] and Schlesser *et al.* [22] used for q and r in Ar and S a crystal

*Contact author: togawa@mpi-hd.mpg.de
†Present address: Department of Physics and Astronomy, Johns Hopkins University, Baltimore, Maryland 21218, USA.
‡Contact author: crespojr@mpi-hd.mpg.de

spectrometer with a resolving power of ∼12 000, achieving a wavelength accuracy better than 2–5 ppm, but at energies below 1 keV available crystals and gratings offer neither enough reflectivity nor resolving power. Other experiments using merged beams of ions and photons [27] were limited by insufficiently accurate calibrations with molecular x-ray absorption spectra [28,29]. Systematic uncertainties were recently substantially reduced down to 15 ppm by using $1s$-np transitions in He-like ions to independently recalibrate molecular transitions [30,31]. State-of-the-art soft x-ray monochromators with resolution exceeding 20 000 [32] still suffer from calibration problems resulting from periodic errors of angular encoders in use [33].

In this Letter, we present measurements at the P04 beamline of the PETRA-III storage ring in Hamburg, Germany [34] resolving the q and r lines in Li-like oxygen, fluorine, and neon, and yielding transition energies with an accuracy of approximately 5 ppm. A more than tenfold improvement was made possible by mitigating systematic fluctuations of angular encoders by simultaneous high-resolution photoelectron spectroscopy (XPS). Our accurate measurements benchmark predictions accounting for electron-electron correlation, QED, and nuclear size effects, as well as general and specific relativistic mass shifts. Moreover, we provide accompanying large-scale calculations, which exhibit theoretical uncertainties on par with state-of-the-art predictions while taking the effect of autoionization shifts into account [18]. We thereby provide both experiment and theory to test and benchmark the state-of-the-art calculations of Li-like theory for a few selected elements. We acquire absorption spectra by scanning the incident photon energy while counting the number of fluorescence photons after resonant excitation, which are detected by silicon-drift detectors (SDDs). At P04 [34], a photon beam of $10^{14}\gamma/s$ at 0.1% bandwidth is generated by an undulator, which after monochromatization and transport losses results in an approximately $10^{11}\gamma/s$ flux at the focus, which is placed at center of our compact electron beam ion trap, PolarX-EBIT [35]. The ions are produced by PolarX-EBIT, by injecting a tenuous atomic or molecular beam containing the element of interest. It crosses the electron beam, which is focused by a magnetic field and set to an energy sufficient to generate and trap the respective He-like and Li-like ions, but below their K-shell excitation threshold. This ensures a good signal-to-noise ratio in the silicon-drift detectors, which are equipped with 500-nm aluminum filters for blocking most of the low-energy stray light. Both detectors are mounted side-on for registering soft fluorescence x rays produced by electron impact and, crucially, upon resonant photoexcitation. This method was demonstrated at the free-electron laser FLASH as soft x-ray laser spectroscopy [36] and later also applied at synchrotron-radiation facilities [30,33,37–42].

After optimizing the monochromator using the strong, narrow w ($1s2p\ ^1P_1$ to $1s^2\ ^1S_0$) line of oxygen [32] to achieve a resolving power of more than 30 000, we can resolve q and r. We then scan several times in discrete monochromator steps of nominal energies a range containing the q and r transitions of the Li-like ion, and calibration lines including the w line of the He-like ion of the same element, as well as a short series of $1s^2$ to $1snp$ transitions of the next lower element in atomic number.

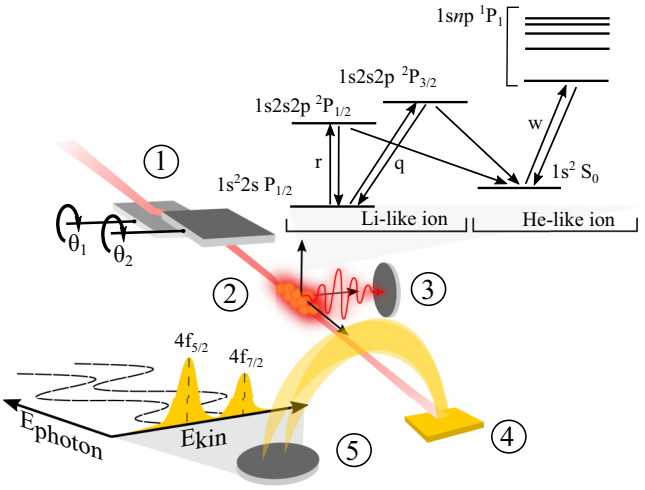

FIG. 1. Scheme of our experiment. Passing a monochromator (1) photons are focused onto the trapped HCI (2), with the relevant transitions and energy levels indicated. Fluorescence photons following resonant excitation due to the incident photon beam are recorded by a SDD (3). The outgoing beam continuously generates photoelectrons from a gold target (4). A PES resolves the two prominent $4f$ lines on a detector (5) to monitor energy fluctuations.

Knowing the actual photon energy depends on accurate readings of grating and mirror angles (θ_1, θ_2 in Fig. 1) in the monochromator. Angular encoders measure them by the transmission of light between several glass disks patterned with opaque marks that overlap only at certain rotation-angle steps. While the narrow linewidth of the recorded transitions calls for steps of roughly 4×10^{-5} deg, the spacing between the 36 000 reference marks of the Heidenhain RON 905 encoders used in the P04 monochromator delivers only 10^{-2}-deg dark-bright cycles. Between those marks, encoders interpolate the angle changes 1000-fold using the quadrature signals of several diodes measuring the light modulated by minor disk rotations. This procedure is very sensitive to imperfections of those analog signals, and thus empirical look-up tables have to be regularly generated and stored in the hardware. However, residual errors remain. Previous observations at P04 and beamlines elsewhere showed that nominal photon energies calculated from such interpolated readouts had periodic subdivisional errors [43,44], leading to fluctuations in the photon-energy readout. With two encoders needed to measure the diffraction angle, a double interpolation uncertainty should affect most x-ray monochromators worldwide [43,44]. As we will discuss in the following, periodic changes with peak-to-peak amplitudes of up to 70 meV have been found in our case.

Since the off-axis electron gun of PolarX-EBIT lets the photon beam exit downstream unimpeded, we perform XPS [45] measurements for monitoring fluctuations of the actual photon-beam energy (see Fig. 1). The hemispherical photoelectron spectrometer (PES), ASPHERE [46], is permanently installed at P04 several meters downstream of the open port where PolarX-EBIT is mounted. After passing through it, the photon beam illuminates a gold target mounted in PES that is electrostatically biased, where photoelectrons are

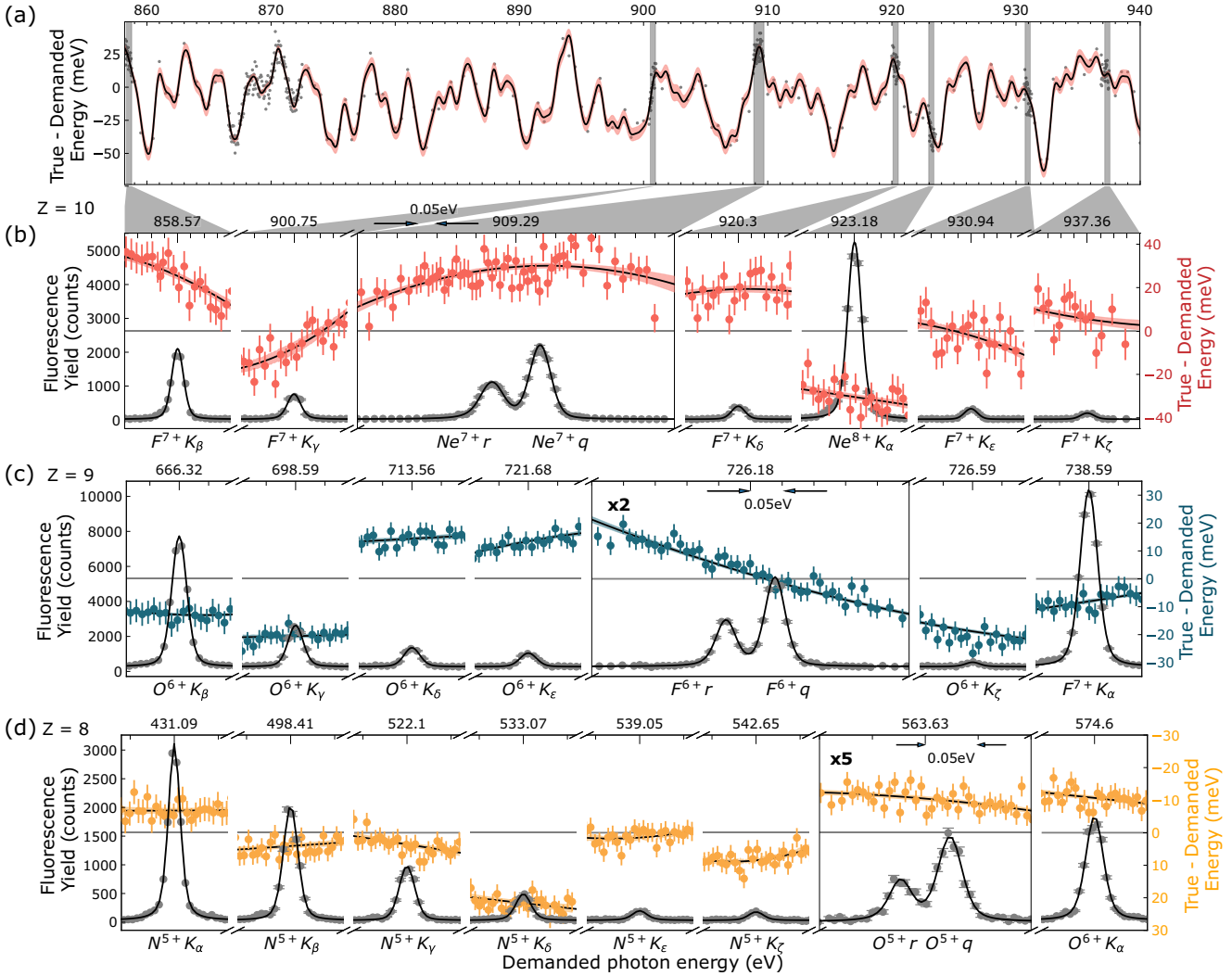

FIG. 2. (a) Trace of energy deviations recorded by means of XPS of Au $4f_{5/2}$ photoelectrons. The trace covers the energy range of the Li-like neon q and r measurement. (b)–(d) Example scans of q and r lines for neon, fluorine, and oxygen and respective calibration lines are superimposed with their, simultaneously acquired, photoelectron trace, which monitors the deviations of the demanded photon energy from the actual energy. Each scan contains the resolved q and r transitions of the Li-like ion, as well as various He-like calibration lines.

emitted from the Au $4f_{5/2,7/2}$ states known for their large cross sections [45,47,48] with a kinetic energy given by $E_{\mathrm{kin}} = E_\gamma - E_{4f} + V_{\mathrm{bias}}$. While V_{bias} is scanned on par with the nominal photon energy in order to keep E_{kin} nominally constant, PES selects $4f_{5/2,7/2}$ photoelectrons within a narrow ($\approx$ 15 eV) range encompassing both states, and guides them to a microchannel-plate-amplified phosphor screen imaged on a camera. This high selectivity together with the short-term stability of ASPHERE allows us to monitor periodic energy fluctuations from the nominal, linearly growing energy of each scan.

While the $4f_{5/2,7/2}$ photoelectron peaks should have fixed positions at the detector, actual energy fluctuations induce small centroid shifts of both peaks. After projection of the detector image onto its dispersive axis, we continuously monitor them with a few meV statistical uncertainty by fitting two Voigt peaks and a linear background. Alternative fit models did not significantly improve the fits. During photon energy scans, the $4f_{5/2,7/2}$ peaks' oscillations [see Fig. 2(a)] reflect the interpolation inaccuracies of the two angular encoders. Two distinct oscillation periods arise from the different distances of the mirror and grating to the undulator x-ray source and exit slit. This recording yields the photoelectron traces used for correction. To calibrate the kinetic-energy range covered by these traces on the photoelectron detector image, we scan the bias voltage at a constant photon energy, shifting the $4f_{5/2,7/2}$ peaks across the detector. Subsequently, traces are locally modeled at resonances using low-degree polynomials within narrow energy windows (see Fig. 2), and added as corrections to the nominal, yet uncalibrated, photon energy scale derived from the monochromator-angle readout. Using this modified scale, the centroids of the highly charged ion (HCI) fluorescence resonances are determined by fitting Voigt functions. Under the present experimental conditions, we see several sources comprising Gaussian and Lorentzian components, respectively. We associate the Gaussian contribution with the inherent limitations in resolution of the monochromator and the thermal motion of

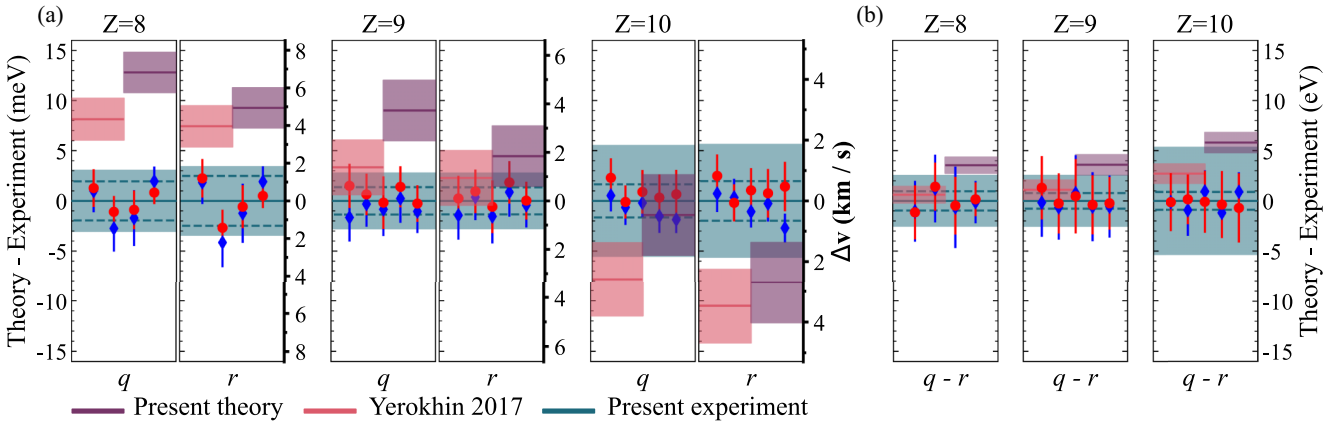

FIG. 3. Comparison of our results with theory from Refs. [15,16]. Theory-experiment energy difference of q and r (a) and their fine-structure splitting (b). Dashed lines mark experimental 1-sigma uncertainties, excluding those of our XPS data. The area shaded in green includes all uncertainties. Predictions and uncertainties of Refs. [15,16] as well as of our calculations are shaded in red and purple, respectively. The bold right-side axes in (a) show the accuracy in units of km/s, corresponding to the uncertainty of the AGN-outflow velocity.

the ions. The Lorentzian width, as shown in Ref. [33], stems from the finite lifetime of the excited levels and the pseudo-Lorentz instrumental component due to x-ray diffraction at the beamline components [44]. For absolute calibration of the photon energy in each scan, we assign to the measured positions of the He-like transitions predicted energy values from Ref. [19], and fit the corresponding dispersion curves using linear functions, except for q and r of Li-like oxygen, where a second-order polynomial was needed.

We found a systematic shift in the energies of q and r depending on whether the correction was derived from the Au $4f_{7/2}$ or the $4f_{5/2}$ peak (blue and red data points in Fig. 3). By taking a weighted average of these individual results, we find this shift being largest for neon with approximately 1.8 meV, for fluorine 1 meV, and negligible for oxygen measurements, and take it into account with an accordingly enlarged systematic uncertainty. These uncertainty bands are depicted as dashed lines in Fig. 3. Repeated XPS measurements also revealed a broader distribution of $4f_{7/2}$, $4f_{5/2}$ centroids than statistically expected, which we attribute to instabilities in the voltage sources of PES. We estimate this systematic error from the distribution widths found respectively as 5.3, 2.4, and 2.3 meV for Ne, F, and O and add it in quadrature to the total. See Supplemental Material [49] for details on error estimation.

We then compare the measured energies of q and r with high-precision calculations of both the ground state and the excited $1s2s2p$ states, including contributions from electronic correlations, quantum electrodynamics (QED), and nuclear recoil. Since the excited states can decay via electron emission, a so-called Auger-Meitner channel (see Fig. 1), they do not have square integrable wave functions. For this reason, the energies of autoionizing states can exhibit a strong dependence on the basis set parameters, which limits the accuracy of the standard high-precision approaches such as the configuration interaction (CI) or coupled cluster. To properly account for the energy shift resulting from the Auger-Meitner channel [50], we have used the complex scaling method [18,51–53] to evaluate the energies of $1s2l2l'$ levels of Li-like oxygen, fluorine, and neon with extended configuration space.

In Table I and Fig. 3, we compare the experimental data and our calculations with the existing predictions of Yerokhin *et al.* [15] based on the basis-balancing method for the treatment of the autoionization channel. For all elements, our theoretical values for the q and r transitions show a shift of ∼5 and ∼2 meV, respectively, from those of Refs. [15,16]. Although our complex rotation method is better suited for the complete treatment of states with autoionization channels, our experiment shows overall better agreement with Ref. [15]. It is interesting to note that both predictions of fine-structure splitting, i.e., the differences between q and r, agree well with our experiment. This suggests that the likely cause of the discrepancy observed in the absolute energy comparison may be due to electron correlation effects rather than the QED corrections.

Figure 4 compares our results with predictions and measurements of the unresolved oxygen qr blend of other works. We also include earlier predictions from Vainshtein and Safronova [54] showing one significant digit more

TABLE I. Measured energies of the $1s2s2p\ ^2P_{3/2}$ (q) and $1s2s2p\ ^2P_{1/2}$ (r) transitions, derived center of gravity (c.g.), and differences from predictions. All values are given in eV.

		This work		Refs. [15,16]
Element		Expt.	Theory	Theory
$Z=8$	q	563.0712(30)	563.084(2)	563.079(2)
	r	563.0257(34)	563.035(2)	563.033(2)
	c.g.	563.0560(23)		563.064(2)
	q-r	0.0456(25)	0.0492(8)	0.0463(8)
$Z=9$	q	725.3720(28)	725.381(3)	725.375(3)
	r	725.2945(28)	725.299(3)	725.297(3)
	c.g.	725.3462(21)		725.349(3)
	q-r	0.0774(25)	0.081(1)	0.079(1)
$Z=10$	q	908.2019(55)	908.200(4)	908.194(4)
	r	908.0796(57)	908.071(4)	908.069(4)
	c.g.	908.1607(41)		908.151(4)
	q-r	0.1222(53)	0.128(1)	0.125(1)

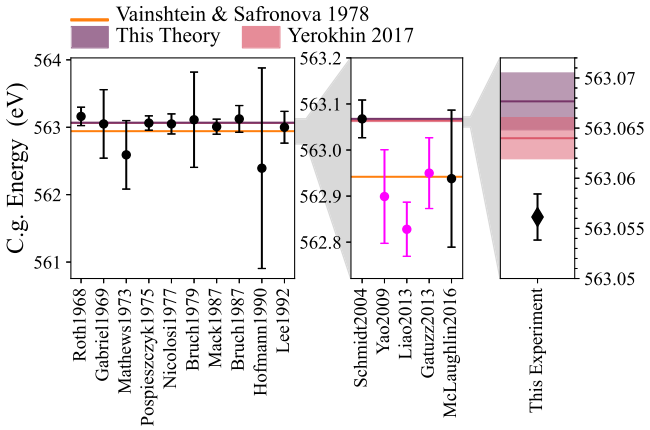

FIG. 4. Experimental values for the center-of-gravity energy of the blended *qr* line of Li-like oxygen [11,23,27,57–59,63–72]. Astrophysical observations (magenta circles); predictions and their uncertainties: Refs. [15,16] (red); this work (purple); Ref. [54] (orange).

than other theoretical works [8,55,56]. Interestingly, the center-of-gravity value of 562.9419 eV by Vainshtein and Safronova [54] agrees better with astrophysical observations [57–59] than other laboratory measurements. However, both our theoretical and experimental results align more favorably with Refs. [15,16].

By combining soft x-ray laser spectroscopy of accurately *ab initio* predicted narrow He-like transitions with synchronous XPS measurements, we eliminate encoder interpolation errors generally affecting energy determinations with monochromators, and solve a long-standing problem of such devices. Thus, our soft x-ray energy measurements below 1 keV are the most accurate to date. For the studied low-Z elements, electronic correlations are dominant. Nonetheless, QED effects in these autoionizing systems cause shifts carrying theoretical uncertainties as large as those of Dirac-Coulomb-Breit terms. Understanding these enables more robust tests of QED theory and mass-shift contributions in strong fields using heavier ions, where correlation effects become smaller. Furthermore, our results recalibrate earlier works, and immediately benefit *XRISM* [60], a recently launched x-ray observatory furnished with a high-resolution x-ray microcalorimeter. Additionally, our data provide accurate reference lines, which allow full utilization of upcoming x-ray observatories such as *Athena* [61] and *Arcus* [62], which have a targeted resolving power of 1000–3500 and an uncertainty of below 10 km/s, and call for high-accuracy rest wavelength standards of essential soft x-ray transitions.

Financial support was provided by the Max-Planck-Gesellschaft (MPG) and Bundesministerium für Bildung und Forschung (BMBF) through Project No. 05K13SJ2. C.S. acknowledges support from NASA under Grant No. 80GSFC21M0002 and MPG. M.A.L. acknowledges support from NASA's Astrophysics Program. We acknowledge DESY (Hamburg, Germany), a member of the Helmholtz Association HGF, for the provision of experimental facilities. Parts of this research were carried out at PETRA III. We thank Jens Viefhaus and Rolf Follath for valuable discussions on x-ray monochromator resolution and performance, and the synchrotron-operation team at PETRA III for their skillful and reliable work.

[1] S. Kaspi, W. N. Brandt, H. Netzer, I. M. George, G. Chartas, E. Behar, R. M. Sambruna, G. P. Garmire, and J. A. Nousek, Astrophys. J. **554**, 216 (2001).
[2] E. Behar and H. Netzer, Astrophys. J. **570**, 165 (2002).
[3] J. C. Lee, P. M. Ogle, C. R. Canizares, H. L. Marshall, N. S. Schulz, R. Morales, A. C. Fabian, and K. Iwasawa, Astrophys. J. **554**, L13 (2001).
[4] P. Richter, F. B. S. Paerels, and J. S. Kaastra, Space Sci. Rev. **134**, 25 (2008).
[5] E. Behar, A. P. Rasmussen, A. J. Blustin, M. Sako, S. M. Kahn, J. S. Kaastra, G. Branduardi-Raymont, and K. C. Steenbrugge, Astrophys. J. **598**, 232 (2003).
[6] K. C. Steenbrugge, J. S. Kaastra, C. P. de Vries, and R. Edelson, Astron. Astrophys. **402**, 477 (2003).
[7] A. J. Blustin, G. Branduardi-Raymont, E. Behar, J. S. Kaastra, S. M. Kahn, M. J. Page, M. Sako, and K. C. Steenbrugge, Astron. Astrophys. **392**, 453 (2002).
[8] E. Behar and S. M. Kahn, arXiv:astro-ph/0210280.
[9] T. Holczer, E. Behar, and N. Arav, Astrophys. J. **708**, 981 (2010).
[10] S. Mathur, F. Nicastro, A. Gupta, Y. Krongold, B. M. McLaughlin, N. Brickhouse, and A. Pradhan, Astrophys. J. Lett. **851**, L7 (2017).
[11] M. Schmidt, P. Beiersdorfer, H. Chen, D. B. Thorn, E. Träbert, and E. Behar, Astrophys. J. **604**, 562 (2004).
[12] B. J. Wargelin, S. M. Kahn, and P. Beiersdorfer, Phys. Rev. A **63**, 022710 (2001).
[13] O. Marchuk, G. Bertschinger, H.-J. Kunze, N. R. Badnell, and S. Fritzsche, J. Phys. B: At., Mol. Opt. Phys. **37**, 1951 (2004).
[14] P. Beiersdorfer, J. Phys. B: At., Mol. Opt. Phys. **48**, 144017 (2015).
[15] V. A. Yerokhin, A. Surzhykov, and A. Müller, Phys. Rev. A **96**, 042505 (2017).
[16] V. A. Yerokhin, A. Surzhykov, and A. Müller, Phys. Rev. A **96**, 069901(E) (2017).
[17] V. A. Yerokhin and A. Surzhykov, Phys. Rev. A **86**, 042507 (2012).
[18] V. A. Zaytsev, I. A. Maltsev, I. I. Tupitsyn, V. M. Shabaev, and V. Y. Ivanov, Opt. Spectrosc. **128**, 307 (2020).
[19] V. Yerokhin and A. Surzhykov, J. Phys. Chem. Ref. Data **48**, 033104 (2019).
[20] L. A. Vainshtein and U. I. Safronova, Phys. Scr. **31**, 519 (1985).
[21] J. Machado, G. Bian, N. Paul, M. Trassinelli, P. Amaro, M. Guerra, C. I. Szabo, A. Gumberidze, J. M. Isac, J. P. Santos, J. P. Desclaux, and P. Indelicato, Phys. Rev. A **101**, 062505 (2020).
[22] S. Schlesser, S. Boucard, D. S. Covita, J. M. F. dos Santos, H. Fuhrmann, D. Gotta, A. Gruber, M. Hennebach, A. Hirtl,

P. Indelicato, E.-O. Le Bigot, L. M. Simons, L. Stingelin, M. Trassinelli, J. F. C. A. Veloso, A. Wasser, and J. Zmeskal, Phys. Rev. A **88**, 022503 (2013).
[23] V. Azarov, A. Kramida, and Y. Ralchenko, At. Data Nucl. Data Tables **149**, 101548 (2023).
[24] S. Mannervik, S. Asp, L. Broström, D. R. DeWitt, J. Lidberg, R. Schuch, and K. T. Chung, Phys. Rev. A **55**, 1810 (1997).
[25] A. E. Kramida and M.-C. Buchet-Poulizac, Eur. Phys. J. D **39**, 173 (2006).
[26] M. F. Gu, M. Schmidt, P. Beiersdorfer, H. Chen, D. B. Thorn, E. Träbert, E. Behar, and S. M. Kahn, Astrophys. J. **627**, 1066 (2005).
[27] B. M. McLaughlin, J.-M. Bizau, D. Cubaynes, S. Guilbaud, S. Douix, M. M. A. Shorman, M. O. A. E. Ghazaly, I. Sakho, and M. F. Gharaibeh, Mon. Not. R. Astron. Soc. **465**, 4690 (2017).
[28] J. M. Bizau, D. Cubaynes, S. Guilbaud, M. M. Al Shorman, M. F. Gharaibeh, I. Q. Ababneh, C. Blancard, and B. M. McLaughlin, Phys. Rev. A **92**, 023401 (2015).
[29] M. Coreno, M. de Simone, K. Prince, R. Richter, M. Vondráček, L. Avaldi, and R. Camilloni, Chem. Phys. Lett. **306**, 269 (1999).
[30] M. A. Leutenegger, S. Kühn, P. Micke, R. Steinbrügge, J. Stierhof, C. Shah, N. Hell, M. Bissinger, M. Hirsch, R. Ballhausen, M. Lang, C. Gräfe, S. Wipf, R. Cumbee, G. L. Betancourt-Martinez, S. Park, V. A. Yerokhin, A. Surzhykov, W. C. Stolte, J. Niskanen *et al.*, Phys. Rev. Lett. **125**, 243001 (2020).
[31] J. Stierhof, S. Kühn, M. Winter, P. Micke, R. Steinbrügge, C. Shah, N. Hell, M. Bissinger, M. Hirsch, R. Ballhausen *et al.*, Eur. Phys. J. D **76**, 1 (2022).
[32] M. Hoesch, J. Seltmann, F. Trinter, S. Kühn, M. Togawa, R. Steinbrügge, S. Bernitt, and J. R. Crespo López-Urrutia, J. Phys.: Conf. Ser. **2380**, 012086 (2022).
[33] S. Kühn, C. Cheung, N. S. Oreshkina, R. Steinbrügge, M. Togawa, S. Bernitt, L. Berger, J. Buck, M. Hoesch, J. Seltmann, F. Trinter, C. H. Keitel, M. G. Kozlov, S. G. Porsev, M. F. Gu, F. S. Porter, T. Pfeifer, M. A. Leutenegger, Z. Harman, M. S. Safronova *et al.*, Phys. Rev. Lett. **129**, 245001 (2022).
[34] J. Viefhaus, F. Scholz, S. Deinert, L. Glaser, M. Ilchen, J. Seltmann, P. Walter, and F. Siewert, Nucl. Instrum. Methods Phys. Res., Sect. A **710**, 151 (2013).
[35] P. Micke, S. Kühn, L. Buchauer, J. R. Harries, T. M. Bücking, K. Blaum, A. Cieluch, A. Egl, D. Hollain, S. Kraemer, T. Pfeifer, P. O. Schmidt, R. X. Schüssler, C. Schweiger, T. Stöhlker, S. Sturm, R. N. Wolf, S. Bernitt, and J. R. Crespo López-Urrutia, Rev. Sci. Instrum. **89**, 063109 (2018).
[36] S. W. Epp, J. R. Crespo López-Urrutia, G. Brenner, V. Mäckel, P. H. Mokler, R. Treusch, M. Kuhlmann, M. V. Yurkov, J. Feldhaus, J. R. Schneider, M. Wellhöfer, M. Martins, W. Wurth, and J. Ullrich, Phys. Rev. Lett. **98**, 183001 (2007).
[37] M. C. Simon, J. R. Crespo López-Urrutia, C. Beilmann, M. Schwarz, Z. Harman, S. W. Epp, B. L. Schmitt, T. M. Baumann, E. Behar, S. Bernitt, R. Follath, R. Ginzel, C. H. Keitel, R. Klawitter, K. Kubiček, V. Mäckel, P. H. Mokler, G. Reichardt, O. Schwarzkopf, and J. Ullrich, Phys. Rev. Lett. **105**, 183001 (2010).
[38] J. K. Rudolph, S. Bernitt, S. W. Epp, R. Steinbrügge, C. Beilmann, G. V. Brown, S. Eberle, A. Graf, Z. Harman, N. Hell, M. Leutenegger, A. Müller, K. Schlage, H.-C. Wille, H. Yavaş, J. Ullrich, and J. R. Crespo López-Urrutia, Phys. Rev. Lett. **111**, 103002 (2013).
[39] R. Steinbrügge, S. Bernitt, S. W. Epp, J. K. Rudolph, C. Beilmann, H. Bekker, S. Eberle, A. Müller, O. O. Versolato, H.-C. Wille, H. Yavaş, J. Ullrich, and J. R. Crespo López-Urrutia, Phys. Rev. A **91**, 032502 (2015).
[40] S. Kühn, C. Shah, J. R. Crespo López-Urrutia, K. Fujii, R. Steinbrügge, J. Stierhof, M. Togawa, Z. Harman, N. S. Oreshkina, C. Cheung, M. G. Kozlov, S. G. Porsev, M. S. Safronova, J. C. Berengut, M. Rosner, M. Bissinger, R. Ballhausen, N. Hell, S. Park, M. Chung *et al.*, Phys. Rev. Lett. **124**, 225001 (2020).
[41] C. Shah, S. Kühn, S. Bernitt, R. Steinbrügge, M. Togawa, L. Berger, J. Buck, M. Hoesch, J. Seltmann, M. G. Kozlov *et al.*, Phys. Rev. A **109**, 063108 (2024).
[42] C. Shah, M. Togawa, M. Botz, J. Danisch, J. J. Goes, S. Bernitt, M. Maxton, K. Köbnick, J. Buck, J. Seltmann *et al.*, ApJ **969**, 52 (2024).
[43] J. Krempaský, R. Follath, V. N. Strocov, T. Schmitt, and U. Flechsig, Proc. SPIE **8139**, 81390K (2011).
[44] R. Follath and A. Balzer, AIP Conf. Proc. **1234**, 657 (2010).
[45] C. Nordling, E. Sokolowski, and K. Siegbahn, Phys. Rev. **105**, 1676 (1957).
[46] M. Ünzelmann, H. Bentmann, T. Figgemeier, P. Eck, J. Neu, B. Geldiyev, F. Diekmann, S. Rohlf, J. Buck, M. Hoesch, M. Kalläne, K. Rossnagel, R. Thomale, T. Siegrist, G. Sangiovanni, D. D. Sante, and F. Reinert, Nat. Commun. **12**, 3650 (2021).
[47] M. P. Seah, I. S. Gilmore, and G. Beamson, Surf. Interface Anal. **26**, 642 (1998).
[48] S. Aksela, T. Kantia, M. Patanen, A. Mäkinen, S. Urpelainen, and H. Aksela, J. Electron Spectrosc. Relat. Phenom. **185**, 273 (2012).
[49] See Supplemental Material at http://link.aps.org/supplemental/10.1103/PhysRevA.110.L030802 for technical details of the present experiment and further details on the error estimation.
[50] V. A. Zaytsev, I. A. Maltsev, I. I. Tupitsyn, and V. M. Shabaev, Phys. Rev. A **100**, 052504 (2019).
[51] Y. K. Ho, Phys. Rep. **99**, 1 (1983).
[52] N. Moiseyev, Phys. Rep. **302**, 212 (1998).
[53] E. Lindroth and L. Argenti, in *Advances in Quantum Chemistry*, edited by C. A. Nicolaides, E. Brändas, and J. R. Sabin (Academic Press, New York, 2012), Vol. 63, Chap. 5, pp. 247–308.
[54] L. Vainshtein and U. Safronova, At. Data Nucl. Data Tables **21**, 49 (1978).
[55] A. Gabriel, Mon. Not. R. Astron. Soc. **160**, 99 (1972).
[56] A. K. Pradhan, G. X. Chen, F. Delahaye, S. N. Nahar, and J. Oelgoetz, Mon. Not. R. Astron. Soc. **341**, 1268 (2003).
[57] Y. Yao, N. S. Schulz, M. F. Gu, M. A. Nowak, and C. R. Canizares, Astrophys. J. **696**, 1418 (2009).
[58] J.-Y. Liao, S.-N. Zhang, and Y. Yao, Astrophys. J. **774**, 116 (2013).
[59] E. Gatuzz, J. García, C. Mendoza, T. R. Kallman, M. Witthoeft, A. Lohfink, M. A. Bautista, P. Palmeri, and P. Quinet, Astrophys. J. **768**, 60 (2013).
[60] M. Tashiro, H. Maejima, K. Toda, R. Kelley, L. Reichenthal, J. Lobell, R. Petre, M. Guainazzi, E. Costantini, M. Edison *et al.*, Proc. SPIE **10699**, 1069922 (2018).

[61] F. Pajot, D. Barret, T. Lam-Trong, J.-W. Den Herder, L. Piro, M. Cappi, J. Huovelin, R. Kelley, J. Mas-Hesse, K. Mitsuda *et al.*, J. Low Temp. Phys. **193**, 901 (2018).
[62] R. K. Heilmann, A. R. Bruccoleri, V. Burwitz, C. DeRoo, A. Garner, H. M. Günther, E. M. Gullikson, G. Hartner, E. Hertz, A. Langmeier, T. Müller, S. Rukdee, T. Schmidt, R. K. Smith, and M. L. Schattenburg, Astrophys. J. **934**, 171 (2022).
[63] N. V. Roth and R. C. Elton, Measurement and Identification of Laboratory Produced Vacuum Ultraviolet Spectral Lines (NRL Report 6638), Tech. inform., U.S. Clearinghouse Fed. Sci., 1968, p. 41, AD 667584.
[64] A. H. Gabriel and C. Jordan, Nature (London) **221**, 947 (1969).
[65] D. L. Matthews, W. J. Braithwaite, H. H. Wolter, and C. F. Moore, Phys. Rev. A **8**, 1397 (1973).
[66] A. Pospieszczyk, Astron. Astrophys. **39**, 357 (1975).
[67] P. Nicolosi and G. Tondello, J. Opt. Soc. Am. **67**, 1033 (1977).
[68] R. Bruch, D. Schneider, W. H. E. Schwarz, M. Meinhart, B. M. Johnson, and K. Taulbjerg, Phys. Rev. A **19**, 587 (1979).
[69] M. Mack and A. Niehaus, Nucl. Instrum. Methods Phys. Res., Sect. B **23**, 291 (1987).
[70] R. Bruch, N. Stolterfoht, S. Datz, P. D. Miller, P. L. Pepmiller, Y. Yamazaki, H. F. Krause, J. K. Swenson, K. T. Chung, and B. F. Davis, Phys. Rev. A **35**, 4114 (1987).
[71] G. Hofmann, A. Müller, K. Tinschert, and E. Salzborn, Z. Phys. D: At., Mol. Clusters **16**, 113 (1990).
[72] D. H. Lee, T. J. M. Zouros, J. M. Sanders, P. Richard, J. M. Anthony, Y. D. Wang, and J. H. McGuire, Phys. Rev. A **46**, 1374 (1992).

High-accuracy Measurements of Core-excited Transitions in Light Li-like Ions: Supplemental Material

Acquisition of PES trace

In this experiment we scan a wide photon energy window, much larger than what can be accepted by the pass energy of the photoelectron spectrometer (PES), while retaining a good resolution. To keep the lines within the spectrometer acceptance, we utilized a bias voltage on the gold target to change synchronous with the incident nominal photon energy. In principle, this compensates the increase in kinetic energy during a scan, therefore ensuring the lines to be kept centered with the exception of the fluctuation of $\sim 10\,\mathrm{meV}$ due to the monochromator encoders. However, we have observed a drift of several eV over the course of one photon energy scan (see Fig. 1). We have identified this significant drift as a miscalibration of the bias voltage supply, specifically with the Keithley 6517A model. Using a secondary calibrated high-resolution voltage meter, we found the drift to be linear. Fortunately, this additional linearity is accounted for by the polynomial function we use to calibrate the photon energy scale. Hence, we find this effect to be not significant to the final energy determination. Furthermore, the high quality of the calibration, as shown in the bottom pane of Fig. 5, indicates the absence of unaccounted large systematic errors.

Calibration of PES kinetic energy scale

In order to map the detector spread to corresponding kinetic energies, the bias voltage is scanned at a fixed photon energy. Both gold lines are consequently shifted through the detector area. By plotting the position of the gold lines as a function of the bias voltage, a continuous curve can be obtained, which assigns the detector position to the respective bias voltage (Fig. 2 top). For the kinetic energy calibration, a unit voltage is interpreted as a unit of kinetic energy. In order to model the calibration data, an appropriate linear curve is first subtracted from the data, revealing a residual showing a clear indication for a higher-order polynomial function in the energy calibration (Fig. 2 middle). A suitable polynomial model is therefore additionally applied to the residual data, which is then combined with the initial linear function to obtain a smooth energy calibration function (Fig. 2 bottom). From the reduced chi-square, we see that the statistical uncertainty alone can not serve as a justification of the distribution of the residual data points. We will discuss this in more detail later.

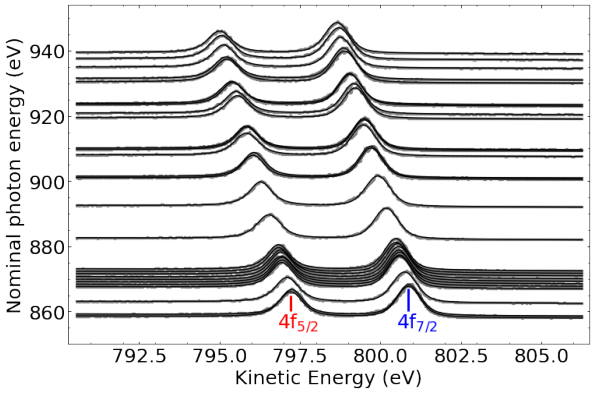

FIG. 1. A waterfall diagram depicting the change of gold line position over the duration of one exemplary scan. Amplitudes of all spectra are normalized to the height of the $4f_{7/2}$ line. Not all recorded spectra are shown for illustrative purposes.

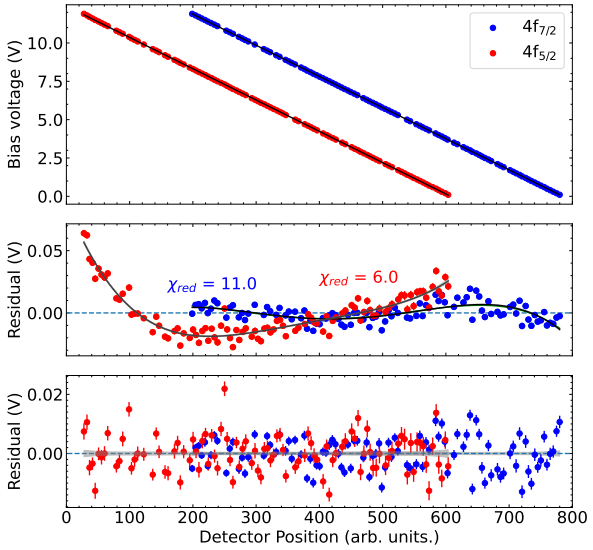

FIG. 2. Kinetic energy calibration of the photoelectron spectrum. The bias voltage is scanned from -12V to 0, which moves the 4f gold lines accordingly from one side to the other on the detector surface. After a linear model is fitted to the data points, the residuals reveal a clear nonlinearity at the edge the detector. This nonlinearity is additionally modeled and added to the initial linear curve.

Energy correction and calibration of the nominal photon energy scale

The energy correction of the nominal photon energy scale is obtained by locally modeling a narrow photon energy window of the calibrated PES trace with a poly-

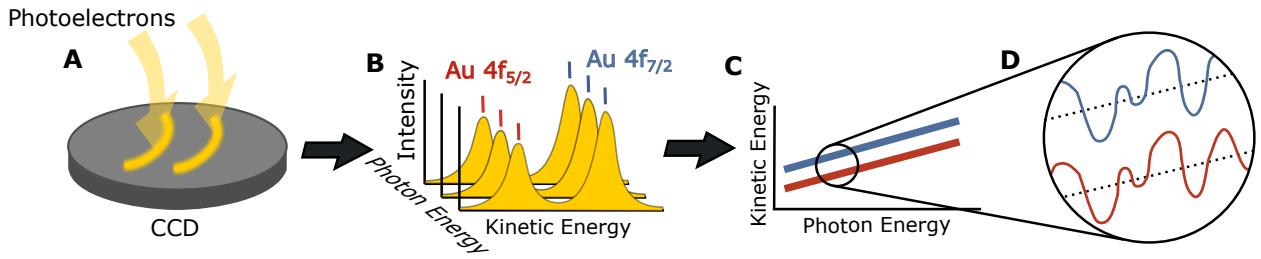

FIG. 3. Principle of the energy correction. (A): The hemispherical spectrometer (PES) registers with high resolution Au $4f_{5/2,7/2}$ photoelectrons on a multichannel-plate (MCP) screen imaged by a camera. A bias applied to the Au target following the nominal photon energy keeps the photoelectron peaks centered on the MCP along the whole scan. (B): The image projection onto the dispersive axis shows small deviations of the actual kinetic energy at each monochromator step. (C) Subtracting a linear fit from the photoelectron energies yields for both peaks periodic deviations shown as blue and red curves in (D) from the nominal photon energy scale due to imperfect interpolations of the grating and mirror angles in the monochromator.

nomial model for each recorded transition. This smooth function is then used as an additional offset to the nominal energy axis of the incident photon energy. After assigning the calibration lines to their respective known theoretical energies from reference [1], a suitable polynomial function is fitted to the data (Fig. 5 top). Figure 5 displays the uncertainty band obtained from an exemplary calibration of the nominal photon energy. The quality of this photon energy calibration is greatly increased by applying the energy correction as can be seen in the middle plot of Fig. 5, which shows the residuals of calibration without applying the energy correction. Such measurements have been repeated several times for each element.

Uncertainty 1: nonlinear contribution in PES detector calibration function

Figure 4 displays the result of five measurements of neon, which have been analyzed as described so far. The analysis has been performed twice per measurement by exchanging the source of the energy correction (either from $4f_{7/2}$ or $4f_{5/2}$). In principle, no significant deviation should be observable by the choice of the correction function. However, by evaluating a weighted average independently, a systematic shift between both results seems to be present (Fig. 4). This effect is most prominent for neon, less prominent for fluorine and negligible for oxygen. We suspect that this effect is due to a position dependent error within the applied PES detector calibration, which has not been accounted for.We conservatively estimate the uncertainty from the outer edges of both uncertainty bands.

Uncertainty 2. Energy profile of incident photons

In the experiment, the energy resolution as well as the energy profile of the incident photon beam has been op-

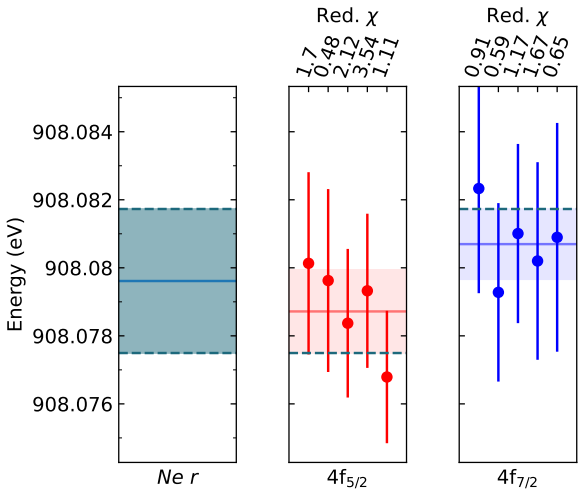

FIG. 4. Visualization of error estimation. For each element several measurements have been recorded. Each measurement has been analyzed by utilizing the $4f_{7/2}$ as well as $4f_{5/2}$ gold line as source of the correction function. Weighted averages are determined for each set. Both results for Ne r are displayed in blue and red, respectively. The final uncertainty is estimated from the outermost edges of both uncertainty bands.

timized with the 1s-2p J = 1 transition of He-like oxygen at 574eV. We have observed a slight decrease in beam profile quality for the energetically higher lying neon and fluorine measurements, resulting in a slightly asymmetric line profile, an effect, which has been observed several times in the past [4]. If at all, the asymmetry can be seen for the calibration lines, however for q and r, which are not fully resolved, the asymmetry is not clearly visible. In order to estimate this systematic shift resulting from the asymmetric line shape, we first determine the centroid of the peak given from the applied symmetric Voigt models and compare it by applying a skewed Voigt model to the data. An approximate 1 meV shift can be observed

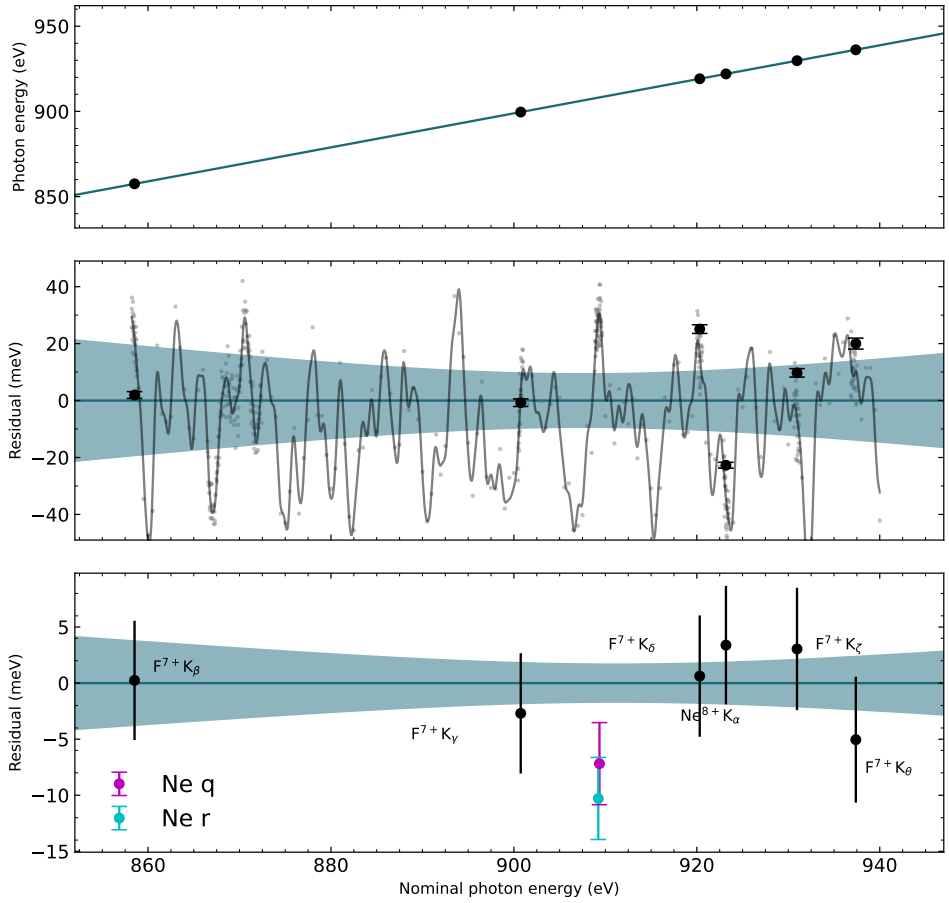

FIG. 5. Exemplary calibration curve and corresponding residuals for neon q and r. Top: Experimentally determined photon energies of calibration lines are plotted against their corresponding theoretical prediction from ref.[2]. Center: Residuals of the fit and 1-σ confidence band. Bottom: Residuals of the fit and confidence band, taking into account the fluctuation due to the monochromator encoders (Grey line). To compare the position of the predicted q and r lines to the experiment, we show in the bottom panel of figure the theoretical values of q and r from ref.[1, 3] with respect to the experimental calibration function.

independently of the applied skewed Voigt model. This uncertainty will be taken into account in the final error budget.

Uncertainty 3. Precision and accuracy of photoelectron measurement.

In this section we discuss the XPS measurements, which are used for energy correction. After initial set up of the PES, the position of the gold lines on the detector is highly sensitive to the temporal stability of the voltage sources and more importantly the voltage source used to bias the gold target. Any fluctuation of the sources will eventually translate to the energy of the q and r lines. It is therefore important to estimate the uncertainty produced by the reproducibility of a photoelectron spectroscopy measurement. In figure 6, we use the residuals obtained after modeling of the photoelectron trace and produce a histogram showing the distribution of residuals, each corresponding to a XPS measurement. By comparing the one sigma width of the distribution with the averaged statistical uncertainty of centroid determination (Fig. 6, top row), we see in all three cases a significantly larger width of the distribution. This leads

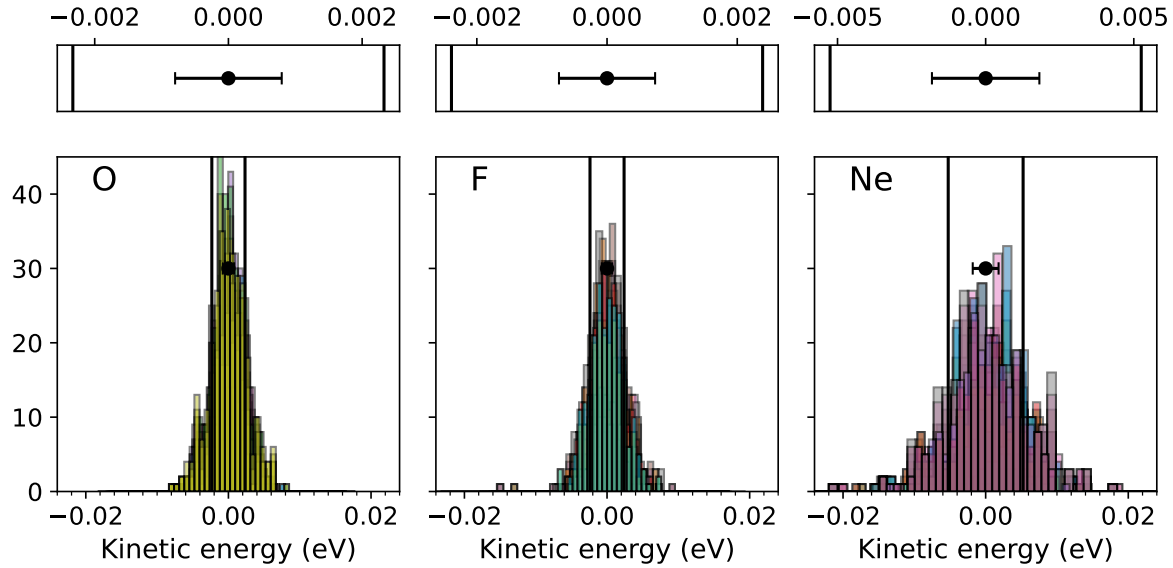

FIG. 6. Residuals obtained from the modeled photoelectron traces of single measurements are displayed as histograms. One sigma intervals of the distribution are shown as black vertical lines. On top we plot the average uncertainty of a single measurement, which includes the quadratically added statistical and calibration error.

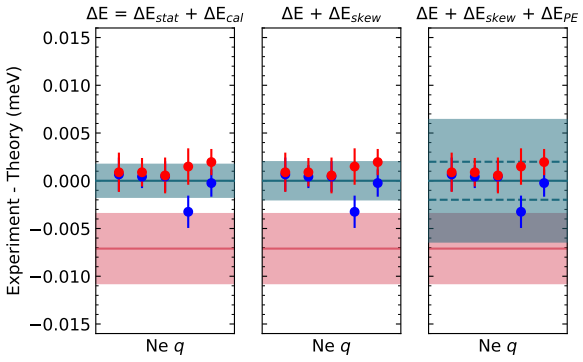

FIG. 7. The blue shaded areas depict the experimental uncertainty under inclusion of different sources of error. Prediction of Refs. [1] are represented by the red line and shaded area. Left: Uncertainty estimated by means of the two individual energy correction procedures involving the gold $4f_{7/2}$and $4f_{5/2}$. Center: A minute increase in error due to the added uncertainty from to the skewed lineshape. Right: Additional inclusion of the PES measurement uncertainty.

to the conclusion that the spread of the individual measurements can not be solely attributed to the statistical uncertainty of the XPS measurement. We therefore use the one sigma width derived from these distributions as an estimate for the systematic photoelectron energy uncertainty.

In figure 7 we show how the individual sources of uncertainty add to the total measurement uncertainty.

[1] V. A. Yerokhin, A. Surzhykov, and A. Müller, Relativistic configuration-interaction calculations of the energy levels of the $1s^2 2l$ and $1s2l2l'$ states in lithiumlike ions: Carbon through chlorine, Phys. Rev. A **96**, 042505 (2017).

[2] V. Yerokhin and A. Surzhykov, Theoretical energy levels of 1 sns and 1 snp states of helium-like ions, Journal of Physical and Chemical Reference Data **48**, 033104 (2019).

[3] V. A. Yerokhin, A. Surzhykov, and A. Müller, Erratum: Relativistic configuration-interaction calculations of the energy levels of the and $1s2l2l'$ states in lithiumlike ions: Carbon through chlorine [phys. rev. a 96, 042505 (2017)], Phys. Rev. A **96**, 069901 (2017).

[4] S. Kühn, C. Cheung, N. S. Oreshkina, R. Steinbrügge, M. Togawa, S. Bernitt, L. Berger, J. Buck, M. Hoesch, J. Seltmann, F. Trinter, C. H. Keitel, M. G. Kozlov, S. G. Porsev, M. F. Gu, F. S. Porter, T. Pfeifer, M. A. Leutenegger, Z. Harman, M. S. Safronova, J. R. C. López-Urrutia, and C. Shah, New measurement resolves key astrophysical fe xvii oscillator strength problem, Phys. Rev. Lett. **129**, 245001 (2022).

2.2 High-precision Transition Energy Measurements of Neon-like Fe xvii Ions

Line positions soft X-ray lines of highly charged iron, used for plasma diagnostics, have been measured with improved precision and compared with stae-of-the-art predictions. This article was published in *The Astrophysical Journal*.

AUTHORS Chintan Shah , **Moto Togawa** , Marc Botz , Jonas Danisch , Joschka J. Goes , Sonja Bernitt , Marleen Maxton , Kai Köbnick , Jens Buck , Jörn Seltmann , Moritz Hoesch , Ming Feng Gu , F. Scott Porter , Thomas Pfeifer , Maurice A. Leutenegger , Charles Cheung , Marianna S. Safronova , José R. Crespo López-Urrutia

PUBLICATION STATUS Published 28 June 2024

JOURNAL REFERENCE ApJ 969 52

DIGITAL OBJECT IDENTIFIER https://doi.org/10.3847/1538-4357/ad454b

AUTHOR'S CONTRIBUTIONS CS and **MT** prepared and organized the experiment. CS, **MT**, MB, JD, JG, SB, MM, KK and JRCLU took the data. JB, JS, MH operated the synchrotron radiation beamline. CS and **MT** analyzed the data. CS wrote the manuscript. All authors took part in the critical review of the manuscript before and after submission.

ABSTRACT We improve by a factor of 4–20 the energy accuracy of the strongest soft X-ray transitions of Fe XVII ions by resonantly exciting them in an electron beam ion trap with a monochromatic beam at the P04 beamline of the PETRA III synchrotron facility. By simultaneously tracking instantaneous photon-energy fluctuations with a high-resolution photoelectron spectrometer, we minimize systematic uncertainties down to 10–15 meV, or velocity equivalent $\pm \sim 5\,\mathrm{km\,s^{-1}}$ in their rest energies, substantially improving our knowledge of this key astrophysical ion. Our large-scale configuration-interaction computations include more than 4 million relativistic configurations and agree with the experiment at a level without precedent for a 10-electron system. Thereby, theoretical uncertainties for interelectronic correlations become far smaller than those of quantum electrodynamics (QED) corrections. The present QED benchmark strengthens our trust in future calculations of many other complex atomic ions of interest to astrophysics, plasma physics, and the development of optical clocks with highly charged ions.

The Astrophysical Journal, 969:52 (12pp), 2024 July 1 https://doi.org/10.3847/1538-4357/ad454b

High-precision Transition Energy Measurements of Neon-like Fe XVII Ions

Chintan Shah[1,2,3], Moto Togawa[2,4,5], Marc Botz[2,5], Jonas Danisch[2], Joschka J. Goes[2], Sonja Bernitt[2,6,7,8], Marleen Maxton[2], Kai Köbnick[2], Jens Buck[9], Jörn Seltmann[10], Moritz Hoesch[10], Ming Feng Gu[11], F. Scott Porter[1], Thomas Pfeifer[2], Maurice A. Leutenegger[1], Charles Cheung[12], Marianna S. Safronova[12], and José R. Crespo López-Urrutia[2]

[1] NASA Goddard Space Flight Center, 8800 Greenbelt Road, Greenbelt, MD 20771, USA
[2] Max-Planck-Institut für Kernphysik, Saupfercheckweg 1, 69117 Heidelberg, Germany; chintan.shah@mpi-hd.mpg.de
[3] Center for Space Sciences and Technology, University of Maryland, Baltimore County, 1000 Hilltop Circle, Baltimore, MD 21250, USA
[4] European XFEL, Holzkoppel 4, 22869 Schenefeld, Germany
[5] Heidelberg Graduate School of Fundamental Physics, Ruprecht-Karls-Universität Heidelberg, Im Neuenheimer Feld 226, 69120 Heidelberg, Germany
[6] GSI Helmholtzzentrum für Schwerionenforschung, Planckstraße 1, 64291 Darmstadt, Germany
[7] Helmholtz-Institut Jena, Fröbelstieg 3, 07743 Jena, Germany
[8] Institut für Optik und Quantenelektronik, Friedrich-Schiller-Universität, Max-Wien-Platz 1, 07743 Jena, Germany
[9] Institut für Experimentelle und Angewandte Physik, Christian-Albrechts-Universität zu Kiel, Kiel, Germany
[10] Deutsches Elektronen-Synchrotron (DESY), Notkestrasse 85, 22607 Hamburg, Germany
[11] Space Science Laboratory, University of California, Berkeley, CA 94720, USA
[12] Department of Physics and Astronomy, University of Delaware, Newark, DE 19716, USA
Received 2024 January 11; revised 2024 April 2; accepted 2024 April 28; published 2024 June 28

Abstract

We improve by a factor of 4–20 the energy accuracy of the strongest soft X-ray transitions of Fe XVII ions by resonantly exciting them in an electron beam ion trap with a monochromatic beam at the P04 beamline of the PETRA III synchrotron facility. By simultaneously tracking instantaneous photon-energy fluctuations with a high-resolution photoelectron spectrometer, we minimize systematic uncertainties down to 10–15 meV, or velocity equivalent $\pm\sim$5 km s^{-1} in their rest energies, substantially improving our knowledge of this key astrophysical ion. Our large-scale configuration-interaction computations include more than 4 million relativistic configurations and agree with the experiment at a level without precedent for a 10-electron system. Thereby, theoretical uncertainties for interelectronic correlations become far smaller than those of quantum electrodynamics (QED) corrections. The present QED benchmark strengthens our trust in future calculations of many other complex atomic ions of interest to astrophysics, plasma physics, and the development of optical clocks with highly charged ions.

Unified Astronomy Thesaurus concepts: Atomic data benchmarking (2064); Laboratory astrophysics (2004); Line positions (2085); Atomic spectroscopy (2099); Experimental data (2371); Theoretical techniques (2093); Space plasmas (1544)

1. Introduction

Over the past three decades, extensive research has focused on the soft X-ray emission from Ne-like iron (Fe XVII, Fe^{16+}), particularly in hot astrophysical plasmas observed by Chandra and XMM-Newton (Behar et al. 2001; Brinkman et al. 2001). The dominant spectral transitions $3d \rightarrow 2p$ and $3s \rightarrow 2p$ of Fe XVII within the 700–850 eV range (14.5–17.5 Å) play a crucial role in deducing the plasma parameters across various sources. These parameters include the electron temperature, density, elemental abundance, gas motion, and photon scattering opacity (Parkinson 1973; Smith et al. 1985; Schmelz et al. 1992; Waljeski et al. 1994; Phillips et al. 1996; Behar et al. 2001; Mauche et al. 2001; Doron & Behar 2002; Xu et al. 2002; Gu 2003; Paerels & Kahn 2003; Werner et al. 2009; Pradhan & Nahar 2011; Beiersdorfer et al. 2018; Gu et al. 2019, 2020; Grell et al. 2021).

Despite decades of study, since early solar X-ray observations (Parkinson 1973; Smith et al. 1985; Schmelz et al. 1992; Waljeski et al. 1994), discrepancies between observed and theoretical intensity ratios (Brown et al. 1998) have persisted. Early explanations invoking resonance scattering (McKenzie et al. 1980; Schmelz et al. 1992; Saba et al. 1999) found no confirmation in measurements with electron-beam ion traps (EBITs) and tokamaks that also agreed with solar observations (Brown et al. 1998, 2001a, 2001b; Beiersdorfer et al. 2002, 2004; Brown et al. 2006; Gillaspy et al. 2011; Beiersdorfer et al. 2017; Shah et al. 2019). As optically thin laboratory plasmas are not subject to resonance scattering, indirect line formation mechanisms were suggested (Chen & Pradhan 2002; Gu 2003; Beiersdorfer et al. 2008, 2014, 2015; Shah et al. 2019; Gu et al. 2020; Grilo et al. 2021). An experiment with a free-electron laser aimed at directly determining the oscillator-strength ratio for lines 3C and 3D without uncertainties due to electron-impact excitation. Its unexpected results departing even more from theory were attributed to inaccuracies in calculated oscillator strengths (Bernitt et al. 2012), but soon after, unforeseen transient nonequilibrium effects and population transfer due to the ultrabrilliant peak photon flux explained them (Oreshkina et al. 2014; Loch et al. 2015; Oreshkina et al. 2016; Wu & Gao 2019). Our later measurements (Kühn et al. 2020) with synchrotron radiation avoided this nonlinear systematic and improved the accuracy of the oscillator-strength ratio while still disagreeing with the theory. Finally, further increases in resolving power and signal-to-noise ratio found the cause of the persistent discrepancies in hitherto unresolvable

line wings and diffraction effects and brought the oscillator-strength ratio in line with state-of-the-art predictions (Kühn et al. 2022).

In spite of these advances, many questions remain open for this essential ion and many other less-studied species. For instance, widely used wavelength references for Fe XVII from EBIT measurements using a crystal spectrometer with a resolving power of 500–700 have uncertainties of 1–3 mÅ (∼40–200 meV), Doppler-equivalent to ∼15–50 km s^{-1}, i.e., ∼60–180 parts per million (ppm), for $n = 3 - 2$, and double that for high-n transitions (Beiersdorfer & Wargelin 1994; Brown et al. 1998). This is only marginally adequate for analysis of high-resolution diffraction grating spectra acquired with the Chandra High Energy Transmission Grating Spectrometer (HETGS), which can measure velocities of bright emission lines with ∼25 km s^{-1} systematic uncertainty (Ishibashi et al. 2006; Bozzo et al. 2023). These uncertainties in transition energies will also impair the achievement of the science goals of other extant, upcoming, and proposed missions, including XMM-Newton (den Herder et al. 2001; Jansen et al. 2001), XRISM (Tashiro et al. 2018), Athena (Barret et al. 2016; Pajot et al. 2018), Line Emission Mapper (LEM; Kraft et al. 2022), Arcus (Heilmann et al. 2022; Smith et al. 2022), and Lynx (Schwartz et al. 2019). Even though some of these missions feature spectrometers with FWHM resolution far broader than the uncertainties of published rest-energy determinations, well-exposed spectra of bright objects with a high signal-to-noise ratio will allow centroid determination with uncertainties comparable to or smaller than these prior measurements. There is clearly a need for better determinations of the Fe XVII transition energies that will allow us to take full advantage of the resolving power of current and future missions, as well as improved and well-benchmarked theoretical methods that can provide energies for transitions that have not yet been measured with sufficient precision.

We report new measurements of the rest energies of key Fe XVII transitions with an EBIT at the P04 beamline of the PETRA III synchrotron with uncertainties below 15 ppm, an improvement by a factor of 4–20 over the status quo. The accuracy of our results translates in velocity terms to 5 km s^{-1} and fully unlocks the value of archived and forthcoming observations from XMM-Newton and Chandra, as well as of accurate velocimetry targeted by upcoming missions (Barret et al. 2016; Pajot et al. 2018; Heilmann et al. 2022; Kraft et al. 2022; Smith et al. 2022). We also test the large-scale configuration interaction (CI) approach and, therefore, our combination of the CI and coupled-cluster approaches (CI + all-order method), which is crucial for the development of high-precision clocks (Kozlov et al. 2018) and essential for understanding the quantum electrodynamics (QED) effects in many-electron systems. By applying the model potential approach (Tupitsyn et al. 2016) using the QEDMOD package (Shabaev et al. 2018), we incorporate QED effects into the effective Hamiltonian, basis-set orbitals, and one-electron matrix elements—a widely employed practice. The quality of the QED model potential is usually assessed against exact solutions for H-like ions since the uncertainty in the electronic correlation in HCI with a few valence electrons is usually larger, or at the level of QED contributions unless the ionization degree is rather high. Until this work, there were no estimates regarding the accuracy of the QEDMOD approach for the majority of many-electron systems.

Motivated by our highly accurate experimental results, we carry out new CI computations, taking the contributions from high nl states into account, increasing the number of relativistic configurations from 1.2 million in our previous work (Cheung et al. 2021; Kühn et al. 2022) to over 4 million, and investigating the convergence of the computations in both of these parameters. The results show a remarkable degree of numerical convergence across all energy levels and agree with the measurements to a level of 1–33 meV (1–45 ppm) that is unprecedented for a complex ion such as Fe XVII. For the first time, uncertainties in the electronic correlations smaller than QED corrections allow us to test the accuracy of the QED contribution in a many-electron system.

2. Measurements and Data Analysis

PolarX-EBIT (Micke et al. 2018) was designed for the study of highly charged ions interacting with X-ray photons at synchrotrons and free-electron lasers (see Kühn et al. 2020; Leutenegger et al. 2020; Togawa et al. 2020; Kühn et al. 2022; Steinbrügge et al. 2022; Stierhof et al. 2022). Its off-axis electron gun emits a nearly monoenergetic electron beam that is compressed to a diameter of less than 100 μm by a magnetic field of ∼870 mT generated by permanent magnets. Considering the overlap of the ion cloud and the electron beam leads to an effective electron density of $\sim 10^{10}$ cm^{-3}. Iron pentacarbonyl ($Fe(CO)_5$) molecules enter the trap region as a tenuous beam through a two-stage differential pumping system. There, electron-impact dissociation generates Fe atoms, and step-wise electron-impact ionization produces highly charged ions that remain radially trapped by the ensuing negative space-charge potential of the electron beam, and axially by biased cylindrical drift tubes. We chose operating conditions to ensure that Fe XVII ions mostly populate the trap.

At the soft X-ray beamline P04, an APPLE II undulator (Viefhaus et al. 2013) produces circularly polarized photons, which are then sent through a monochromator equipped with a variable line-spacing grating of 1200 lines mm^{-1} mean groove density. Using an exit slit opening of 50 μm, the energy resolution ΔE was set to a value of approximately $E/\Delta E$ ≈13,000 in the energy range of 700–1100 eV. A pair of plane-elliptical mirrors refocus this beam onto the ion cloud. The photon beam energy is scanned over the Fe XVII transitions of interest and the corresponding calibration lines. Two silicon drift detectors (SDD) mounted at the top and on the side of the EBIT register fluorescence, with ∼100 eV FWHM resolution, following from resonant photoexcitation as well as electron-impact excitation.

To calibrate the monochromator photon-energy scale, we excite K-shell transitions in H-like and He-like oxygen, fluorine, and neon ions trapped in PolarX-EBIT. Their energies can be calculated with uncertainties well below 1 meV. We take values for the H-like $1s \rightarrow 2p$ transitions from Yerokhin & Shabaev (2015), and from Erickson (1977) for $1s \rightarrow np$ up to $n = 7$, and for He-like ions, we take energy values from Yerokhin & Surzhykov (2019) for $1s \rightarrow np$ transitions up to $n = 7$.

The monochromator disperses the spectrum of the undulator cone on the exit slit by choice of incidence and diffraction angles of the grating, which is accomplished by appropriate rotations of both the grating and mirror, with the extra degree

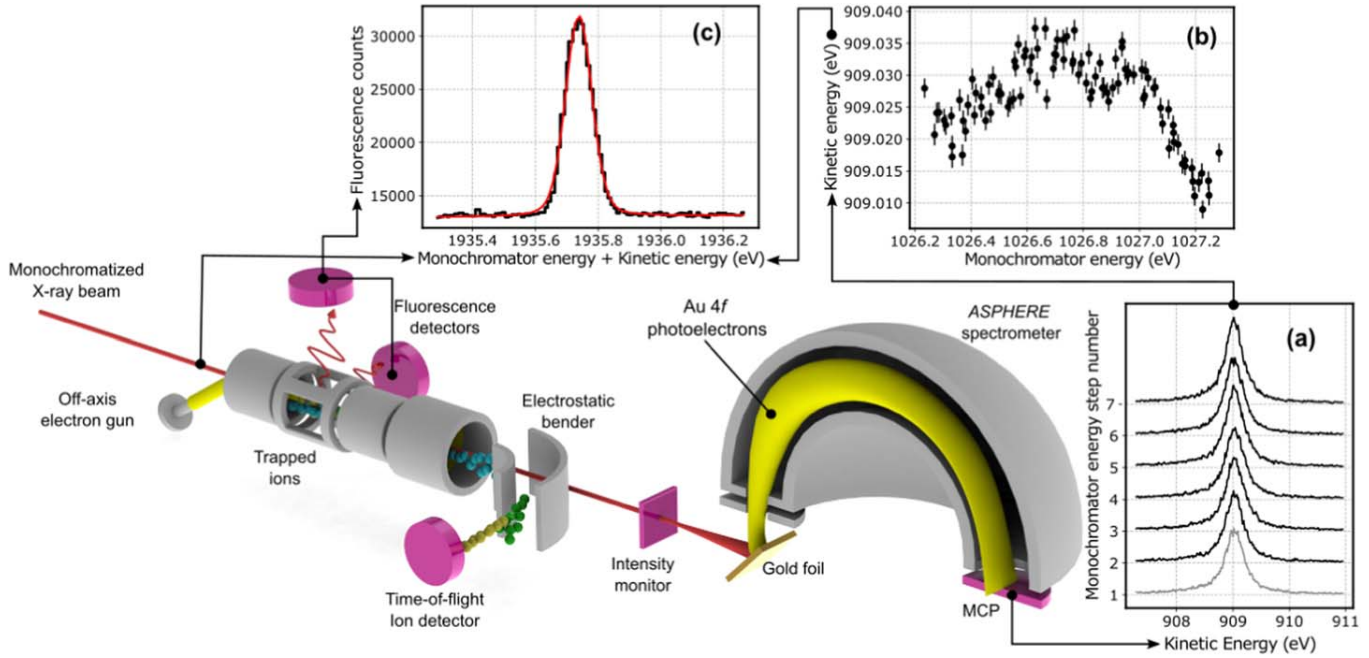

Figure 1. A photon beam of variable energy excites an elongated ion ensemble within a portable EBIT, PolarX-EBIT (Micke et al. 2018). Emitted fluorescence X-rays are recorded by two silicon drift detectors. Ions periodically released from the trap are mass-analyzed by their time of flight as a monitoring diagnostic of the trapped ion content. Downstream, the photon beam passes through a wire mesh used to measure its intensity before hitting a gold target and releasing photoelectrons that enter ASPHERE, a high-resolution hemispherical electron-energy analyzer. ASPHERE records (a) the Voigt-like kinetic energy distribution of Au $4f_{7/2}$ electrons and their centroids (b) at each monochromator energy step. Because we apply a bias to the Au target that tracks changes in the nominal monochromator energy, ideally, (b) is expected to exhibit constant values, but it shows small yet reproducible periodic deviations from the nominal monochromator energy scale due to interpolation errors in the angular encoders. These deviations are corrected for in (c) prior to calibration with reference lines.

of freedom removed by requiring fulfillment of the constant fix-focus condition (Follath 2001). The absolute angles of both grating and mirror are recorded using angular encoders. To measure electronic transitions with narrow natural line widths < 50 meV, angular increments as small as $\approx 10^{-5}$ degrees have to be resolved, equivalent to 36 mas or 175 nrad. The installed Heidenhain RON 905 angular encoders have 36,000 reference marks per turn, or one every 10^{-2} degrees (36″). Such encoders interpolate angle changes 1000 times between each mark. An LED source is positioned on one side of the disk, while two photodiodes are positioned on the opposite side of the disk to record the light intensity modulated by slight rotations of the encoder disk.[13] These intensity variations are then stored in an empirical lookup table in the hardware. However, the process is highly sensitive to imperfections in the analog signals, which can lead to periodic subdivision errors (Follath & Balzer 2010; Krempaský et al. 2011). Furthermore, within each monochromator, there are two encoders—one dedicated to the grating and the other to the focusing mirror. This doubles the uncertainty in the interpolation, impacting the determination of the diffraction angle. Consequently, this can cause the nominal monochromator energy to deviate from the actual photon beam energy. This problem was previously observed in our studies at P04 (Kühn et al. 2022; Togawa et al. 2023) and other beamlines (Follath & Balzer 2010; Krempaský et al. 2011), and leads to periodic fluctuations in the nominal photon-energy scale, which in our case have peak-to-peak amplitudes of up to ∼50 meV below 900 eV and ∼70 meV above 900 eV.

To correct for them while scanning the monochromator to excite resonant transitions, we direct the photon beam exiting the EBIT onto a gold target mounted on a high-resolution hemispherical electron-energy analyzer, ASPHERE (Rossnagel et al. 2001), as shown in Figure 1. There, $4f_{5/2,7/2}$ photoelectrons are emitted, and their kinetic energy is measured. The kinetic energy of these photoelectrons is given by the difference between the photon energy and the binding energy of the electrons, along with any potential bias applied to the gold target. If the bias potential applied to the target is constant, any change in the photon energy will manifest itself as a change in the kinetic energy of the $4f$ Au electrons. However, if we change the target bias to track changes in the nominal photon energy, the electron kinetic energy remains nominally constant and the photoelectron peak (Au $4f_{7/2}$) can appear at a fixed position on the electron detector, see Figure 1(a). Thus, any deviation of the actual photon energy from the nominal photon energy set by the monochromator would result in a deviation of the kinetic energy of the photoelectrons. An example of such a deviation, reflecting the interpolation inaccuracies of the two angular encoders of the monochromator, is shown in Figure 1(b). We fit Au $4f_{7/2}$ peaks (line widths of about 700 meV FWHM) with Voigt profiles to find their centroids and determine their kinetic energies with uncertainties of a few meV at electron count rates of $\sim 10^4$ s^{-1}. By cooling the gold target to liquid nitrogen temperature, we further reduce the peak width to ∼450 meV, which further improves centroid determination. We then use this information to correct each step of the nominal monochromator energy scale. To avoid any assumptions in modeling these deviations shown in Figure 1(b), and because the addition of an arbitrary constant term to the energy scale will be removed when calibrating against

[13] https://www.heidenhain.us/wp-content/uploads/2022/07/591109-24_Angle_Encoders_with_Integral_Bearing.pdf

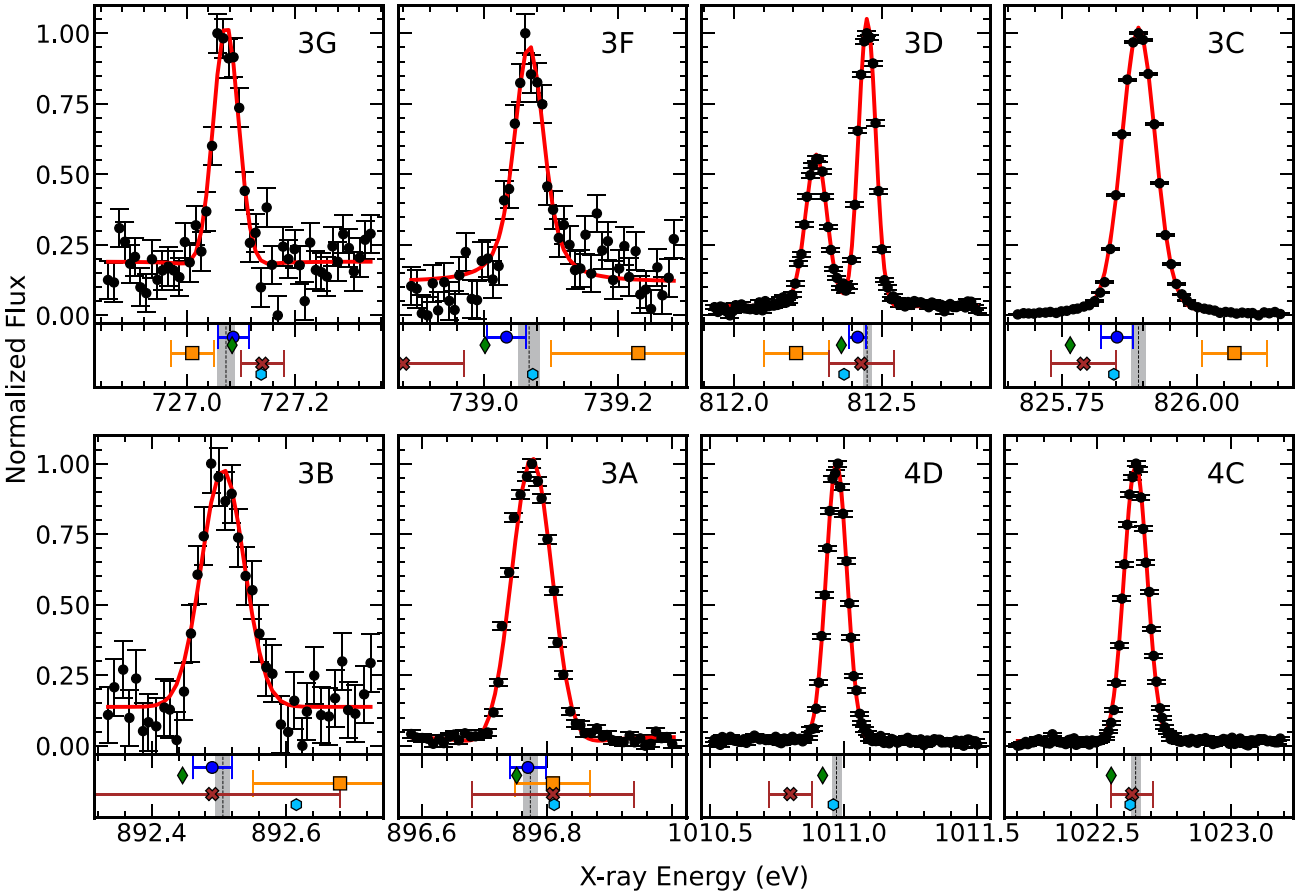

Figure 2. (Top panels) Representative scan for each of the measured Fe XVII lines. Both the data and model are scaled to the range [0,1]. (Bottom panels) Measured transition energies derived from a weighted average of all scans are depicted with their total uncertainty represented by the gray band. They are compared against Large CI (blue circles), FAC MBPT (green diamonds), solar observations (cyan hexagons), and previous laboratory data (orange squares: Beiersdorfer & Wargelin 1994; brown crosses: Brown et al. 1998).

known reference energies, we simply add the measured electron kinetic energy directly to the nominal monochromator energy scale rather than first subtracting a nominal kinetic energy offset. On this corrected monochromator energy scale (Figure 1(c)), we then determine the centroids of the calibration lines and associate them with the theoretical references mentioned above. By fitting a third-order polynomial to these data, we obtain the dispersion curve and thus the calibrated monochromator energy scale.

For the Fe XVII measurements, we set the EBIT to use a ∼4 mA, 3500 eV electron beam, capable of directly exciting the lines studied here, and thus generating an undesired background. These parameters yielded a ratio of photoexcitation peak to electron-impact background between 2 and 3 throughout the experiment, indeed lower than the ratio of ≈45 achieved in our previous work (Kühn et al. 2022) by cyclically switching the electron-beam energy between ion breeding and probing energy after a long parameter optimization. This time, since switching tests showed a severe loss of Fe XVII ions, we decided to use a constant electron-beam energy of 3500 eV, well above that of dielectronic recombination satellites. The present signal-to-noise ratio and resolving power of 13,000 were sufficient for our reported accuracy.

The P04 monochromator was scanned over ranges covering $3s-2p$ (3G and 3F), $3d-2p$ (3C and 3D), $3p-2s$ (3A and 3B), and $4d-2p$ transitions (4C and 4D) of Fe XVII. Fluorescence was collected in the SDDs for 10–15 s at each monochromator step. The count rate for each transition is directly proportional to the respective oscillator strength, and we can see transitions with excitation rates about 4–80 times lower than that of the 3C transition. Scans of each line were therefore repeated as needed to obtain good statistics. This also yielded adequate statistics at each step for the Au $4f_{7/2}$ photoelectron peak position determination needed for the nominal monochromator photon-energy scale correction. To construct the spectrum for a single transition, as depicted in Figure 2, all photons detected in the SDDs within a 50 eV region of interest centered around the expected energy are summed as a function of the monochromator energy. A representative scan for each of these lines is shown in Figure 2. The transition energies of the Fe XVII lines were determined using a maximum-likelihood fit of Voigt profiles added to the linear background term arising from electron-impact excitation using the cash statistic (Cash 1979; Kaastra 2017). The Voigt function is a convolution of Lorentzian and Gaussian functions. The Gaussian contributions to the line width arise from the limited resolution of the monochromator and the thermal motion of the ions (Hoesch et al. 2022). The Lorentzian width, as shown in Kühn et al. (2022), stems from the natural line width of the transition and a pseudo-Lorentz instrumental component due to X-ray diffraction at beamline components (Follath & Balzer 2010). Given the possible energy-dependent

Table 1
Experimental and Calculated Transition Energies from This Work in Comparison with Previous Experiments, Astrophysical Observations, and Other Predictions

Line	Term	Configuration	This Work			Previous Experiments		Observations	
			Experiment	Large CI[a]	FAC-MBPT[b]	BW94[c]	B98[d]	Hinode[e]	SMM[f]
3G	$^3P_1$	$[1s^22s_{1/2}^2 2p_{1/2}^2 2p_{3/2}^3 3s_{1/2}]_1$	727.073(15)	727.086	727.084	727.01(4)	727.14(4)	727.14	727.14
				(−0.013)	(−0.011)	(0.06)	(−0.06)	(−0.06)	(−0.06)
3F	$^1P_1$	$[1s^22s_{1/2}^2 2p_{1/2} 2p_{3/2}^4 3s_{1/2}]_1$	739.067(15)	739.034	739.002	739.23(13)	738.88(9)	739.07	739.10
				(0.033)	(0.065)	(−0.17)	(0.19)	(−0.01)	(−0.03)
3D	$^3D_1$	$[1s^22s_{1/2}^2 2p_{1/2}^2 2p_{3/2}^3 3d_{5/2}]_1$	812.417(13)	812.418	812.363	812.21(11)	812.43(11)	812.37	812.74
				(−0.001)	(0.054)	(0.21)	(−0.01)	(0.05)	(−0.33)
3C	$^1P_1$	$[1s^22s_{1/2}^2 2p_{1/2} 2p_{3/2}^4 3d_{3/2}]_1$	825.870(12)	825.852	825.765	826.07(6)	825.79(6)	825.85	825.90
				(0.019)	(0.106)	(−0.20)	(0.08)	(0.02)	(−0.03)
3B	$^3P_1$	$[1s^22s_{1/2} 2p_{1/2}^2 2p_{3/2}^6 3p_{1/2}]_1$	892.496(10)	892.490	892.446	892.68(13)	892.49(19)	892.61	892.61
				(0.007)	(0.050)	(−0.18)	(0.01)	(−0.12)	(−0.12)
3A	$^1P_1$	$[1s^22s_{1/2} 2p_{1/2}^2 2p_{3/2}^6 3p_{3/2}]_1$	896.774(10)	896.770	896.752	896.81(6)	896.81(13)	896.81	896.88
				(0.004)	(0.022)	(−0.04)	(−0.04)	(−0.04)	(−0.10)
4D	$^3D_1$	$[1s^22s_{1/2}^2 2p_{1/2}^2 2p_{3/2}^3 4d_{5/2}]_1$	1010.983(16)	⋯	1010.921	⋯	1010.80(8)	1010.96	1011.04
					(0.062)		(0.19)	(0.02)	(−0.06)
4C	$^1P_1$	$[1s^22s_{1/2}^2 2p_{1/2} 2p_{3/2}^4 4d_{3/2}]_1$	1022.639(16)	⋯	1022.552	⋯	1022.63(8)	1022.62	1022.80
					(0.087)		(0.01)	(0.02)	(−0.16)

Notes. All values in eV. Values in parentheses following the measured values give total uncertainties and parentheses below the measured values indicate absolute differences from the present measurements.
[a] Large CI calculations, method is from Cheung et al. (2021).
[b] CI + second-order MBPT of FAC, method is from Gu et al. (2006).
[c] EBIT measurements by Beiersdorfer & Wargelin (1994).
[d] EBIT measurements by Brown et al. (1998).
[e] Solar observations by Hinode: Del Zanna & Ishikawa (2009).
[f] Solar observations by SMM: Phillips et al. (1982).

contributions to line widths from beamline components, we chose to leave all parameters of the Voigt profile unconstrained during our fitting procedure for determining the line centroids.

Table 1 presents the results for eight Fe XVII lines and their associated uncertainties from errors in the centroid determination of calibration lines, the dispersion fit 1σ confidence band, and the centroid determination of each Fe XVII line, which is typically in the range of 1–3 meV. The total systematic uncertainties of the calibration are estimated to reach levels of 10–15 meV. As mentioned before, the angular encoder interpolation error induces oscillations of the nominal monochromator photon energy scale up to ±70 meV in the 650–1150 eV energy range. While accurate reference energies and the corrections from ASPHERE to the photon-energy axis help mitigate these oscillations, ∼10%–20% (7–14 meV) residual variations still remain in the corrected monochromator photon-energy scale. A potential source of these could be the limited resolution of the Keithley 6517 voltage source biasing the gold target. Despite using a seven-digit calibrated voltmeter (Agilent 3458a), the voltage source operates in 5 mV steps within the 100 V range, limiting our electron kinetic energy measurements. Further systematics arise from the frequent switching of the voltage range of this bias supply needed to cover the monochromator range of 600–1150 eV, requiring separate calibration for each voltage range. Unfortunately, we could only calibrate the bias supply in a narrow 20 V range. Moreover, unmeasured fluctuations in the voltages applied to the inner and outer hemispheres of the electron spectrometer may have introduced additional systematic uncertainties. The dimensional stability of its electron-optics components is affected by thermal drifts caused by varying ambient conditions at ppm levels to which we are already sensitive. Note that we also fit our data with skewed Voigt profiles, allowing for a nonzero skewness, thus accounting for any line asymmetries that may exist due to monochromator imperfections (Perry-Sassmannshausen et al. 2021; Hoesch et al. 2022; Togawa et al. 2023). These tests resulted in changes to the line centroids of less than ∼1 meV, which is negligible considering the total uncertainty of our measurements. We considered whether lines from contaminant ions of oxygen, fluorine, or neon originating from residual calibration gases could lead to systematic errors in any of our transition-energy determinations. Because these lines have known transition energies, and because of the extremely high resolving power (13,000) attained in our experiment, we ruled out any significant effect from such contamination. After conservatively considering all these sources, our present uncertainties are a factor of 4–20 smaller than those of previously reported experiments (Beiersdorfer & Wargelin 1994; Brown et al. 1998).

3. Discussion of the Results

We compare the present results in Figure 2 and Tables 1 and 2 with earlier experimental data, observations, and predictions, including our own. Our calculations employ the latest version of our highly scalable parallel CI code (Cheung et al. 2021; see Appendix). Optimization of the basis-set construction allowed faster convergence with the principal quantum number n than in our prior work (see supplementary material of Kühn et al. 2022) while including higher partial waves (h, i, and k), and a larger number of reference configurations of even and odd parity. Table 3 shows the QED and other contributions in cm^{-1} for the measured transitions. Column $17g$ shows the results obtained with the $17spdfg$ basis set (see the Appendix);

Table 2
Continuation of Table 1

Line	Large CI[a] (old)	Exp.[b]	NIST ASD[c]	AtomDB[d] CI	CHIANTI[e] MRMP	CHIANTI[f] AS	SPEX[g]	W16[h] MBPT	S15[i] MBPT	G05[j] MBPT	A04[k] MCDF
3G	726.97	727.11	727.14	725.79	727.06	727.48	727.18	726.78	⋯	727.12	725.38
	(0.10)	(−0.03)	(−0.07)	(1.28)	(0.01)	(−0.41)	(−0.11)	(0.29)	...	(−0.05)	(1.70)
3F	738.91	739.04	739.05	738.01	739.00	738.21	738.88	738.72	⋯	739.06	736.05
	(0.16)	(0.03)	(0.01)	(1.06)	(0.07)	(0.85)	(0.19)	(0.34)	...	(0.01)	(3.02)
3D	812.32	812.41	812.37	811.70	812.41	813.65	812.48	812.04	812.57	812.44	811.08
	(0.10)	(0.01)	(0.05)	(0.72)	(0.01)	(−1.23)	(−0.06)	(0.37)	(−0.15)	(−0.02)	(1.34)
3C	825.76	825.83	825.70	825.83	825.76	827.52	826.01	825.39	825.89	825.70	825.01
	(0.11)	(0.04)	(0.17)	(0.04)	(0.11)	(−1.65)	(−0.14)	(0.48)	(−0.02)	(0.17)	(0.86)
3B	⋯	⋯	892.50	894.25	892.41	895.55	892.61	892.21	⋯	892.40	894.25
	...	...	(−0.00)	(−1.75)	(0.08)	(−3.05)	(−0.12)	(0.29)	...	(0.10)	(−1.75)
3A	⋯	⋯	896.90	898.54	896.67	899.85	897.14	896.46	⋯	896.62	898.55
	...	...	(−0.13)	(−1.77)	(0.10)	(−3.08)	(−0.36)	(0.31)	...	(0.15)	(−1.77)
4D	⋯	⋯	1011.00	1009.79	⋯	1012.03	1011.29	1010.53	⋯	⋯	1009.22
	...	...	(−0.02)	(1.19)	...	(−1.05)	(−0.31)	(0.46)	...	...	(1.76)
4C	⋯	⋯	1022.70	1021.76	⋯	1023.64	1022.97	1022.17	⋯	⋯	1020.90
	...	...	(−0.06)	(0.88)	⋯	(−1.00)	(−0.33)	(0.47)	⋯	⋯	(1.74)

Notes. The experimental results are compared with previous predictions, with energy units expressed in eV. Values in parentheses below the predicted values denote the absolute differences from the current measurements.
[a] Large CI: Kühn et al. (2022).
[b] Preliminary critical analysis of Fe XVII spectral data, A. Kramida (2019, private communication).
[c] NIST Atomic Spectroscopy Database: Kramida et al. (2022).
[d] AtomDB Database: Loch et al. (2006; APED: `fe_17_LV_v3_0_4_a.fits`).
[e] Chianti Database with MRMP calculations: Del Zanna & Ishikawa (2009).
[f] Chianti Database with AS calculations: Liang & Badnell (2010).
[g] SPEX database: Gu et al. (2020).
[h] MBPT by Wang et al. (2016).
[i] MBPT by Santana et al. (2015).
[j] MBPT by Gu (2005).
[k] MCDF by Aggarwal et al. (2003).

Table 3
Contributions to the Theoretical Energies (in cm^{-1} above the Ground State) of Fe XVII from an Enlarged Basis Set ($>17g$), Additional Reference Configurations (Extras), and QED in Comparison with Our Measurements and Their Errors in cm^{-1}

Label	This Exp.	Error	ΔPrev. Th.[a]	$17g$	$\geqslant 17g$	Extras	QED	Final	ΔThis Th.[b]	ΔThis Th.[b] (%)
3G	5,864,241	122	841	5,862,842	541	146	814	5,864,343	−102	0.0017
3F	5,960,976	123	1274	5,958,941	558	146	1067	5,960,711	265	0.0045
3F–3G	**96,736**	**174**	**434**	**96,099**	**17**	**0**	**253**	**96,368**	**368**	**0.3800**
3D	6,552,587	103	787	6,552,044	294	104	151	6,552,594	−7	0.0001
3C	6,661,093	96	897	6,660,390	248	5	299	6,660,942	151	0.0023
3C–3D	**108,506**	**141**	**110**	**108,346**	**−46**	**−99**	**148**	**108,348**	**158**	**0.1454**
3B	7,198,469	82	...	7,200,865	573	−28	−2993	7,198,416	53	0.0007
3A	7,232,969	82	...	7,235,357	547	−8	−2958	7,232,938	31	0.0004
3A–3B	**34,500**	**116**	...	**34,492**	**−25**	**20**	**35**	**34,522**	**−22**	**0.0626**

Notes. Note that we used the CODATA2018 (Tiesinga et al. 2021) recommended value of hc to convert experimental values from eV to cm^{-1}. The difference between the three pairs of lines is shown in bold.
[a] This column shows the difference between previous theoretical large CI computations from Kühn et al. (2022) and those of the present experiment.
[b] This column shows the difference between current theoretical large CI computations and those of the present experiment.

column $>17g$, additional contributions from highly excited orbitals up to $24spdfgh21i17k$; "Extras," additional contributions due to the much larger number of configurations included in CI, selected to give the large contributions. The final results are the sum of these three columns and a QED contribution (Tupitsyn et al. 2016). Column [ΔThis Th.] shows differences between the current experiment and theory, and column [ΔPrev. Th.] shows differences from previous calculations presented in Kühn et al. (2022), demonstrating a significant improvement. We estimate the uncertainty in the electronic correlation computations to be approximately 29 meV (∼230 cm^{-1}), primarily arising from the $>17g$ contribution (see Appendix). The difference between theory and experiment is within the combined uncertainties for all six levels. This allows us to estimate the uncertainty of the QED contribution at 30–32 meV (240–260 cm^{-1}), which is the combined theory and experimental uncertainties added in quadrature. We also computed the energies of the 3A and 3B

levels for the first time. The $2s-3p$ lines (3A and 3B), which involve a $2s$ electron, have the largest QED contributions ($\sim$370 meV, or $\sim$3000 cm^{-1}), while for $3s-2p$ transitions 3G and 3F as well as $3d-2p$ ones (3C and 3D) they are much smaller. From the 3A and 3B results, we thus estimate a relative QED accuracy of 8%.

As shown in Table 1, line 3F, close to the He-like F Kα calibration line, shows a larger absolute deviation of about 33 meV from the large CI prediction, while the remaining measured lines remain below $\sim$10–20 meV. Unfortunately, line 3F was measured only once, unlike the others, which were scanned at least four to five times. We explored several plausible explanations for the 3F discrepancy. One possible source of the discrepancy could be the simultaneous excitation of high-n Rydberg lines of O VII within the scan range of line 3F, which could lead to a shift of the 3F centroid. Furthermore, we considered lines from the lower charge states, Fe X, Fe VIII, and Fe VII, which fall within the 3F scan range. Despite the relatively low abundance of these charge states in our experiment, they can potentially influence the 3F line due to their strong oscillator strengths. Although the theoretical line positions and oscillator strengths of these low charge states are calculated by Gu et al. (2006), they have never been compared experimentally, making it difficult to estimate their influence on the 3F position. We also investigated the possibility of magnetically induced mixing of the $J=0$ and $J=1$ ($2p_{1/2}^{-1}\,3s_{1/2}$) excited states (Beiersdorfer et al. 2003), which might shift the energy of the $J=1$ state sufficiently to introduce a systematic error in our measurement of 3F. However, measurements by Beiersdorfer et al. (2016) show a separation of $\sim$1.2 eV between these states, making strong magnetic-field-induced mixing unlikely. We performed FAC calculations for atoms in strong magnetic fields to verify this, finding shifts on the order of 10 μ eV for the field strength in PolarX-EBIT, demonstrating that this effect is not important in our experiment. The decrease in reflectivity of the platinum-coated diffraction grating over the 3F scan range could slightly affect the centroid position determination at 739 eV. Based on simulations we estimate this effect to be smaller than 0.1 meV.

We also consider the differences between the three line pairs, as they are more sensitive to QED effects than absolute energies. Table 3 shows that the largest uncertainty, caused by the uncertainty in the basis-set convergence, is common to each of the pairs. This significantly reduces the uncertainty of electronic correlations to better than 6 meV (50 cm^{-1}) for the energy difference. Both (3A–3B) and (3C–3D) are in excellent agreement with our present as well as previous predictions (Kühn et al. 2022). For (3G–3F), the deviation is 46 meV (about 2σ) and can be attributed to the factors discussed above for line 3F. It is interesting to note that our measured 3F energy is in much better agreement with solar observations (Phillips et al. 1982; Del Zanna & Ishikawa 2009) than with our calculations. Nevertheless, our present calculations of the ground state transitions show an order of magnitude smaller deviation from our experimental results compared to our prior predictions (Kühn et al. 2022). This represents a benchmark with our experimental data at the level of 10–20 ppm, an unprecedented agreement for a neon-like system to the best of our knowledge.

Besides CI, we performed calculations using a combination of conventional CI and second-order many-body perturbation theory (MBPT) with the Flexible Atomic Code (FAC; Gu 2008). Details of this method are described in Gu (2005), Gu et al. (2006), and recently in Steinbrügge et al. (2022). In these calculations, we included frequency-dependent generalized Breit interactions (Breit 1929) in both the CI expansion and the MBPT corrections, as well as self-energy and vacuum polarization calculated using the QED operator model of Shabaev et al. (2018). These predictions demonstrate a reasonable agreement with our experimental data, with the largest discrepancy of about 100 meV observed for line 3C. We compared our results with other CI+MBPT data available in the literature (Gu 2005; Santana et al. 2015; Wang et al. 2016), showing maximum deviations of up to 0.5 eV. The origin of the discrepancy between our CI+MBPT calculations and the previously published ones is unclear. We have also observed departures from the predictions of multiconfiguration Dirac–Fock (MCDF) and autostructure (AS) calculations (Aggarwal et al. 2003; Loch et al. 2005; Liang & Badnell 2010), with deviations reaching up to 1–3 eV. However, we note that the atomic structures used in these calculations were necessarily small to facilitate their use in R-matrix collision calculations, which are computationally more demanding compared to atomic structure calculations. Other accurate predictions for Fe XVII from multireference Møller–Plesset (MRMP) are reported in Del Zanna & Ishikawa (2009) and included in the CHIANTI code. They show very good agreement with our experimental data.

We compare our results with laboratory data from Beiersdorfer & Wargelin (1994) and Brown et al. (1998). Both works measured electron-impact spectra of Fe XVII under similar experimental conditions in the Lawrence Livermore National Laboratory EBIT facility using a crystal spectrometer employing a cesium acid phthalate crystal for the wavelength range of the lines presently discussed. Both measurements have carefully concatenated several spectra from different wavelength ranges and calibrated them against reference lines of hydrogenic and helium-like oxygen, fluorine, and neon, similar to our work. Nevertheless, these two measurements are themselves marginally inconsistent with each other within their quoted uncertainties. Furthermore, we find that our measurements are also marginally inconsistent with both these previous measurements within uncertainties. The source of these marginal inconsistencies is unknown.

We also compare our results with data from widely used databases and plasma codes. The NIST Atomic Spectroscopy Database (ASD; Kramida et al. 2022) values showed significant deviations for lines 3C and 3A. However, when critically evaluated $n=3-2$ data by the authors of the NIST ASD (A. Kramida 2019, private communication) were considered, we found a much better agreement with our experimental results (see Table 2). Comparison with AtomDB (Foster et al. 2012), CHIANTI (Del Zanna et al. 2021), and SPEX (Kaastra et al. 1996) databases and plasma codes revealed discrepancies as large as 1–2 eV. SPEX numbers showed better agreement with our results than those found in AtomDB, since SPEX has updated Fe-L atomic data (Gu et al. 2019, 2020, 2022), which were mainly calculated using FAC. Although the Astrophysical Plasma Emission Database (APED) version in AtomDB shows different values in its online webguide version (2.0.1) [14] and its pyatomdb version (3.0.4), the theoretical source is in both cases Loch et al. (2005), which uses the CI method, and disagrees by up to

[14] http://www.atomdb.org/Webguide/webguide.php

1–2 eV from our results, as shown in Table 2. CHIANTI provides two sources for the energies: AS theory (Liang & Badnell 2010), and the more accurate set of data from MRMP theory (Del Zanna & Ishikawa 2009). Note that the theoretical energy level data in AtomDB and Chianti are not used when generating model spectra when more accurate experimental or observational values exist. AtomDB replaces the most important transition energies of Fe XVII with the Brown et al. (1998) values, whereas CHIANTI uses the observed transition energies from solar observation (Del Zanna & Ishikawa 2009).

Overall, most experimental and observational data agree with our experiment within 0.1 eV on average, well within the error bars of earlier works. However, there are substantial discrepancies with predictions from certain theoretical models, exceeding the margins of error associated with the experimental results. This highlights the urgent need to update the aforementioned databases to avoid pitfalls in astrophysical spectrum modeling and interpretation of observational data.

4. Summary and Conclusions

We presented high-precision transition-energy measurements of eight strong, astrophysically preeminent Fe XVII transitions required for plasma diagnostics. Our approach combined resonant photoexcitation of Fe XVII and narrow H-like and He-like transitions with high-resolution photoelectron spectroscopy (Rossnagel et al. 2001). This eliminates a very common source of systematic errors found even in advanced monochromators, namely quasiperiodic encoder interpolation errors (Follath & Balzer 2010; Krempaský et al. 2011). As a result, our Fe XVII measurements represent a significant improvement in accuracy compared to previous experimental references, achieving an average enhancement of almost an order of magnitude. The uncertainties now stand at 10–15 meV, which translates to Doppler shifts of approximately ± 5 km s^{-1}. A further improvement in accuracy by another order of magnitude will require incorporating high-resolution/high-stability voltage sources and more accurate voltmeters at ASPHERE to eliminate systematic errors associated with knowledge of the bias voltages.

We have also improved our high-precision calculations by an order of magnitude in comparison with previous best calculations (Cheung et al. 2021; Kühn et al. 2022). This improvement allowed us, for the first time, to test the accuracy of QED corrections to the transition energies of a complicated 10-electron system. We expect that the achieved QED accuracy is applicable to a broad range of ions of intermediate degrees of ionization that can be treated with our large-scale CI or CI+all-order approaches. This has significant implications for predicting energy levels in systems where no experimental data are available for a wide range of applications in astrophysics, plasma physics, and atomic clock development (King et al. 2022). The established QED accuracy is deemed sufficient for high-precision prediction of HCI clock transitions (Kozlov et al. 2018). Improved accuracy of the experimental values would allow us to further decouple the uncertainty due to basis-set convergence from the uncertainty in the QED and improve theory predictions.

Our improved transition-energy measurements for Fe XVII are sufficiently accurate that the uncertainties are no longer a significant part of the error budget for present or future planned astrophysical instruments, such as Chandra HETGS, XMM-Newton RGS, XRISM (Tashiro et al. 2018), Athena (Pajot et al. 2018), LEM (Kraft et al. 2022), HUBS (Cui et al. 2020), Arcus (Heilmann et al. 2022), HiReX (Nicastro et al. 2021), and Lynx (Schwartz et al. 2019). Future campaigns of similar measurements of prominent transitions in key ions (especially Fe-L shell ions) would be of great utility and could easily be directly included in commonly used astrophysical plasma spectral databases.

The closeness of our large CI calculations to our measured values, with the worst deviation at line 3F of 33 meV amounting to a Doppler shift of only 13 km s^{-1}, shows that such well-converged calculations are sufficiently accurate to be readily used in spectral databases. While there is no reason for this in the case of the lines measured in the present work, when accurate measurements are not available, similarly well-converged results could be used for other transitions of Fe XVII and many other ions. By including a very large number of configurations, our agreement becomes significantly better than that of other well-performing methods, such as results from less-converged large CI, MBPT, and MRMP calculations. For Fe XVII, our calculations are more accurate than even the best measurements for Fe-L shell transitions in Li-like through F-like ions (Brown et al. 2002). This suggests a near-future research program composed of comprehensive large CI calculations of transition energies for all ions of astrophysical interest up to Ne-like, supplemented by targeted experiments aimed at measuring the most important transition energies.

Acknowledgments

This research was funded by the Max Planck Society (MPG) and the German Federal Ministry of Education and Research (BMBF) under project 05K13SJ2. C.S. acknowledges support from NASA under grant No. 80GSFC21M0002 and MPG. F.S.P. and M.A.L. acknowledge support from the NASA Astrophysics Program. The theoretical work has been supported by the US NSF grants Nos. PHY-2012068 and PHY-2309254 and US Office of Naval Research grant No. N00014-20-1-2513. Calculations were performed in part using the computing resources at the University of Delaware, in particular the Caviness and DARWIN high-performance computing clusters. M.S.S. thanks MPIK for the hospitality. We thank DESY (Hamburg, Germany), a member of the Helmholtz Association HGF, for the provision of experimental facilities. Parts of this research were carried out at PETRA III. We thank the P04 team at PETRA III for their skillful and reliable work. We also thank the anonymous referees whose comments and suggestions helped improve and clarify this manuscript.

Appendix
Large-scale CI Calculations

In this work, we conducted extensive high-precision calculations of Fe XVII. We start from the solution of the Dirac–Hartree–Fock equations in the central field approximation to construct the one-particle orbitals. Calculations are carried out using a CI method, correlating all 10 electrons. Breit interaction is included in all calculations. QED corrections are taken from the previous work (Kühn et al. 2022) except for the levels with a $2s$ hole, which were not computed in 2022. The same method is used in all QED calculations (Tupitsyn et al. 2016). The CI wave function is obtained as a linear combination of all distinct states of a given angular momentum

J and parity:

$$\Psi_J = \sum_i c_i \Phi_i. \tag{A1}$$

The low-lying energies and wave functions are determined by solving the time-independent multielectron Schrödinger equation

$$H\Phi_n = E_n \Phi_n. \tag{A2}$$

Expanding the previous work (Kühn et al. 2022), we perform several calculations optimizing the basis-set convergence, including higher partial waves up to k orbitals, and significantly expanding the set of reference configurations until convergence is reached in these parameters as well.

We have shown a comparison of our theoretical results for six transitions measured in this work with the experiment in the main text. We note that such a larger-scale computation of the 4C and 4D levels is beyond the capabilities of available computational resources (32 TB of memory and about 2000 CPUs on our largest available partition). Computing higher-lying levels requires computing of all the lower-lying levels with the same angular momentum and parity, drastically increasing memory requirement.

To test the consistency of our approach, we compare the data for the even and larger number of odd levels in Table 4 with the preliminary critical analysis of Fe XVII spectral data by A. Kramida (2019, private communication). These data generally agree well with our experiment (except for levels with a $2s$ hole), so they serve as a good general reference for other levels. The six levels measured in this work are shown in bold. The final values are given in cm^{-1} in Table 4 in the column "Final." The difference between the final values and the experimental values in cm^{-1} and percentage are given in the last two columns.

We will discuss a complete assessment of the main contributions to the energies, including the basis-set construction, the inclusion of extra configurations, and QED. We find excellent agreement with experiments for all energies, at the level of 0.0004% for some levels. With the high level of accuracy attained, we are able to test QED contributions in the calculations of multielectron systems for the first time.

Computation. We consider Fe XVII as a system with 10 valence electrons and start with all possible single and double excitations to any orbital up to 17*spdfg* from the $1s^22s^22p^6$ and $1s^22s^22p^53p$ even-parity reference configurations, and the $1s^22s^22p^53s$, $1s^22s^22p^53d$, and $1s^22s2p^63p$ odd-parity reference configurations. For example, a single excitation from the reference configurations $2s^22p^6$ can include promoting an electron from the $2s$ or $2p$ orbitals to any orbital up to $17s$, $17p$, ... $17g$, with $2s^22p^510p$ or $2s2p^617s$ as example outcomes. We designate the basis set by the highest principal quantum number and the highest partial wave included. For example, $17g$ means that all orbitals up to $n = 17$ are included for *spdfg* partial waves. Note that $1s^2$ is removed from all the designations to save space.

The base calculation for the energy levels is done with a $17g$ basis set and is listed in cm^{-1} in Table 4 in column "$17g$." The contributions to the energy levels from expanding the basis set to $20g$ and $24g$ are in the columns "$+20g$" and "$+24g$," respectively. The largest difference between the $23g$ and $24g$ calculations was 3 cm^{-1}, so the basis set at the level of *spdfg* partial waves is considered sufficiently saturated. We note that although the 24*spdfg* basis was also used in Kühn et al. (2022), we constructed a more compact basis in the present work, to significantly improve convergences with the principal quantum number n. The basis is constructed in the 5 a.u. cavity, while the basis in Kühn et al. (2022) was constructed in a 20 a.u. cavity, with additional differences in the constructions of the higher partial-wave orbitals. A detailed comparison of the two computations confirms much better convergence properties of the present basis. We note very large computational resources needed for a basis-set expansion, especially for the inclusion of higher partial waves.

Contributions to higher partial waves are considered in the next six columns of Table 4. We calculated the contributions of extending the base $17g$ basis set to include up to $17h$ orbitals and listed them in column "$+17h$." Next, we successively increase the principal quantum number and increase the basis set up to $24h$. The contributions from (18 to 20)h orbitals and (21–24)h orbitals are given in columns "$+20h$" and "$+24h$," respectively. The largest difference between $23h$ and $24h$ calculations was 9 cm^{-1}, so the energies of including the higher h orbitals have also converged sufficiently. We note that a large fraction of the nh contribution comes from very high-n orbitals, so the inclusion of the first few h orbitals does not give correct results for this partial wave. This effect is exacerbated for the i and k orbitals, where more of the contribution is expected to come from $n > 20$ even with the present compact basis.

The same procedure was used to obtain contributions from the i orbitals up to $21i$ and k orbitals up to $17k$ and are listed under columns "$+21i$" and "$+17k$," respectively. Contributions from including i orbitals up to the same principal quantum number $n = 17$ as the base run are listed in column "$+17i$. Due to the high computational demand for higher partial-wave calculations, we did not perform calculations for odd-parity states at the level of $21i$. Instead, we set the contributions of $21i$ to the odd-parity energies to be the average of the even-parity state contributions, which was 81 cm^{-1}. Contributions from k orbitals were already at a level of convergence around 15 cm^{-1} at $21i$.

We note that we have performed detailed convergence studies computing a separate contribution for each nl for the last few principal quantum numbers to evaluate convergence. Based on these data, we conservatively estimate the missing higher g orbital contribution at 5 cm^{-1}, higher h orbital contribution at 20 cm^{-1}, and higher i orbital contribution at 50 cm^{-1}. It appears that $17k$ is not sufficiently converged. Table 4 shows that the contribution of all ni orbitals is about $1/2$ of the nh contribution. Conservatively assuming a similar convergence pattern for higher partial waves gives 70 cm^{-1} for the k partial wave and a similar total contribution for all the other partial waves. The total uncertainty due to the convergence of the basis set is then on the order of 230 cm^{-1}. However, we note that the incomplete convergence of the basis is expected to cause a systematic shift of data for all levels; i.e., all energy values will be larger, with some smaller variances between the levels. It is possible that the partial-wave convergence is faster and the overall shift is smaller; therefore, we only use the above estimate to make an accuracy evaluation but do not shift the theory values. We note that overall $+100\,\mathrm{cm}^{-1}$ shift of all of our values would improve the agreement of our data with the present experiment; however, this is the level of the experimental precision at 1σ so improved

Table 4
Contributions to Fe XVII Energies Calculated with Increased Basis Sets and Number of Configurations

Configuration		Expt[a]	Δ[b]	17g	+20g	+24g	+17h	+20h	+24h	+17i	+21i	+17k	QED	Extras	Final	Δ	Δ (%) Present
$2s^22p^6$	$^1S_0$	0	0	0	0	0	0	0	0	0	0	0	0	0	0	0	0
$2s^22p^53p$	$^3S_1$	6,093,295	1124	6,092,365	44	20	278	58	45	64	86	8	70	107	6,093,143	152	0.002%
$2s^22p^53p$	$^3D_2$	6,121,484	988	6,120,688	38	18	252	51	40	56	77	4	56	⋯	6,121,280	204	0.003%
$2s^22p^53p$	$^3D_3$	6,134,539	1015	6,133,678	41	19	258	54	42	58	81	5	107	⋯	6,134,345	194	0.003%
$2s^22p^53p$	$^1P_1$	6,143,639	1013	6,142,785	39	18	253	52	40	56	78	4	93	⋯	6,143,417	222	0.004%
$2s^22p^53s$	2	5,849,216	1134	5,847,527	38	16	269	52	35	63	81	8	813	149	5,849,052	164	0.003%
$2s^22p^53s$	**$^3P_1$**	**5,864,502**	**1102**	**5,862,842**	**37**	**15**	**258**	**50**	**34**	**60**	**81**	**7**	**814**	**146**	**5,864,343**	**158**	**0.003%**
$2s^22p^53s$	**$^1P_1$**	**5,960,742**	**1040**	**5,958,941**	**41**	**18**	**259**	**55**	**37**	**60**	**81**	**7**	**1067**	**146**	**5,960,711**	**31**	**0.001%**
$2s^22p^53d$	$^3P_1^o$	6,471,640	1148	6,470,765	51	24	138	65	47	22	81	−2	95	139	6,471,426	214	0.003%
$2s^22p^53d$	$^3P_2^o$	6,486,183	1007	6,485,436	51	24	121	65	47	17	81	−4	109	139	6,486,086	97	0.001%
$2s^22p^53d$	$^3F_4^o$	6,486,720	920	6,486,064	51	24	90	65	47	7	81	−7	105	142	6,486,669	51	0.001%
$2s^22p^53d$	$^3F_3^o$	6,492,651	856	6,492,060	50	23	66	64	46	−2	81	−10	102	138	6,492,621	30	0.000%
$2s^22p^53d$	$^1D_2^o$	6,506,537	855	6,505,941	50	23	62	64	46	−3	81	−10	107	138	6,506,500	37	0.001%
$2s^22p^53d$	$^3D_3^o$	6,515,203	807	6,514,654	50	23	49	63	46	−8	81	−12	107	136	6,515,189	14	0.000%
$2s^22p^53d$	**$^3D_1^o$**	**6,552,503**	**703**	**6,552,044**	**51**	**24**	**49**	**65**	**47**	**−9**	**81**	**−12**	**151**	**104**	**6,552,594**	**91**	**0.001%**
$2s^22p^53d$	$^3F_2^o$	6,594,309	802	6,593,569	55	26	71	69	50	0	81	−9	355	138	6,594,404	95	0.001%
$2s^22p^53d$	$^3D_2^o$	6,600,998	938	6,600,124	54	26	80	69	49	2	81	−8	349	137	6,600,962	36	0.001%
$2s^22p^53d$	$^1F_3^o$	6,605,185	857	6,604,381	54	26	56	69	49	−6	81	−11	363	136	6,605,198	13	0.000%
$2s^22p^53d$	**$^1P_1^o$**	**6,660,770**	**574**	**6,660,390**	**54**	**26**	**11**	**68**	**49**	**−23**	**81**	**−17**	**299**	**5**	**6,660,942**	**172**	**0.003%**
$2s2p^63p$	**$^3P_1^o$**	**7,199,200**	⋯	**7,200,865**	**47**	**30**	**248**	**56**	**38**	**65**	**81**	**8**	**−2993**	**−28**	**7,198,416**	**784**	**0.011%**
$2s2p^63p$	$^3P_2^o$	⋯	⋯	7,219,595	48	31	251	57	39	66	81	8	−2944	−36	7,217,197	⋯	
$2s2p^63p$	**$^1P_1^o$**	**7,233,292**	⋯	**7,235,357**	**46**	**30**	**235**	**54**	**35**	**61**	**81**	**6**	**−2958**	**−8**	**7,232,938**	**354**	**0.005%**

Notes. The results are compared with the preliminary critical analysis of Fe XVII spectral data by A. Kramida (2019, private communication). All energies are given in cm^{-1}. The basis set is designated by the highest principal quantum number and the highest partial wave included. For example, 17g means that all orbitals up to $n = 17$ are included for *spdfg* partial waves. The last two columns show the differences between the present computations with A. Kramida (2019, private communication) in cm^{-1} and %, respectively. The measured transitions are highlighted in bold.

[a] A. Kramida (2019, private communication).

[b] Kühn et al. (2022). This column shows the difference between previous theoretical large CI computations from Kühn et al. (2022) and the preliminary critical analysis of Fe XVII spectral data by A. Kramida (2019, private communication).

experimental precision is needed to definitively test the basis-set convergence.

Additionally, an extensive evaluation of the configuration weights was done to include important configurations in the list of basic reference configurations used to construct a final set of configurations. The weights of configurations signify the configuration's contribution to the corresponding wave functions and are calculated for each configuration Φ_i as $|c_i|^2$ from Equation (A1). These calculations are done by allowing single and double excitations to a much smaller $12g$ basis set since the size of the computational problem will become prohibitive when additional reference configurations are included. The total contributions to including these extra configurations are given in the column "Extras" in Table 4. Beyond the initial two even- and three odd-parity configurations, we systematically included an additional 12 even- and nine odd-parity reference configurations. Note that energies were calculated only for two even-parity levels to save computational resources and allow for additional reference configurations. The inclusion of these extra configurations contributes about 100 cm^{-1} shift to the energies and accounts for an additional 2 million relativistic configurations. Note also that these contributions would also be higher if the calculations were done with a larger basis set. We estimate an uncertainty from the convergence of the CI configuration set at the level of 50 cm^{-1}, which is essentially negligible in comparison with the basis-set convergence uncertainty. We note that missing contributions can be both positive and negative in this case.

Analysis of contributions to the 3F–3G, 3C–3D, and 3A–3B line differences given in the main text Table 3 shows that the basis-set expansion contribution effectively cancels for similar configurations; it is less than 50 cm^{-1} for all three cases. We also find that QED contributions play a major role in the 3F–3G energy difference. For 3C–3D, the contributions from the basis-set expansion and the addition of extra configurations essentially cancel out the QED. In the 3A–3B difference, the basis-set and extra configuration contributions cancel, leaving a shift from the QED. Therefore, comparing the differences in the energy values for similar configurations provides important additional information. It would be very useful to improve the uncertainty of the experiment as well as carry out such comparison in other ions with different degrees of ionization with 7–10 electrons.

ORCID iDs

Chintan Shah https://orcid.org/0000-0002-6484-3803
Moto Togawa https://orcid.org/0000-0003-4571-2282
Marc Botz https://orcid.org/0009-0003-8574-4542
Jonas Danisch https://orcid.org/0009-0002-2934-6016
Joschka J. Goes https://orcid.org/0009-0006-2461-9571
Sonja Bernitt https://orcid.org/0000-0002-1976-5121
Marleen Maxton https://orcid.org/0009-0005-9076-3101
Kai Köbnick https://orcid.org/0009-0003-0805-2438
Jens Buck https://orcid.org/0000-0002-5545-0637
Jörn Seltmann https://orcid.org/0009-0009-7545-2101
Moritz Hoesch https://orcid.org/0000-0002-0114-2110
Ming Feng Gu https://orcid.org/0000-0001-9136-8449
F. Scott Porter https://orcid.org/0000-0002-6374-1119
Thomas Pfeifer https://orcid.org/0000-0002-5312-3747
Maurice A. Leutenegger https://orcid.org/0000-0002-3331-7595
Charles Cheung https://orcid.org/0000-0002-3724-3730
Marianna S. Safronova https://orcid.org/0000-0002-1305-4011
José R. Crespo López-Urrutia https://orcid.org/0000-0002-2937-8037

References

Aggarwal, K. M., Keenan, F. P., & Msezane, A. Z. 2003, ApJS, 144, 169
Barret, D., Lam Trong, T., den Herder, J.-W., et al. 2016, Proc. SPIE, 9905, 99052F
Behar, E., Cottam, J., & Kahn, S. 2001, ApJ, 548, 966
Beiersdorfer, P., Behar, E., Boyce, K., et al. 2002, ApJL, 576, L169
Beiersdorfer, P., Bitter, M., Von Goeler, S., & Hill, K. 2004, ApJ, 610, 616
Beiersdorfer, P., Bode, M. P., Ishikawa, Y., & Diaz, F. 2014, ApJ, 793, 99
Beiersdorfer, P., Brown, G. V., & Laska, A. 2015, JPhCS, 583, 012022
Beiersdorfer, P., Crespo López-Urrutia, J. R., & Träbert, E. 2016, ApJ, 817, 67
Beiersdorfer, P., Hell, N., & Lepson, J. 2018, ApJ, 864, 24
Beiersdorfer, P., Lepson, J. K., Gu, M. F., & Bitter, M. 2017, ApJ, 850, 57
Beiersdorfer, P., Schweikhard, L., Liebisch, P., & Brown, G. V. 2008, ApJ, 672, 726
Beiersdorfer, P., Scofield, J. H., & Osterheld, A. L. 2003, PhRvL, 90, 235003
Beiersdorfer, P., & Wargelin, B. J. 1994, RScI, 65, 13
Bernitt, S., Brown, G. V., Rudolph, J. K., et al. 2012, Natur, 492, 225
Bozzo, E., Huenemoerder, D. P., Produit, N., et al. 2023, MNRAS, 522, L66
Breit, G. 1929, PhRv, 34, 553
Brinkman, A., Behar, E., Güdel, M., et al. 2001, A&A, 365, L324
Brown, G., Beiersdorfer, P., Chen, H., Chen, M., & Reed, K. 2001a, ApJL, 557, L75
Brown, G., Beiersdorfer, P., & Widmann, K. 2001b, PhRvA, 63, 032719
Brown, G., Beiersdorfer, P., Liedahl, D., Widmann, K., & Kahn, S. 1998, ApJ, 502, 1015
Brown, G. V., Beiersdorfer, P., Chen, H., et al. 2006, PhRvL, 96, 253201
Brown, G. V., Beiersdorfer, P., Liedahl, D. A., et al. 2002, ApJS, 140, 589
Cash, W. 1979, ApJ, 228, 939
Chen, G. X., & Pradhan, A. K. 2002, PhRvL, 89, 013202
Cheung, C., Safronova, M., & Porsev, S. 2021, Symm, 13, 621
Cui, W., Chen, L. B., Gao, B., et al. 2020, JLTP, 199, 502
Del Zanna, G., Dere, K. P., Young, P. R., & Landi, E. 2021, ApJ, 909, 38
Del Zanna, G., & Ishikawa, Y. 2009, A&A, 508, 1517
den Herder, J. W., Brinkman, A. C., Kahn, S. M., et al. 2001, A&A, 365, L7
Doron, R., & Behar, E. 2002, ApJ, 574, 518
Erickson, G. W. 1977, JPCRD, 6, 831
Follath, R. 2001, NIMPA, 467, 418
Follath, R., & Balzer, A. 2010, in AIP Conf. Proc. 1234, SRI 2009, 10th Int. Conf. on Synchrotron Radiation Instrumentation, ed. R. Garrett et al. (Melville, NY: AIP), 657
Foster, A. R., Ji, L., Smith, R. K., & Brickhouse, N. S. 2012, ApJ, 756, 128
Gillaspy, J., Lin, T., Tedesco, L., et al. 2011, ApJ, 728, 132
Grell, G. J., Leutenegger, M. A., & Shah, C. 2021, ApJ, 917, 105
Grilo, F., Shah, C., Kühn, S., et al. 2021, ApJ, 913, 140
Gu, L., Raassen, A. J. J., Mao, J., et al. 2019, A&A, 627, A51
Gu, L., Shah, C., Mao, J., et al. 2020, A&A, 641, A93
Gu, L., Shah, C., Mao, J., et al. 2022, A&A, 664, A62
Gu, M., Holczer, T., Behar, E., & Kahn, S. M. 2006, ApJ, 641, 1227
Gu, M. F. 2003, ApJ, 582, 1241
Gu, M. F. 2005, ApJS, 156, 105
Gu, M. F. 2008, CaJPh, 86, 675
Heilmann, R. K., Bruccoleri, A. R., Burwitz, V., et al. 2022, ApJ, 934, 171
Hoesch, M., Seltmann, J., Trinter, F., et al. 2022, JPhCS, 2380, 012086
Ishibashi, K., Dewey, D., Huenemoerder, D. P., & Testa, P. 2006, ApJL, 644, L117
Jansen, F., Lumb, D., Altieri, B., et al. 2001, A&A, 365, L1
Kaastra, J. S. 2017, A&A, 605, A51
Kaastra, J. S., Mewe, R., & Nieuwenhuijzen, H. 1996, 11th Colloq. on UV and X-ray Spectroscopy of Astrophysical and Laboratory Plasmas, 411
King, S. A., Spieß, L. J., Micke, P., et al. 2022, Natur, 611, 43
Kozlov, M. G., Safronova, M. S., Crespo López-Urrutia, J. R., & Schmidt, P. O. 2018, RvMP, 90, 045005
Kraft, R., Markevitch, M., Kilbourne, C., et al. 2022, arXiv:2211.09827
Kramida, A., Ralchenko, Y., Reader, J. & NIST ASD Team 2022, NIST Atomic Spectra Database, v5.9 (Gaithersburg, MD: National Institute of Standards and Technology), https://physics.nist.gov/asd
Krempaský, J., Follath, R., Strocov, V. N., Schmitt, T., & Flechsig, U. 2011, Proc. SPIE, 8139, 813 90K

Kühn, S., Cheung, C., Oreshkina, N. S., et al. 2022, PhRvL, 129, 245001
Kühn, S., Shah, C., Crespo López-Urrutia, J. R., et al. 2020, PhRvL, 124, 225001
Leutenegger, M. A., Kühn, S., Micke, P., et al. 2020, PhRvL, 125, 243001
Liang, G. Y., & Badnell, N. R. 2010, A&A, 518, A64
Loch, S., Pindzola, M., Ballance, C., & Griffin, D. 2005, JPhB, 39, 85
Loch, S. D., Ballance, C. P., Li, Y., Fogle, M., & Fontes, C. J. 2015, ApJ, 801, L13
Loch, S. D., Pindzola, M. S., Ballance, C. P., & Griffin, D. C. 2006, JPhB, 39, 85
Mauche, C. W., Liedahl, D. A., & Fournier, K. B. 2001, ApJ, 560, 992
McKenzie, D., Landecker, P., Broussard, R., et al. 1980, ApJ, 241, 409
Micke, P., Kühn, S., Buchauer, L., et al. 2018, RScI, 89, 063109
Nicastro, F., Kaastra, J., Argiroffi, C., et al. 2021, ExA, 51, 1013
Oreshkina, N. S., Cavaletto, S. M., Keitel, C. H., & Harman, Z. 2014, PhRvL, 113, 143001
Oreshkina, N. S., Cavaletto, S. M., Keitel, C. H., & Harman, Z. 2016, JPhB, 49, 094003
Paerels, F. B. S., & Kahn, S. M. 2003, ARA&A, 41, 291
Pajot, F., Barret, D., Lam-Trong, T., et al. 2018, JLTP, 193, 901
Parkinson, J. 1973, A&A, 24, 215
Perry-Sassmannshausen, A., Buhr, T., Martins, M., et al. 2021, PhRvA, 104, 053107
Phillips, K. J. H., Fawcett, B. C., Kent, B. J., et al. 1982, ApJ, 256, 774
Phillips, K. J. H., Greer, C. J., Bhatia, A. K., & Keenan, F. P. 1996, ApJL, 469, L57
Pradhan, A., & Nahar, S. 2011, Atomic Astrophysics and Spectroscopy (Cambridge: Cambridge Univ. Press)
Rossnagel, K., Kipp, L., Skibowski, M., & Harm, S. 2001, NIMPA, 467-468, 1485
Saba, J. L. R., Schmelz, J. T., Bhatia, A. K., & Strong, K. T. 1999, ApJ, 510, 1064
Santana, J. A., Lepson, J. K., Träbert, E., & Beiersdorfer, P. 2015, PhRvA, 91, 012502
Schmelz, J. T., Saba, J. L. R., & Strong, K. T. 1992, ApJL, 398, L115
Schwartz, D. A., Vikhlinin, A., Tananbaum, H., et al. 2019, Proc. SPIE, 11118, 111180K
Shabaev, V. M., Tupitsyn, I. I., & Yerokhin, V. A. 2018, CoPhC, 223, 69
Shah, C., Crespo López-Urrutia, J. R., Gu, M. F., et al. 2019, ApJ, 881, 100
Smith, B. W., Mann, J. B., Cowan, R. D., & Raymond, J. C. 1985, ApJ, 298, 898
Smith, R. K., Bautz, M., Bregman, J., et al. 2022, Proc. SPIE, 12181, 1218121
Steinbrügge, R., Kühn, S., Nicastro, F., et al. 2022, ApJ, 941, 188
Stierhof, J., Kühn, S., Winter, M., et al. 2022, EPJD, 76, 38
Tashiro, M., Maejima, H., Toda, K., et al. 2018, Proc. SPIE, 10699, 1069922
Tiesinga, E., Mohr, P. J., Newell, D. B., & Taylor, B. N. 2021, RvMP, 93, 025010
Togawa, M., Kühn, S., Shah, C., et al. 2020, PhRvA, 102, 052831
Togawa, M., Kühn, S., & Shah, C. 2023, PhRvL, submitted
Tupitsyn, I. I., Kozlov, M. G., Safronova, M. S., Shabaev, V. M., & Dzuba, V. A. 2016, PhRvL, 117, 253001
Viefhaus, J., Scholz, F., Deinert, S., et al. 2013, NIMPA, 710, 151
Waljeski, K., Moses, D., Dere, K. P., et al. 1994, ApJ, 429, 909
Wang, K., Chen, Z. B., Si, R., et al. 2016, ApJS, 226, 14
Werner, N., Zhuravleva, I., Churazov, E., et al. 2009, MNRAS, 398, 23
Wu, C., & Gao, X. 2019, NatSR, 9, 7463
Xu, H., Kahn, S. M., Peterson, J. R., et al. 2002, ApJ, 579, 600
Yerokhin, V., & Surzhykov, A. 2019, JPCRD, 48, 033104
Yerokhin, V. A., & Shabaev, V. M. 2015, JPCRD, 44, 033103

2.3 Hanle-effect for lifetime measurements in the soft X-ray regime

A century-old technique for measuring atomic lifetimes has now been adapted to measure picosecond lifetimes in the X-ray regime. This article is accepted for publication at *Physical Review Letters*

AUTHORS **Moto Togawa**, Jan Richter, Chintan Shah, Marc Botz, Joshua Nenninger, Jonas Danisch, Joschka Goes, Steffen Kühn, Pedro Amaro, Awad Mohamed, Yuki Amano, Stefano Orlando, Roberta Totani, Monica de Simone, Stephan Fritzsche, Thomas Pfeifer, Marcello Coreno, Andrey Surzhykov, José R. Crespo López-Urrutia

PUBLICATION STATUS Accepted by *Physical Review Letters*

JOURNAL REFERENCE

DIGITAL OBJECT IDENTIFIER The preprint version is accessible at
https://doi.org/10.48550/arXiv.2408.12227

AUTHOR'S CONTRIBUTIONS **MT** and SK prepared and organized the experiment. **MT**, SK, MB, JN, JD, JG. JB, JS, MH took the data. RT, MS and MC operated the synchrotron radiation beamline. **MT** analyzed the data. **MT** and JRCLU wrote the manuscript except for the theoretical part. JR and AS performed theoretical simulation and wrote theoretical part. All authors took part in the critical review of the manuscript before and after submission.

ABSTRACT By exciting a series of $1s^2\,{}^1S_0 \rightarrow 1snp\,{}^1P_1$ transitions in helium-like nitrogen ions with linearly polarized monochromatic soft X-rays at the Elettra facility, we found a change in the angular distribution of the fluorescence sensitive to the principal quantum number n. In particular it is observed that the ratio of emission in directions parallel and perpendicular to the polarization of incident radiation increases with higher n. We find this n-dependence to be a manifestation of the Hanle effect, which served as a practical tool for lifetime determinations of optical transitions since its discovery in 1924. In contrast to traditional Hanle effect experiments, in which one varies the magnetic field and considers a particular excited state, we demonstrate a 'soft X-ray Hanle effect' which arises in a static magnetic field but for a series of excited states. By comparing experimental data with theoretical predictions, we were able to determine lifetimes ranging from hundreds of

femtoseconds to tens of picoseconds of the $1s{\it n}p\,^1P_1$ levels, which find excellent agreement with atomic-structure calculations. We argue that dedicated soft X-ray measurements could yield lifetime data that is beyond current experimental reach and cannot yet be predicted with sufficient accuracy.

Hanle Effect for Lifetime Determinations in the Soft X-Ray Regime

Moto Togawa,[1,2,3,*] Jan Richter,[4,5] Chintan Shah,[6,1,7] Marc Botz,[1,3] Joshua Nenninger,[1] Jonas Danisch,[1] Joschka Goes,[1] Steffen Kühn,[1] Pedro Amaro,[8] Awad Mohamed,[9,10] Yuki Amano,[11] Stefano Orlando,[9] Roberta Totani,[9,12] Monica de Simone,[13] Stephan Fritzsche,[14,15,16] Thomas Pfeifer,[1] Marcello Coreno,[9] Andrey Surzhykov,[4,17] and José R. Crespo López-Urrutia[1]

[1]*Max-Planck-Institut für Kernphysik, Saupfercheckweg 1, 69117 Heidelberg, Germany*
[2]*European XFEL, Holzkoppel 4, 22869 Schenefeld, Germany*
[3]*Heidelberg Graduate School for Physics, Ruprecht-Karls-Universität Heidelberg, Im Neuenheimer Feld 226, 69120 Heidelberg, Germany*
[4]*Physikalisch–Technische Bundesanstalt, D–38116 Braunschweig, Germany*
[5]*Institut für Theoretische Physik, Leibniz Universität Hannover, Appelstraße 2, 30167 Hannover, Germany*
[6]*NASA Goddard Space Flight Center, 8800 Greenbelt Road, Greenbelt, Maryland 20771, USA*
[7]*Department of Physics and Astronomy, Johns Hopkins University, Baltimore, Maryland 21218, USA*
[8]*Laboratory of Instrumentation, Biomedical Engineering and Radiation Physics (LIBPhys-UNL), Department of Physics, NOVA School of Science and Technology, NOVA University Lisbon, 2829-516 Caparica, Portugal*
[9]*ISM-CNR, Istituto di Struttura della Materia, LD2 Unit, 34149 Trieste, Italy*
[10]*Physics Division, School of Science and Technology, Università di Camerino, Via Madonna delle Carceri 9, Camerino, MC, Italy*
[11]*Institute of Space and Astronautical Science (ISAS), Japan Aerospace Exploration Agency (JAXA), 3-1-1 Yoshinodai, Chuo-ku, Sagamihara, Kanagawa 252-5210, Japan*
[12]*Elettra - Sincrotrone Trieste S.C.p.A., Strada Statale 14, 34149 Trieste, Italy*
[13]*IOM-CNR, Istituto Officina dei Materiali, 34149 Trieste, Italy*
[14]*Helmholtz-Institut Jena, Fröbelstieg 3, D-07763 Jena, Germany*
[15]*GSI Helmholtzzentrum für Schwerionenforschung GmbH, Planckstrasse 1, D-64291 Darmstadt, Germany*
[16]*Theoretisch-Physikalisches Institut, Friedrich-Schiller-Universität Jena, D-07763 Jena, Germany*
[17]*Institut für Mathematische Physik, Technische Universität Braunschweig, Mendelssohnstrasse 3, D-38106 Braunschweig, Germany*

(Received 13 June 2024; accepted 12 September 2024)

By exciting a series of $1s^2\,{}^1S_0 \rightarrow 1snp\,{}^1P_1$ transitions in heliumlike nitrogen ions with linearly polarized monochromatic soft x rays at the Elettra facility, we found a change in the angular distribution of the fluorescence sensitive to the principal quantum number n. In particular it is observed that the ratio of emission in directions parallel and perpendicular to the polarization of incident radiation increases with higher n. We find this n dependence to be a manifestation of the Hanle effect, which served as a practical tool for lifetime determinations of optical transitions since its discovery in 1924. In contrast to traditional Hanle effect experiments, in which one varies the magnetic field and considers a particular excited state, we demonstrate a "soft x-ray Hanle effect" which arises in a static magnetic field but for a series of excited states. By comparing experimental data with theoretical predictions, we were able to determine lifetimes ranging from hundreds of femtoseconds to tens of picoseconds of the $1snp\,{}^1P_1$ levels, which find excellent agreement with atomic-structure calculations. We argue that dedicated soft x-ray measurements could yield lifetime data that are beyond current experimental reach and cannot yet be predicted with sufficient accuracy.

DOI:

Diagnostics of high-temperature plasmas—whether generated in fusion devices, with high-power lasers from the infrared to the x-ray range, or found in astrophysical observations—relies on accurate experimental and theoretical data of oscillator strengths for x-ray transitions in highly charged ions (HCI). Generally, few-electron HCI are present in such plasmas. While, in principle, their simpler electronic structure should facilitate calculations and thus

*Contact author: togawa@mpi-hd.mpg.de

diagnostics, there are still large gaps in our experimental knowledge of those systems. Accurate line positions [1], oscillator strengths, and lifetimes [2] were measured for a variety of HCI by exciting them with monochromatized x rays within electron beam ion traps. Synchrotron radiation facilities provide polarized x rays to resonantly excite intershell-transitions in HCI, leading to fluorescence emission distributions that depend both on the incident polarization and the angular momenta of the upper and lower levels. For example, for the simplest case of a $J_i = 0 \rightarrow J_\nu = 1 \rightarrow J_f = 0$ electric dipole transition, the angular distribution of photons, scattered normal to the direction of the incident linearly polarized beam, exhibits the well-known pattern of classical dipole radiation [3]:

$$W(\phi) = W_0 \sin^2\phi. \tag{1}$$

This simple approach suggests, in particular, no photon emission parallel to the incident polarization vector, i.e., at $\phi = 0$. However, even a weak external magnetic field can affect this distribution, as discovered by Hanle in 1924 [4], who showed how it results from the interference of partially overlapping magnetic sublevels. From then on, the Hanle effect became a key tool for optical lifetime determinations, and is still in use. For HCI and also beyond the optical range, however, other experimental methods were necessary (for reviews, see, e.g., [5] on trapped ions, [6,7] on beam-foil methods, or [8,9] for historical overviews). A plethora of theoretical studies has covered lifetimes of allowed and forbidden transitions in many different isoelectronic sequences. Lifetimes of long-lived metastable states (e.g., $1s2s\,^3S_1$) of He-like ions have been repeatedly measured along the isoelectronic sequence with accuracy in some cases better than 1% [10–15]. However, fast transitions in heavier elements, e.g., such as those arising from the $^1P_1$ levels, have only been accessible either by beam-foil excitation [6] or high-resolution x-ray spectroscopy [16]. All the above techniques are successful in measuring lifetimes within a certain energy and time range. However, no experiment so far has been able to test (soft) x-ray transitions associated with lifetimes in the range from hundreds of femtoseconds to a few picoseconds. To fill this experimental gap, we performed a high-energy analog of the original Hanle experiment at the soft x-ray beamline, (GasPhase) of the Elettra synchrotron radiation facility in Trieste, Italy [17,18]. A portable electron beam ion trap (EBIT), PolarX-EBIT [19], was installed at the Gasphase beamline. This compact, room-temperature EBIT sources its magnetic field from stacks of neodymium magnets, achieving a maximum field strength of 0.85 T in the interaction zone. Its off-axis electron gun allows the photon beam to enter and leave the apparatus unimpeded along its longitudinal axis. For the production of the target ions, a tenuous molecular nitrogen beam is injected into the interaction zone of the EBIT, where highly charged

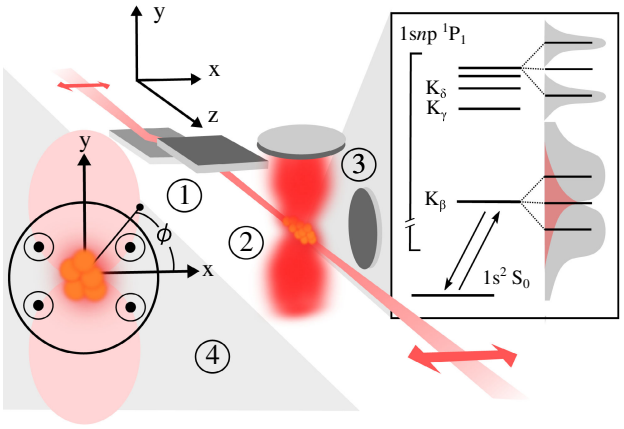

FIG. 1. Experimental setup. Linearly polarized undulator radiation is monochromatized (1) and focused on HCIs (2), which are generated and captured by the electron beam (not shown) that is tightly focused by a magnetic field. X rays following the resonant excitation are scattered by the ions and recorded by two SDDs (3), one perpendicular and the other parallel to the plane of polarization. Inset left (4): Representation of the angular distribution of the fluorescence photons in relation to the magnetic field (black circled dot) according to Eq. (1) with the emission angle ϕ. Inset right: Grotian diagram of the electronic levels investigated in this work and depiction of the corresponding magnetic sublevels m_j. At low n, the natural width of several of these states can overlap (red shaded area in inset), allowing for their coherent excitation. At higher n, the linewidth decreases, leading to statistical excitation process, i.e., depolarization.

nitrogen ions are produced by means of successive electron impact ionization. By tuning the electron beam energy to approximately 200 eV, a charge-state distribution dominated by heliumlike nitrogen ions is produced and trapped. This electron energy is lower than the excitation threshold for the K shell, reducing the background caused by electron impact excitation on our signal. The ions are illuminated by the focused, linearly polarized, monochromatic soft x-ray beam from the GasPhase beamline. The beamline is equipped with a monochromator with a variable-angle spherical grating with 1200 lines per mm reaching a resolution of up to 10 000 and an estimated flux of 10^{10} ph/s. X rays emitted from the ions are then registered by two silicon-drift detectors (SDD) which are mounted side-on and parallel and perpendicular to the polarization vector of the incident photon beam (see Fig. 1). The fluorescence yield recorded by these two SDDs gives insight into the angular distribution of the emitted fluorescence photons. Their energy resolution of approximately 60 eV FWHM at the oxygen K edge additionally allows the fluorescence photons to be distinguished from the background. As depicted in Fig. 2, fluorescence is recorded in discrete steps of the incident photon energy. The two detectors record simultaneously the fluorescence yield parallel ($Y_{||}$) and perpendicular ($Y_\perp$) to the polarization plane. After integration, we determine the ratio $Y_{||}/Y_\perp$.

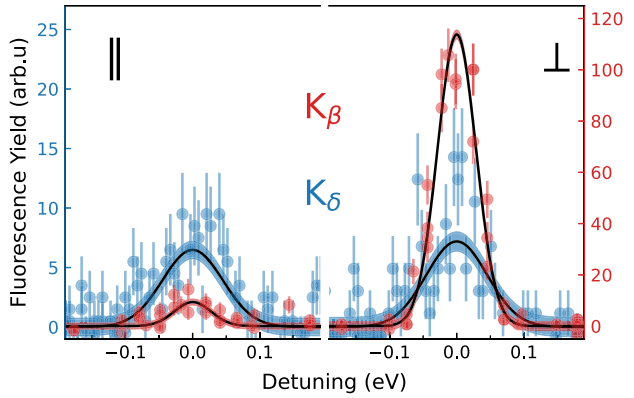

F2:1 FIG. 2. Exemplary measurement of two selected $1s - np$ lines.
F2:2 Left: Fluorescence yield recorded within the polarization plane.
F2:3 Right: Fluorescence yield perpendicular to the polarization plane.
F2:4 The ratio for K_β is still dominated by the perpendicular
F2:5 contribution in accordance to Eq. (1). K_δ shows close to equal
F2:6 emission in both directions.

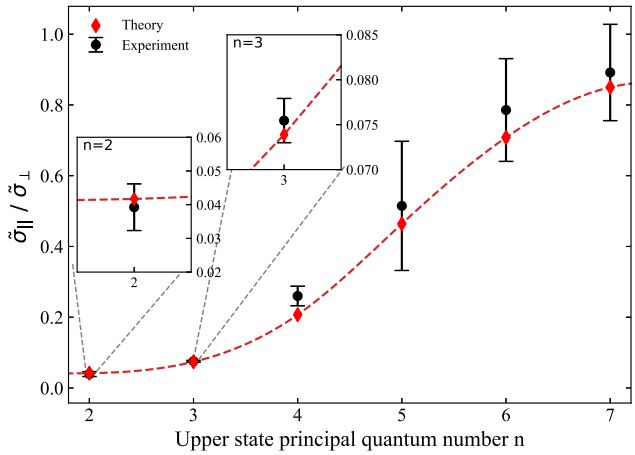

FIG. 3. Ratio of cross sections for the resonant scattering of F3:1
light parallel and perpendicular to the polarization vector of the F3:2
incident light against the principal quantum number n of the p F3:3
electron in the $^1P_1$ state. Red diamonds represent our theoretical F3:4
predictions, connected by a dotted red curve to guide the eye. Our F3:5
calculations of a ratio close to zero for $n = 2$ and increasing for F3:6
$n > 2$ agree well with the present experimental data. This data is F3:7
obtained as the ratio of the detected intensities $Y_\parallel / Y_\perp$ which is F3:8
equal to $\sigma_\parallel / \sigma_\perp$. F3:9

This is repeated for the $1s^2 - 1snp\,^1P_1$ series with n up to 7. According to Eq. (1), the fluorescence yield $Y_\parallel$ should always be equal to zero; finite values are a measure of depolarization. For transitions at higher n, we set the monochromator to the corresponding resonances after finding their positions with an initial scan. We then acquire signal for longer times and subtract the EBIT background obtained by closing the photon shutter of the beamline (see Supplemental Material [20]).

By plotting the yield ratios against the principal quantum number n of the upper level, we observe in qualitative agreement with the field-free approximation of Eq. (1) a ratio close to zero for $n = 2$ (Kα). However, for $n > 2$ its value grows rapidly and approaches already at $n = 7$ a value of $\approx$1, representing full depolarization (Fig. 3). In order to understand these results, we theoretically analyze the resonant elastic scattering of linearly polarized light by evaluating the corresponding second-order matrix element:

$$\mathcal{M}_{M_f,M_i} = \alpha \sum_{\gamma_\nu J_\nu M_\nu} \left[\frac{\langle f|\hat{\mathcal{R}}^\dagger(\boldsymbol{k}_f,\boldsymbol{\epsilon}_f)|\nu\rangle\langle\nu|\hat{\mathcal{R}}(\boldsymbol{k}_i,\boldsymbol{\epsilon}_i)|i\rangle}{E_i - E_\nu + \omega_i} + \frac{\langle f|\hat{\mathcal{R}}(\boldsymbol{k}_i,\boldsymbol{\epsilon}_i)|\nu\rangle\langle\nu|\hat{\mathcal{R}}^\dagger(\boldsymbol{k}_f,\boldsymbol{\epsilon}_f)|i\rangle}{E_i - E_\nu - \omega_i} \right], \quad (2)$$

with α being the fine structure constant and $|i\rangle = |\gamma_i J_i M_i\rangle$, $|\nu\rangle = |\gamma_\nu J_\nu M_\nu\rangle$, and $|f\rangle = |\gamma_f J_f M_f\rangle$ the short-hand notations for the initial, intermediate, and final electronic states. These states are specified by their total angular momentum J, its projection M, and γ, which refers to all additional quantum numbers needed for a unique characterization of the states. For elastic photon scattering, as considered in the present study, the electronic configurations and total angular momentum of initial and final states are the same, $\gamma_i = \gamma_f$ and $J_i = J_f$. The operators $\hat{\mathcal{R}}(\boldsymbol{k}_i,\boldsymbol{\epsilon}_i)$ and $\hat{\mathcal{R}}^\dagger(\boldsymbol{k}_f,\boldsymbol{\epsilon}_f)$ describe the absorption and emission of photons with wave vectors $\boldsymbol{k}_i$ and $\boldsymbol{k}_f$ and polarization vectors $\boldsymbol{\epsilon}_i$ and $\boldsymbol{\epsilon}_f$, respectively [21,22].

The evaluation of Eq. (2) requires a summation over the complete atomic spectrum $|\gamma_\nu J_\nu M_\nu\rangle$. This sum can be truncated to a single term when the energy of the incident photon is close to a transition between initial and one of the intermediate states $\omega_i \approx E_\nu - E_i$. In this resonant case, the scattering amplitude can be simplified to

$$\mathcal{M}^{\mathrm{res}}_{M_f,M_i} \approx \alpha \sum_{M_\nu} \frac{\langle f|\hat{\mathcal{R}}^\dagger(\boldsymbol{k}_f,\boldsymbol{\epsilon}_f)|\nu\rangle\langle\nu|\hat{\mathcal{R}}(\boldsymbol{k}_i,\boldsymbol{\epsilon}_i)|i\rangle}{E_i - E_\nu + \omega_i + i\Gamma_\nu/2}. \quad (3)$$

Here, the natural width Γ_ν of the intermediate state was phenomenologically introduced to the denominator to avoid a divergency for the case of a zero energy detuning, i.e., when $\omega_i = E_\nu - E_i$ [21–23]. Using the matrix element (3) one can obtain the differential cross section

$$\frac{\mathrm{d}\sigma}{\mathrm{d}\Omega}(\theta_f,\phi_f) = \frac{1}{2J_i+1} \sum_{M_i,M_f,\boldsymbol{\epsilon}_f} \left|\mathcal{M}^{\mathrm{res}}_{M_f,M_i}\right|^2, \quad (4)$$

for the resonant scattering of a photon under the angles (θ_f,ϕ_f) defined with respect to the direction $\boldsymbol{k}_i$ and polarization $\boldsymbol{\epsilon}_i$ of the incident radiation. Here, we assumed an unpolarized initial state of the ion and that both the population of the magnetic sublevels $|\gamma_f J_f M_f\rangle$ as well as the polarization of the scattered light remain unobserved.

In what follows, we apply Eqs. (3) and (4) to analyze the angular distribution of the $1s^2\,^1S_0 \to 1snp\,^1P_1 \to 1s^2\,^1S_0$

scattering of initially linearly polarized photons. By considering the experimental setup from Fig. 1, with scattered photons detected normal to the propagation direction of the incident radiation ($\theta_f = \pi/2$) and either within ($\phi_f = 0$) or perpendicular ($\phi_f = \pi/2$) to its polarization axis, we find

$$\sigma_{\parallel} \equiv \frac{\mathrm{d}\sigma}{\mathrm{d}\Omega}\left(\theta_f = \frac{\pi}{2}, \phi_f = 0\right) = 0, \tag{5a}$$

$$\sigma_{\perp} \equiv \frac{\mathrm{d}\sigma}{\mathrm{d}\Omega}\left(\theta_f = \frac{\pi}{2}, \phi_f = \frac{\pi}{2}\right) = \frac{4R^2}{\Gamma_\nu^2 + 4\Delta\omega^2}. \tag{5b}$$

Here, $R = 2\pi\alpha|\langle 1snp\,^1P_1||\hat{a}_{E1}||1s^2\,^1S_0\rangle|^2$ is the square of the reduced matrix element of the electric dipole transition $1s^2\,^1S_0 \to 1snp^1P_1$ and $\Delta\omega = E_\nu - E_i - \omega$ is the detuning between the incident photon energy and the transition energy. As seen from Eqs. (5a) and (5b), the standard second-order perturbation approach negates photon scattering parallel to the polarization vector of the incident light, $\sigma_{\parallel} = 0$, and hence, predicts a vanishing ratio $\sigma_{\parallel}/\sigma_{\perp}$, in contradiction with our experimental findings.

So far, our theoretical analysis was restricted to the case of resonant scattering in the absence of external electromagnetic fields. However, in our experiment the ions are perturbed by the magnetic field of the EBIT. This field is aligned with the propagation direction of the incident light, chosen as the z axis, and leads to a Zeeman splitting of the electronic levels. In a similar manner as in Ref. [24], the Zeeman effect can be incorporated into the perturbative approach, leading to a modified scattering amplitude:

$$\mathcal{M}^{\mathrm{res}}_{M_f,M_i} \approx \alpha \sum_{M_\nu} \frac{\langle f|\hat{\mathcal{R}}^\dagger(\boldsymbol{k}_f, \boldsymbol{\epsilon}_f)|\nu\rangle\langle\nu|\hat{\mathcal{R}}(\boldsymbol{k}_i, \boldsymbol{\epsilon}_i)|i\rangle}{E_i - (E_\nu + M_\nu \Delta E_Z) + \omega_i + i\Gamma_\nu/2}, \tag{6}$$

with $\Delta E_Z = g_j \mu_B B$ and the unperturbed energy of the intermediate state E_ν. One may note that Eq. (6) is obtained under the assumption that the initial (and, hence, final) state does not exhibit any Zeeman splitting since $J_i = J_f = 0$.

By applying Eqs. (4) and (6) for the $1s^2\,^1S_0 \to 1snp^1P_1 \to 1s^2\,^1S_0$ scattering, we derive the cross sections

$$\sigma_{\parallel} = 16\kappa\Delta E_Z^2, \tag{7a}$$

$$\sigma_{\perp} = 4\kappa(\Gamma_\nu^2 + 4\Delta\omega^2), \tag{7b}$$

for photons scattered parallel and perpendicular to the polarization $\boldsymbol{\epsilon}_i$ of the incident light, with the parameter $\kappa = R^2/\left[\Gamma_\nu^2 + 4(\Delta\omega - E_z)^2\right]\left[\Gamma_\nu^2 + 4(\Delta\omega + E_z)^2\right]$. With the help of Eq. (7), we obtain the ratio

$$\frac{\sigma_{\parallel}}{\sigma_{\perp}} = \frac{4\Delta E_Z^2}{\Gamma_\nu^2 + 4\Delta\omega^2}, \tag{8}$$

which can deviate from zero for an ion in an external magnetic field. The effect depends on experimental parameters and ion properties, and will be discussed later. We just mention here that Eq. (8) corresponds to the low-intensity limit of the nonperturbative treatment of the Hanle effect (see Ref. [25] for further details).

Expression (8) was derived for ideally monochromatic and completely polarized incident radiation as well as for pointlike detectors, and has to be modified for realistic conditions. Since the width of the incident radiation $\Delta\omega \approx 0.1$ eV is larger than the Zeeman splitting of the intermediate sublevels, we use an energy-averaged cross section:

$$\tilde{\sigma}_{\perp,\parallel} = \int \sigma_{\perp,\parallel}(\omega)\mathcal{G}(\omega)\mathrm{d}\omega. \tag{9}$$

Here, $\mathcal{G}(\omega)$ is a Gaussian distribution, and the incident synchrotron radiation is assumed to be incoherent. We also take into account the detector size by integrating the differential cross section (4) over a finite solid angle. Finally, the effect of incomplete polarization of the incident radiation is considered within the density-matrix approach. Details are given in the Supplemental Material [20].

We now apply the perturbative approach discussed above to analyze our experimental findings. We start from Eq. (8) which predicts that the ratio $\sigma_{\parallel}/\sigma_{\perp}$ might deviate from zero due to a Zeeman splitting of the intermediate state, and can be used to explain the pronounced n dependence. Since the g factor, and hence the Zeeman shift, are almost constant for the entire series $1snp^1P_1$ [26], this strong dependence must arise from the lifetime τ and, hence, the natural width $\Gamma_\nu = \hbar/\tau$ of the excited states. Indeed, as seen from Table I, τ is very sensitive to the principal quantum number n. For example, the lifetime of the $1s7p^1P_1$ state is increased by a factor of 40 compared to $\tau(1s2p^1P_1)$. These results were obtained with the configuration-interaction method implemented in the AMBiT code [27], and agree well with previous calculations from Refs. [28,29].

The remarkable prolongation of the lifetime as a function of n, and the concomitant reduction of the natural width $\Gamma_\nu = \hbar/\tau$ leads to the growth of the ratio $\sigma_{\parallel}/\sigma_{\perp}$, as we observe in the experiment. For a quantitative comparison with experimental data we make use of the energy-averaged cross section (9) and take into account corrections due to the finite size of the photon detectors. Moreover, we assume complete linear polarization of the incident synchrotron radiation (see Refs. [19,30,31]) and take into account the EBIT magnetic field of $B = 0.85$ T. For these parameters, we calculate the modified cross section ratio $\tilde{\sigma}_{\parallel}/\tilde{\sigma}_{\perp}$ shown by the red diamonds in Fig. 3. The good agreement of theory and experiment supports our explanation of the effect based on the Zeeman splitting of ionic levels. The clear n dependence of the ratio $\sigma_{\parallel}/\sigma_{\perp}$ manifests the well-known Hanle effect, now found in the soft x-ray domain.

One may note, that our setup for the observation of the Hanle effect differs from the traditional one. Indeed for the

TABLE I. The excitation energies, defined with respect to the ground $1s^2\,{}^1S_0$ state, and lifetimes of the $1snp\,{}^1P_1$ levels of a N^{5+} ion. Theoretical predictions obtained using the AMBiT code are compared with previous calculations from Refs. [28,29], and with present experimental findings for the lifetimes.

	Theory		Experiment
n	Energy (eV)	Lifetime (ps)	Lifetime (ps)
2	430.73	0.5539	(0.58 ± 0.58)
	430.71 [28]	0.5537 [28]	
	430.55 [29]	0.5531 [29]	
3	497.95	1.844	(1.98 ± 0.17)
	497.93 [28]	1.846 [28]	
	497.75 [29]	1.844 [29]	
4	521.60	4.346	(5.3 ± 0.7)
	521.58 [28]	4.346 [28]	
	521.39 [29]	4.337 [29]	
5	532.56	8.445	(9.78 ± 4.46)
	532.56 [28]	8.449 [28]	
	532.35 [29]	8.423 [29]	
6	538.53	14.51	(19.89 ± 11.85)
	538.50 [28]	14.44 [28]	
	538.31 [29]	14.51 [29]	
7	542.13	22.79	(35.29 ± 44.79)

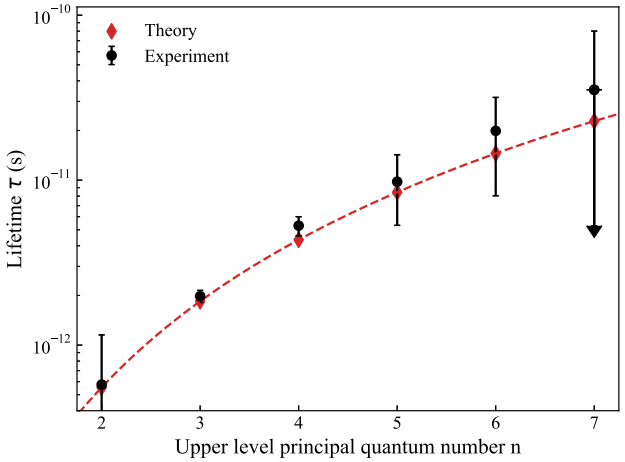

FIG. 4. Lifetime $\tau = \hbar/\Gamma_\nu$ of the $1snp\,{}^1P_1$ states depending on the principal quantum number n. Our experimental data (black dots) is compared with theoretical predictions obtained using the AMBiT code (red diamonds), connected by a dotted red curve to guide the eye.

latter, one varies the external magnetic field to change the overlap of magnetic sublevels of a specific intermediate state $|\gamma_\nu J_\nu\rangle$. This, in turn, alters the interference contributions of the substates $|\gamma_\nu J_\nu M_\nu\rangle$ to the scattering cross section and, hence, leads to a modification of polarization and angular distribution of outgoing photons. In contrast, the external magnetic field remains constant in our experiment. The variation of the overlap of the Zeeman sublevels and, hence, of their inteference contributions is achieved by addressing various $1snp\,{}^1P_1$ states exhibiting different natural widths Γ_ν. This results in analogous modifications to the angular distribution, effectively demonstrating the Hanle effect through the n dependence in our setup.

With these insights, we can extract information about the lifetimes of the intermediate $1snp\,{}^1P_1$ states from the measured ratio $\sigma_\parallel/\sigma_\perp$. To achieve this, we fit our theoretical predictions of the modified cross section ratio $\tilde{\sigma}_\parallel/\tilde{\sigma}_\perp$ to the experimental data from Fig. 3. The only free parameter for the fitting procedure is Γ_ν, while all other experimental parameters are taken as in the calculations above. The uncertainty of the derived lifetimes $\tau(1snp\,{}^1P_1)$, being about few tens of percent, is estimated by propagating those of the measured cross-section ratios and the magnetic field strength (see Supplemental Material [20]). The derived results, displayed in Fig. 4, show good agreement with the theoretical predictions.

In conclusion, our present method based on the Hanle effect yields lifetimes of excited levels from abundant species of highly charged ions in the soft x-ray regime. This method is feasible for a range of hundreds of femtoseconds to tens of picoseconds for which resolution of linewidths is still beyond reach at advanced light sources. Our present experimental accuracy will improve with more statistics in future campaigns. Following this demonstration with theoretically well-understood He-like ions, we will apply our method to the Li-like and other isoelectronic sequences, in which transitions, broadened by more complex fast autoionization channels, still challenge theory. Experimental results for such transitions are urgently needed for an improved scientific harvest of x-ray space observatory data from Chandra, XMM-Newton, and the recently launched XRISM [32]. Furthermore, applications for magnetic field and polarization studies in hot plasmas are expected [33,34].

Acknowledgments—Financial support was provided by the Max-Planck-Gesellschaft (MPG), Bundesministerium für Bildung und Forschung (BMBF) through project 05K13SJ2 and by the AHEAD-2020 Project Grant Agreement No. 871158 of the European Union's Horizon 2020 Programme. C.S. acknowledges support from MPG and NASA-JHU Cooperative Agreement and Max-Planck-Gesellschaft (MPG). P. A. acknowledges support from Fundaçáo para a Ciência e Tecnologia, Portugal, under Grant No. UID/FIS/04559/2020 (LIBPhys) and High Performance Computing Chair—a R&D infrastructure based at the University of Évora (PI: M. Avillez).We acknowledge Elettra Sincrotrone Trieste for providing access to its synchrotron radiation facilities (long term proposals No. 20205206). Fabio Zuccaro is acknowledged for technical support during beamtime preparation and realization. J. R. and A. S. acknowledge funding by the Deutsche Forschungsgemeinschaft (DFG, German Research Foundation) under Germany's Excellence Strategy—EXC-2123 QuantumFrontiers—390837967.

[1] M. A. Leutenegger *et al.*, High-precision determination of oxygen K_α transition energy excludes incongruent motion of interstellar oxygen, Phys. Rev. Lett. **125**, 243001 (2020).

[2] Steffen Kühn *et al.*, New measurement resolves key astrophysical Fe XVII oscillator strength problem, Phys. Rev. Lett. **129**, 245001 (2022).

[3] Vsevolod V. Balashov, Alexei N. Grum-Grzhimailo, and Nikolai M. Kabachnik, *Polarization and Correlation Phenomena in Atomic Collisions: A Practical Theory Course* (Springer Science & Business Media, New York, 2000).

[4] Wilhelm Hanle, Über magnetische Beeinflussung der Polarisation der Resonanzfluoreszenz, Z. Phys. **30**, 93 (1924).

[5] E Träbert, Atomic lifetime measurements employing an electron beam ion trap, Can. J. Phys. **86**, 73 (2008).

[6] E. Träbert, P. H. Heckmann, R. Hutton, and I. Martinson, Intercombination lines in delayed beam-foil spectra, J. Opt. Soc. Am. B **5**, 2173 (1988).

[7] Elmar Träbert, Measurement of femtosecond atomic lifetimes using ion traps, Appl. Phys. B **114**, 167 (2014).

[8] Elmar Träbert, Atomic lifetime data and databases, Atoms **10**, 46 (2022).

[9] Elmar Träbert, On atomic lifetimes and environmental density, Atoms **10**, 114 (2022).

[10] H. T. Schmidt, P. Forck, M. Grieser, D. Habs, J. Kenntner, G. Miersch, R. Repnow, U. Schramm, T. Schüssler, D. Schwalm, and A. Wolf, High-precision measurement of the magnetic-dipole decay rate of metastable heliumlike carbon ions in a storage ring, Phys. Rev. Lett. **72**, 1616 (1994).

[11] G. S. Stefanelli, P. Beiersdorfer, V. Decaux, and K. Widmann, Measurement of the radiative lifetime of the $1s2s^3S_1$ level in heliumlike magnesium, Phys. Rev. A **52**, 3651 (1995).

[12] P. Beiersdorfer, L. Schweikhard, J. Crespo López-Urrutia, and K. Widmann, The magnetic trapping mode of an electron beam ion trap: New opportunities for highly charged ion research, Rev. Sci. Instrum. **67**, 3818 (1996).

[13] J. R. Crespo López-Urrutia, P. Beiersdorfer, D. W. Savin, and K. Widmann, Precision measurement of the lifetime of the $1s2s^3S_1$ metastable level in heliumlike O^{6+}, Phys. Rev. A **58**, 238 (1998).

[14] E. Träbert, P. Beiersdorfer, G. V. Brown, A. J. Smith, S. B. Utter, M. F. Gu, and D. W. Savin, Improved electron-beam ion-trap lifetime measurement of the $Ne^{8+}1s2s^3S_1$ level, Phys. Rev. A **60**, 2034 (1999).

[15] J. R. Crespo López-Urrutia, P. Beiersdorfer, and K. Widmann, Lifetime of the $1s2s^3S_1$ metastable level in He-like S^{14+} measured with an electron beam ion trap, Phys. Rev. A **74**, 012507 (2006).

[16] P. Beiersdorfer, A. L. Osterheld, V. Decaux, and K. Widmann, Observation of lifetime-limited x-ray linewidths in cold highly charged ions, Phys. Rev. Lett. **77**, 5353 (1996).

[17] K. C. Prince, R. R. Blyth, R. Delaunay, M. Zitnik, J. Krempasky, J. Slezak, R. Camilloni, L. Avaldi, M. Coreno, Gly Stefani *et al.*, The gas-phase photoemission beamline at Elettra, J. Synchrotron Radiat. **5**, 565 (1998).

[18] R. R. Blyth, R. Delaunay, M. Zitnik, J. Krempasky, R. Krempaska, J. Slezak, K. C. Prince, R. Richter, M. Vondracek, R. Camilloni, L. Avaldi, M. Coreno, G. Stefani, C. Furlani, M. de Simone, S. Stranges, and M.-Y. Adam, The high resolution gas phase photoemission beamline, elettra, J. Electron Spectrosc. Relat. Phenom. **101–103**, 959 (1999).

[19] P. Micke, S. Kühn, L. Buchauer, J. R. Harries, T. M. Bücking, K. Blaum, A. Cieluch, A. Egl, D. Hollain, S. Kraemer, T. Pfeifer, P. O. Schmidt, R. X. Schüssler, Ch. Schweiger, T. Stöhlker, S. Sturm, R. N. Wolf, S. Bernitt, and J. R. Crespo López-Urrutia, The Heidelberg compact electron beam ion traps, Rev. Sci. Instrum. **89**, 063109 (2018).

[20] See Supplemental Material at http://link.aps.org/supplemental/10.1103/PhysRevLett.000.000000 for technical details on experimental and theoretical analysis.

[21] V. G. Serbo, A. Surzhykov, and A. Volotka, Resonant scattering of plane-wave and twisted photons at the gamma factory, Ann. Phys. (Berlin) **534**, 2100199 (2022).

[22] A. Volotka, D. Samoilenko, S. Fritzsche, V. G. Serbo, and A. Surzhykov, Polarization of photons scattered by ultra-relativistic ion beams, Ann. Phys. (Berlin) **534**, 2100252 (2022).

[23] D. Samoilenko, A. V. Volotka, and S. Fritzsche, Elastic photon scattering on hydrogenic atoms near resonances, Atoms **8**, 12 (2020).

[24] J. O. Stenflo, Hanle-Zeeman scattering matrix, Astron. Astrophys. **338**, 301 (1998).

[25] P. Avan and C. Cohen-Tannoudji, Hanle effect for monochromatic excitation. Non perturbative calculation for a $J = 0$ to $J = 1$ transition, J. Phys. Lett. **36**, 85 (1975).

[26] M. Puchalski and U. D. Jentschura, Quantum electrodynamic corrections to the g factor of helium P states, Phys. Rev. A **86**, 022508 (2012).

[27] E. V. Kahl and J. C. Berengut, AMBIT: A programme for high-precision relativistic atomic structure calculations, Comput. Phys. Commun. **238**, 232 (2019).

[28] W. R. Johnson, I. M. Savukov, U. I. Safronova, and A. Dalgarno, E1 transitions between states with $n = 1$–6 in helium-like carbon, nitrogen, oxygen, neon, silicon, and argon, Astrophys. J. Suppl. Ser. **141**, 543 (2002).

[29] Natalie Mary Cann and Ajit J. Thakkar, Oscillator strengths for S-P and P-D transitions in heliumlike ions, Phys. Rev. A **46**, 5397 (1992).

[30] B. Rouvellou, S. Rioual, L. Avaldi, R. Camilloni, G. Stefani, and G. Turri, Angle-dependent postcollisional interaction and interference effects in resonant double photoionization of neon, Phys. Rev. A **67**, 012706 (2003).

[31] J. Karvonen, A. Kivimäki, H. Aksela, S. Aksela, R. Camilloni, L. Avaldi, M. Coreno, M. de Simone, and K. C. Prince, Angular distribution in xenon $M_{4,5}N_{4,5}N_{4,5}$ Auger decay, Phys. Rev. A **59**, 315 (1999).

[32] M. Tashiro, H. Maejima, K. Toda, R. Kelley, L. Reichenthal, J. Lobell, R. Petre, M. Guainazzi, E. Costantini, M. Edison *et al.*, Concept of the x-ray astronomy recovery mission, Proc. SPIE Int. Soc. Opt. Eng. **10699**, 1069922 (2018).

[33] Silvano Fineschi, Richard B. Hoover, Muamer Zukic, Jongmin Kim, Arthur B. C. Walker II, and Phillip C. Baker, Polarimetry of HI Lyman-alpha for coronal magnetic

field diagnostics, in *Multilayer and Grazing Incidence X-Ray/EUV Optics for Astronomy and Projection Lithography*, edited by Richard B. Hoover and Arthur B. C. Walker II (International Society for Optics and Photonics, SPIE, 1993), Vol. 1742, pp. 423–438.

[34] S. Sahal-Bréchot, M. Malinovsky, and V. Bommier, The polarization of the O VI 1032 A line as a probe for measuring the coronal vector magnetic field via the Hanle effect, Astron. Astrophys. **168**, 284 (1986).

Hanle effect for lifetime determinations in the soft X-ray regime: Supplemental Material

I. DETAILS ON EXPERIMENTAL DATA ANALYSIS

To achieve accurate fluorescence-yield ratios, we carried out two types of measurements. Initially, photon energy scans were conducted to determine the nominal transition energy. The sufficiently high count rates of low-n transitions enabled these energy scans to effectively determine the fluorescence yield ratio $Y_\parallel/Y_\perp$ (see Fig.2 in main text and Fig. S2 a).). For high-n transitions with low transition rates, we conducted additional measurements using a constant photon energy set to the nominal transition energy. After a designated acquisition period, a fast shutter was closed to stop the ion cloud's illumination. This was followed by a period dedicated to capturing the background level, see Fig. S2 d). After obtaining an one-dimensional spectrum by projection to the photon energy axis (Fig. S2 b) and e)), the fluorescence-yield ratio is determined through a least-squares fit. For energy scans, a simple Gaussian model with constant baseline is used, while for static energy measurements, a step function is applied. The fluorescence yield is then associated with the amplitude of the Gaussian or the height of the step function. For each level (n=2 to n=7), multiple measurements were taken and consolidated into a single value for each observed transition using a weighted average.

In addition to the fluorescence yield, we also obtain experimental transition energies from the photon energy scans. Our nominal transition energies generally shift by approximately ∼100 meV to lower energies compared to theoretical predictions (see the measured spectrum of the K$_\beta$transition in Fig. S2 c)). Such shifts are commonly observed and are primarily due to imperfect calibration of the photon energy, which is typically performed using less accurate atomic or molecular transitions.

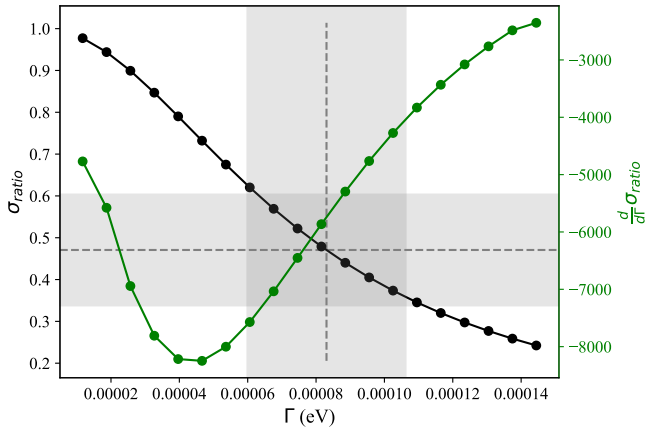

FIG. S1. Each black datapoint depicts the frequency-averaged cross section ratio evaluated at given lifetime Γ_ν for $1s5p\,^1P_1$ level. The horizontal dotted line and shaded area correspond to the experimentally measured cross section ratio. The vertical dotted line indicates its intersection with the calculated cross section ratio. The corresponding uncertainty, which is given by the vertical shaded area, is obtained from the derivative of σ_{ratio} (green data points).

A. Extraction of lifetime

As mentioned in the main text, we first start with the ratio of the frequency-averaged cross sections

$$\tilde{\sigma}_{\perp,\parallel} = \int \sigma_{\perp,\parallel}(\omega)\,\mathcal{G}(\omega)\,\mathrm{d}\omega. \tag{S1}$$

Now, to determine the lifetime of the excited $1snp\,^1P_1$ levels from the experiment, we insert a magnetic field density of $B = 0.85\,\mathrm{T}$ and polarization of $P_l = 1.0$ into Eq. (S1). With only Γ_ν as a free parameter, we equate the frequency-averaged cross section ratio to the respective experimental ratio

$$\sigma_\perp^{exp}/\sigma_\parallel^{exp} = \tilde{\sigma}_\perp/\tilde{\sigma}_\parallel(\Gamma_\nu). \tag{S2}$$

Thereby, we find experimentally, the lifetime Γ_ν, associated to the respective cross section ratio or transition. The error on the experimental cross section ratio is translated by multiplication of the derivative of the cross section ratio evaluated at Γ_ν, see Fig. S1.

B. Effect of magnetic field uncertainty

To quantify the contribution of the magnetic field uncertainty to the determined lifetime, we repeat the extraction of lifetimes as given in Section I A with a field of $B = 0.9\,\mathrm{T}$. The value results from the measured value $B = 0.85\,\mathrm{T}$ by Micke *et al.* [1] in addition to a conservatively estimated magnetic field uncertainty of 0.05 T. Again, we determine Γ_ν and use the difference of both as additional systematic uncertainty. For illustrative purposes, we show in Fig. S3 the influence of the magnetic field on the predicted cross section ratio. The impact of the magnetic field uncertainty is minimal for low- and high-n 1snp states but can reach ∼ 5% for medium n. This can be explained by the fact that for the low-n states the level widths Γ_ν are so large that a variation of B does not affect the cross section ratio. For the high-n states, in contrast, the widths Γ_ν are so small that the variation of B does not lead to a substantial change in the overlap of the almost separated Zeeman sublevels.

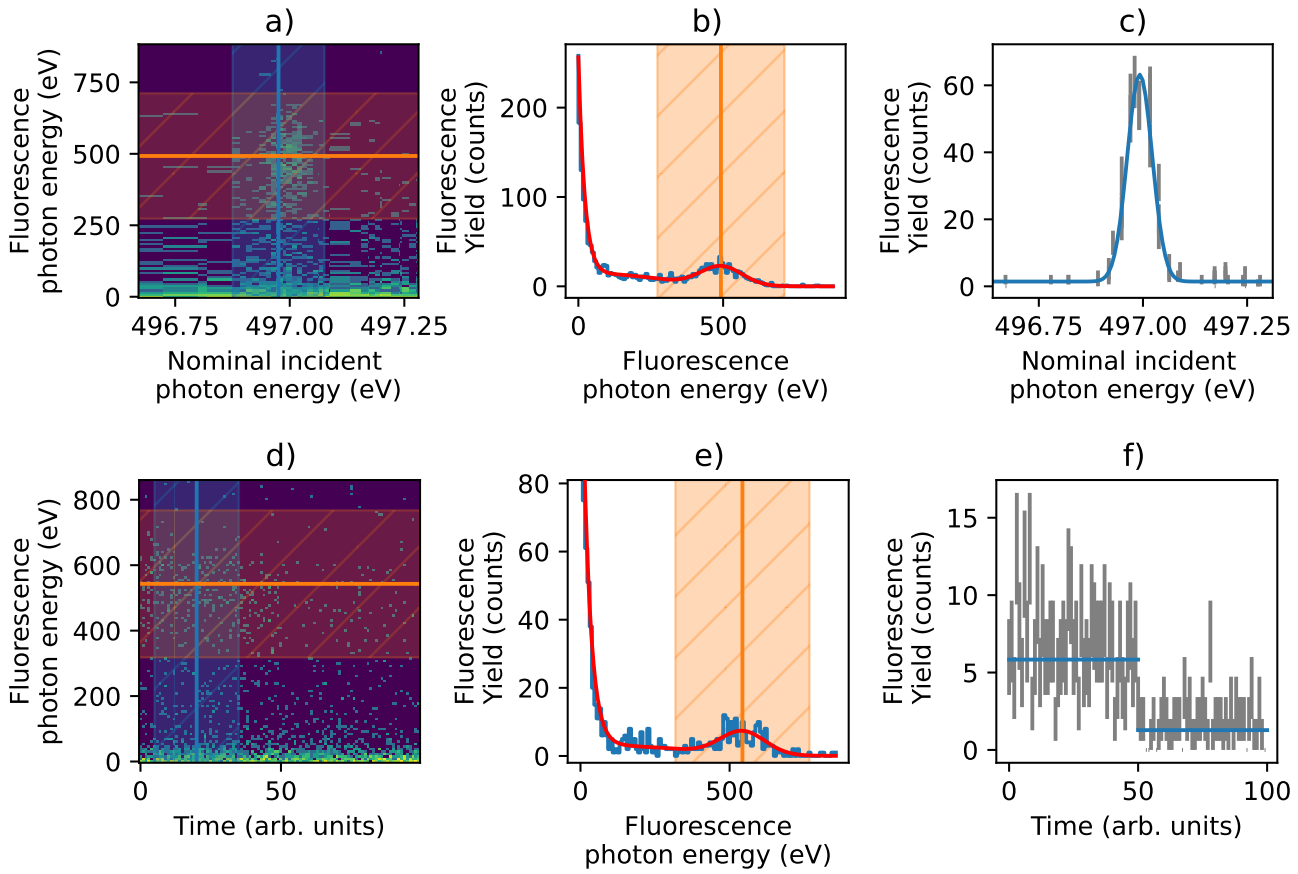

FIG. S2. Extraction of fluorescence spectra for photon energy scans (a, b, c) and constant energy measurements (d, e, f). First, an appropriate region of interest (blue shaded area) is projected onto the fluorescence photon energy axis. The resulting fluorescence spectrum is then modeled, enabling the extraction of a four-sigma region of interest (orange shaded area). Subfigures c) and f) are obtained by projecting this four-sigma region onto the incident photon energy axis and the time axis, respectively.

II. DETAILS ON THEORETICAL ANALYSIS

As described in the main text the modified cross sections $\tilde{\sigma}_{\parallel,\perp}$ are obtained by averaging $\sigma_{\parallel,\perp}$ over a Gaussian frequency distribution. However the expression for the cross sections $\sigma_{\parallel,\perp}$ might also be affected by an incomplete polarization of the incident radiation as well as by a finite detector size. In what follows, we present modified expressions for $\sigma_{\parallel,\perp}$ taking into account both of these effects.

A. Effect of incomplete linear polarization

Applying the density matrix approach from Ref. [2], cross sections can be obtained for any arbitrary polarization. With P_l denoting the degree of linear polarization and the parameter $\kappa = R^2/\left[\Gamma_\nu^2 + 4\left(\Delta\omega - E_z\right)^2\right]\left[\Gamma_\nu^2 + 4\left(\Delta\omega + E_z\right)^2\right]$, the cross sections for photons scattered in directions parallel and perpendicular to the polarization vector are given by

$$\sigma_\parallel = \kappa\left[8E_z^2(P_l+1) - 2(P_l-1)\left(\Gamma_\nu^2 + 4\Delta\omega^2\right)\right] \quad \text{(S3a)}$$

$$\sigma_\perp = \kappa\left[2(P_l+1)\left(\Gamma_\nu^2 + 4\Delta\omega^2\right) - 8E_z^2(P_l-1)\right] \quad \text{(S3b)}$$

and their ratio takes the form

$$\frac{\sigma_\parallel}{\sigma_\perp} = -\frac{4E_z^2(P_l+1) - (P_l-1)\left(\Gamma_\nu^2 + 4\Delta\omega^2\right)}{4E_z^2(P_l-1) - (P_l+1)\left(\Gamma_\nu^2 + 4\Delta\omega^2\right)}. \quad \text{(S4)}$$

As expected, for perfectly linearly polarized light ($P_l = 1$) Eq. (S4) reproduces Eq. (8) from the main text while for unpolarized light ($P_l = 0$) Eq. (S4) simplifies to $\sigma_\parallel/\sigma_\perp = 1$. To investigate the effect of incomplete polarization of the incident radiation, we used Eq. (S3) to calculate the ratio $\tilde{\sigma}_\parallel/\tilde{\sigma}_\perp$ for the $1s^2\,{}^1S_0 \rightarrow 1snp\,{}^1P_1 \rightarrow 1s^2\,{}^1S_0$ scattering. Calculations have been performed for complete polarization as well as for $P_l = 0.975$, 0.95 and 0.925. These values are in a conservative range of possible variation of the polarization of synchrotron light. As seen from Fig. S3, the effect of incomplete polarization is largest for $n = 2$ and decreases

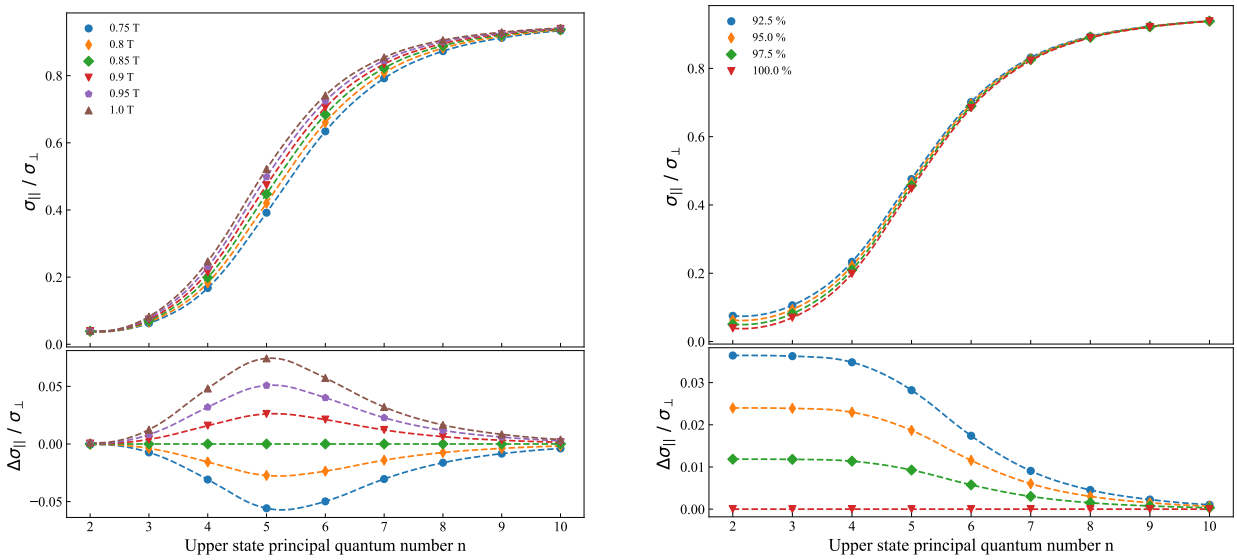

FIG. S3. Left: Predicted cross section ratios for varying magnetic fields. At high and low n, we see weak sensitivity to the external fields. Right: Predicted cross section ratio for varying degrees of linear polarization. Highest sensitivity to the polarization is predicted at low principal quantum numbers. The two bottom panes depict the difference of cross section ratio with respect to the chosen model parameter (B=0.85 T and P=100 %)

for higher excited states. However, since the degree of linear polarization is expected to be higher than 99% [3], polarization impurity has a negligible effect on $\sigma_{\parallel}/\sigma_{\perp}$ compared to the statistical uncertainty and, hence, is not considered here.

B. Effect of finite detector size

Having discussed the effect of incomplete polarization we also take into account the effect of a finite detector size by integrating the differential cross section (4) from the main text over a finite solid angle:

$$\sigma_{\parallel} = \int_{\phi=-\delta_{\parallel}}^{\phi=+\delta_{\parallel}} \int_{\theta=\frac{\pi}{2}-\delta_{\parallel}}^{\theta=\frac{\pi}{2}+\delta_{\parallel}} \frac{\mathrm{d}\sigma}{\mathrm{d}\Omega}(\theta,\phi)\sin(\theta)\,\mathrm{d}\theta\mathrm{d}\phi, \tag{S5}$$

$$\sigma_{\perp} = \int_{\phi=\frac{\pi}{2}-\delta_{\perp}}^{\phi=\frac{\pi}{2}+\delta_{\perp}} \int_{\theta=\frac{\pi}{2}-\delta_{\perp}}^{\theta=\frac{\pi}{2}+\delta_{\perp}} \frac{\mathrm{d}\sigma}{\mathrm{d}\Omega}(\theta,\phi)\sin(\theta)\,\mathrm{d}\theta\mathrm{d}\phi. \tag{S6}$$

Here, the opening angle $\delta_{\parallel,\perp}$ reflects the size of the photon detector. Evaluating this integral, we obtain the cross sections for photons observed with a finite size detector parallel and perpendicular to the incident light polarization $\boldsymbol{\epsilon}_i$:

$$\sigma_{\parallel,\perp} = \frac{\kappa}{3}\sin(\delta_{\parallel,\perp})\left[\left(28\delta_{\parallel,\perp} - 4\delta_{\parallel,\perp}\cos(2\delta_{\parallel,\perp})\right)A \pm P_l(10\sin(2\delta_{\parallel,\perp}) + \sin(4\delta_{\parallel,\perp}))B\right].$$

where we introduced for the sake of brevity the parameters $A = \left(4E_Z^2 + \Gamma^2 + 4\Delta\omega^2\right)$ and $B = \left(4E_Z^2 - \Gamma^2 - 4\Delta\omega^2\right)$. In the expression above, the term proportional to P_l has a positive sign for $\sigma_{\parallel}$ and a negative sign for $\sigma_{\perp}$. While the finite detector size effect is the dominant contribution to $\tilde{\sigma}_{\parallel}/\tilde{\sigma}_{\perp}$ for $n = 2$, the contribution becomes smaller than 1% for $n \geq 6$. Taking into account the finite detector size, our results are in very good agreement with the experimental findings (see Fig. (3) in the main text).

[1] P. Micke, S. Kühn, L. Buchauer, J. R. Harries, T. M. Bücking, K. Blaum, A. Cieluch, A. Egl, D. Hollain, S. Kraemer, T. Pfeifer, P. O. Schmidt, R. X. Schüssler, C. Schweiger, T. Stöhlker, S. Sturm, R. N. Wolf, S. Bernitt, and J. R. Crespo López-Urrutia, The Heidelberg compact electron beam ion traps, Review of Scientific Instruments **89**, 063109 (2018), https://pubs.aip.org/aip/rsi/article-pdf/doi/10.1063/1.5026961/19761397/063109_1_online.pdf.
[2] A. Volotka, D. Samoilenko, S. Fritzsche, V. G. Serbo, and A. Surzhykov, Polarization of photons scattered by ultra-relativistic ion beams, Ann. Phys.(Berlin) **534** (2022).
[3] J. Karvonen, A. Kivimäki, H. Aksela, S. Aksela, R. Camilloni, L. Avaldi, M. Coreno, M. de Simone, and K. C.

141 Prince, Angular distribution in xenon $M_{4,5}N_{4,5}N_{4,5}$ auger
142 decay, Phys. Rev. A **59**, 315 (1999).

Chapter 3

XFEL studies on trapped highly charged ions

In this Chapter, results from two measurement campaigns at the Small Quantum System instrument at the European XFEL facility (EuXFEL) are presented, dedicated to exploit the unique FEL properties for HCI experiments beyond established laser spectroscopy (see Chapter 1.1.2) [16, 49]. XFELs are linear electron accelerator based synchrotron radiation sources [50, 51]. Their light, the XFEL radiation, provides properties that are distinct from synchrotron radiation from storage ring facilities, which have been used in the work presented in Chapter 2. XFEL radiation is spatially almost completely coherent. The unique property of XFEL radiation is enabled by their undulators of more than hundred meter in length. At these scales, an effect known as self amplified spontaneous emission (SASE) emerges. Starting from spontaneously emitted photons, electrons become affected by the light field, making them faster or slower depending on their respective phase. This effect continues until all electrons within the bunch are rearranged to form clearly separated microbunches in the field of the XFEL radiation. These microbunched electrons emit photons collectively, resulting in exceptionally short pulse duration and pulse energy many orders higher than what contemporary synchrotrons can offer. (see. Fig. 3.1)

In Chapter 3.1, I present the use of the exceptionally high photon intensities available at EuXFEL to study non-linear processes with X-rays and HCIs deep in the saturation regime. Following that, I report on the use of short (fs) pulses for time-resolved measurements of fast decays in resonantly excited HCIs in Chapter 3.2. This lifetime measurement technique on HCIs has been pioneered within the framework of this thesis.

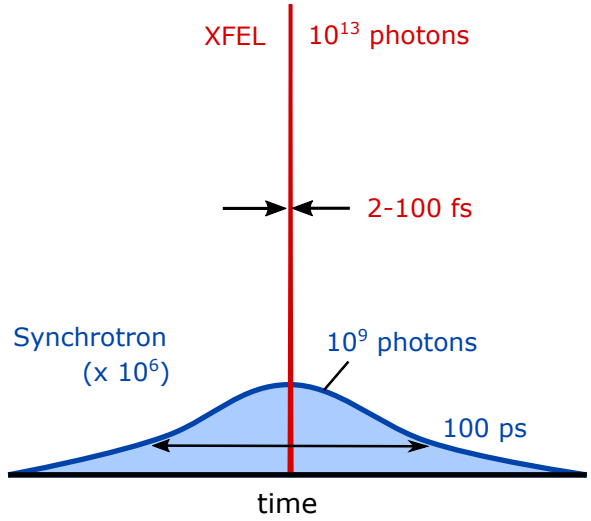

Figure 3.1. *Schematic comparison between a typical X-ray pulse from a Synchrotron and XFEL. Pulses coming from an XFEL contain four orders of magnitude more photons squeezed in a pulse, which is three or four orders of magnitude shorter in time. This opens up completely new opportunities for the study of fast dynamics in matter. Figure adapted from Ref. [52].*

3.1 Nonlinear multiphoton ionization of highly charged krypton

Spectroscopic investigations of prominent, allowed transitions in HCIs can facilitate useful diagnostics in hot laboratory as well as extraterrestrial plasma [53].
In this experiment we investigate the prominent L-to-M-shell single-electron transitions in neon-like ions, coined 3C and 3D [54]:

$$3C : \left[2p^6\right]_{J=0} \rightarrow \left(\left[2p^5\right]_{1/2} 3d_{3/2}\right)_{J=1} \tag{3.1}$$

$$3D : \left[2p^6\right]_{J=0} \rightarrow \left(\left[2p^5\right]_{3/2} 3d_{5/2}\right)_{J=1} . \tag{3.2}$$

The transition ratios of the 3C and 3D lines in neon-like iron have long been a subject of debate, as experimental measurements, astrophysical observations, and theoretical predictions have shown significant discrepancies. One experimental measurement, conducted at the Linac Coherent Light Source (LCLS) in Stanford [49], yielded an unexpectedly low line ratio. It was later discovered that the experiment was affected by population transfer between different charge states due to the high intensities produced by LCLS [55].
In this work, we have studied similar processes for neon-like krypton. Predictions for the 3C and 3D transitions in neon-like krypton estimate lifetimes of approximately 10 fs for both, leading to spectral lines of similar strength when observed under non-saturation conditions (see Fig. 3.3). We have observed that their line ratio undergoes a drastic transformation when the saturation regime is approached. In the following, we briefly present the experimental setup and the detection scheme. A qualitative explanation for the intensity ratio in the saturation regime is provided, which we confirm with a simple model to describe the underlying XFEL- HCI interaction of this experiment.

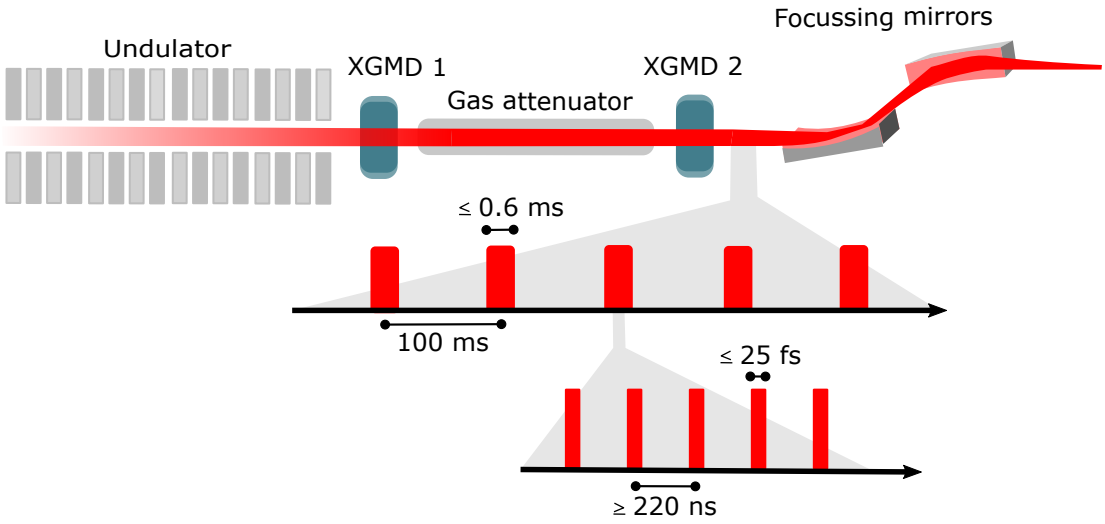

Figure 3.2. *Simplified schematic representation of the SASE3 beamline at EuXFEL. XFEL radiation generated by the 105 meter long undulator first passes through XGMD1 for intensity measurements before reaching the gas attenuator. Following an additional intensity measurement by XGMD2, two KB mirrors focus the XFEL radiation into the experimental chamber (see Fig. 3.4). The zoom-ins show the pulse pattern of the EuXFEL.*

Experimental setup

A compact electron beam ion trap (from now on referred as SQS-EBIT), similar in design as in reference [57], equipped with an off-axis electron gun has been installed into the soft X-ray beamline, Small Quantum Systems (SQS), at the SASE3 undulator of the European X-ray Free-Electron Laser facility.

The necessity of this experiment for a clean ToF-spectrum with well separated ion signatures, lead to the decision of utilizing monoisotopic krypton, ^{83}Kr. Going through a two-

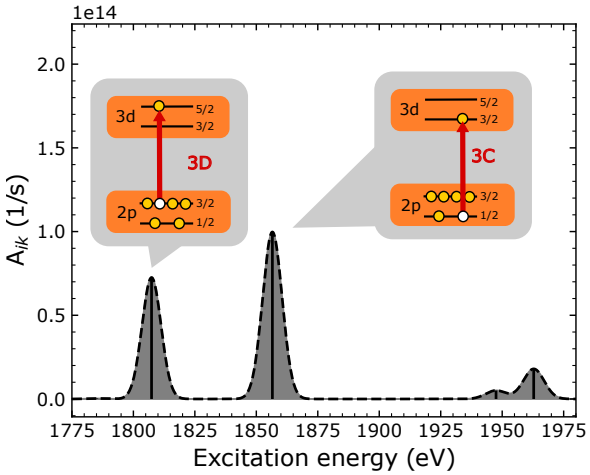

Figure 3.3. *Predicted 3C and 3D transitions in neon-like krypton at approximately 1850 and 1800 eV (black vertical lines). Both transitions are associated with a transition probability of roughly 10^{14} 1/s. Theory predictions are convoluted with a Gaussian of 0.5 % FWHM (dashed line). Calculation are performed with the Flexible Atomic Code [56].*

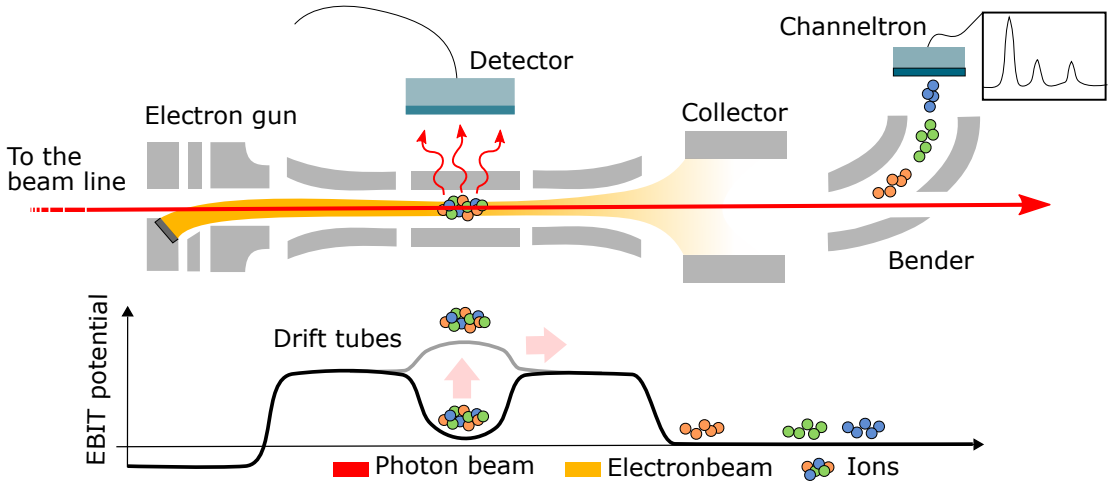

Figure 3.4. *Schematic representation of the experimental chamber, SQS-EBIT. Highly charged ions (HCIs) produced and trapped within SQS-EBIT are irradiated by the focused XFEL radiation. A silicon drift detector records the emitted fluorescence, while an ion-ToF spectrometer set up downstream of the EBIT records the charge state distribution (CSD). The bottom panel illustrates a simplified potential landscape of the EBIT and the ion extraction mechanism.*

stage differentially pumped vacuum system, neutral ^{83}Kr is injected to SQS-EBIT. With the electron beam of SQS-EBIT set to approximately 1780 eV and a current of 6 mA, a distribution of highly charged krypton ions with maximum abundance of aluminum-like krypton is produced. The distribution drops towards higher and lower charge states, leaving only little neon-like and silicon-like krypton within the trap. No charge states above neon-like krypton are observed as the electron beam energy has been set below the ionization threshold of neon-like krypton. An exemplary ToF-spectrum can be seen in Fig. 3.5.
The MHz-pulse-train of European XFEL (Fig. 3.2) is introduced to SQS-EBIT through its off-axis electron gun and illuminates the ion cloud, before leaving the instrument (Fig. 3.4). The ultrashort pulses, with estimated pulse duration of about 30 fs, are focused onto the ion cloud by means of Kirkpatrick-Baez (KB) optics. The interaction of the X-ray pulse with the trapped ion cloud is monitored by a silicon drift detector (SDD) directed towards the trapped ions in a plane perpendicular to the linear polarization of the incoming XFEL radiation. As the main detector for this experiment, an ion time-of-flight spectrometer (ion-ToF) records the charge-state distribution after the ion cloud has interacted with one entire XFEL train (see Fig. 3.5).

Data acquisition

We investigate the photon energy and intensity dependence of the charge-state distribution of the trapped HCIs. In particular, we focus our attention on the effect induced by resonant

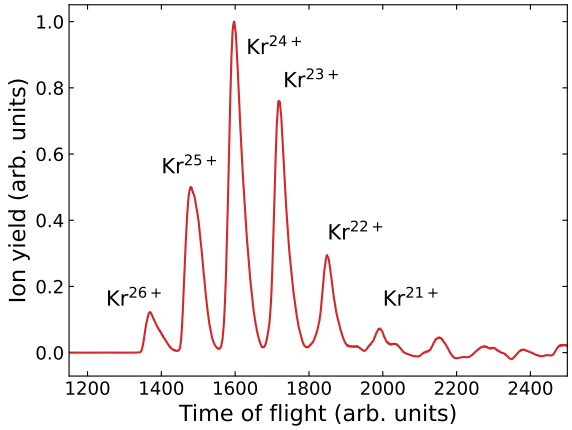

Figure 3.5. *An exemplary time-of-flight spectrum extracted from SQS-EBIT under injection of krypton. Ions are extracted from the trap at a rate of 1 Hz. Charge states from Kr^{26+} (neon-like Kr) to Kr^{21+} (silicon-like Kr) are clearly separated in time and detected.*

excitations. For that purpose, we scan the photon energy of the XFEL by means of the variable-gap undulator available at the Small Quantum Systems (SQS) over the two 3C and 3D resonances. We observe that additional charge states, fluorine- as well as oxygen-like krypton ions are resonantly produced. These additional charge states cannot be produced by means of single photon absorption. For that reason, we have investigated their dependence on the intensity in order to study the observed nonlinear ionization channels. The photon beamline allows monitoring and manipulation of the pulse intensity using a set of two X-ray Gas Monitor (XGM) systems and a gas attenuator permanently installed upstream of the SQS beamline [58, 59]. The gas attenuator consists of a long chamber filled with noble gas. While passing through the chamber, the XFEL beam looses intensity due to photoionization processes with the surrounding atoms. The pulse intensity before and after the attenuator is tracked by the XGM detectors (see Fig. 3.2). The photo ions produced within the EBIT are recorded by means of the ion-ToF spectrometer of SQS-EBIT, allowing to resolve the fluorine and oxygen-like krypton ion yields as a function of the photon energy and intensity as shown in the Fig. 3.6. The spectra displayed in the figure correspond to varying beam intensities, ranging from 100 % to 2 % (top to bottom) with approximately 3 mJ pulse energy for the unattenuated beam. In the following section, possible ionization mechanisms, which can explain the observed spectrum are discussed.

Resonance enhanced multiphoton ionization vs. resonant double-core-hole ionization in closed shell ions

When the energy of a single photon is insufficient to lift a bound electron into the continuum, ionization can still occur through multiphoton processes. Through simultaneous absorption of multiple photons by means of a virtual level, enough energy can be provided for ionization. These processes are called *non-sequential*. In the framework of interaction with short and intense XFEL pulses, the most common process is the *sequential* absorption of photons [45]. Consecutive, independent absorption processes occur over the duration of

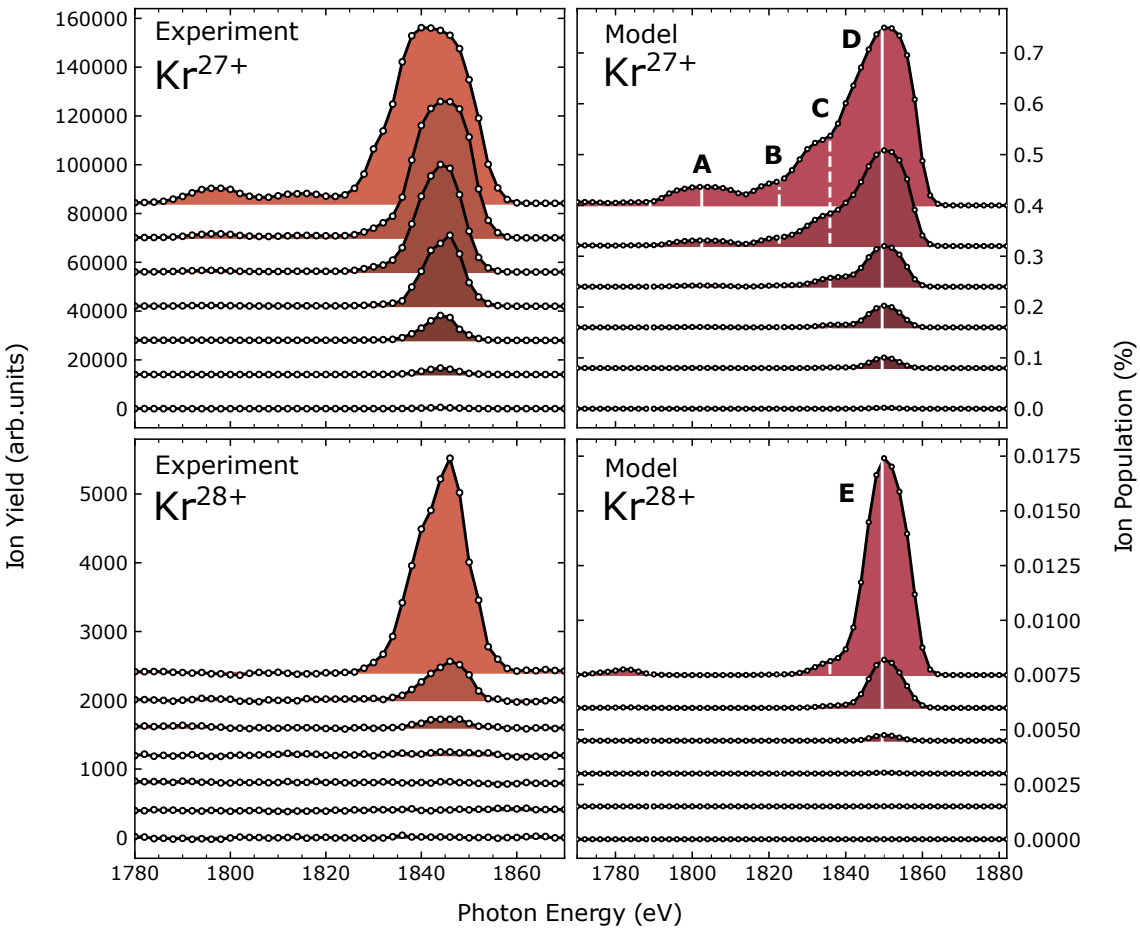

Figure 3.6. *As a function of XFEL photon energy, experimental (left) and predicted (right) ion yield spectra (Top: fluorine-like, Bottom: oxygen-like) are shown. To track the nonlinear dependence, ion yield spectra are recorded for decreasing intensity, which are depicted as waterfall diagrams from top to bottom. White vertical lines in the predicted spectra, mark transitions that initiate the respective features in the fluorine-like and oxygen-like ion spectrum.*

one pulse. A well known sequential process is the resonance enhanced multiphoton ionization (REMPI). In the simplest case, REMPI can occur by means of a resonant photon absorption, lifting an electron into an excited state, which is followed by a non-resonant photoionization process within the lifetime of the excited state (or pulse duration, whatever is shorter). More complex REMPI is reported in the XUV FEL experiments involving up to three XUV photons [60]. For REMPI in the (soft) X-ray regime core-electrons are targeted making Auger-Meitner and shake-Off competitive ionization processes. Ionization trajectories through multiple charge states have also been observed at XFEL experiments. Thereby, the sequential direct one-photon ionization limit can be significantly surpassed [47].
The production of double-core holes (i.e. multiply excited states with two K-shell or M-shell vacancies) is another possible process occurring during irradiation with short and intense X-

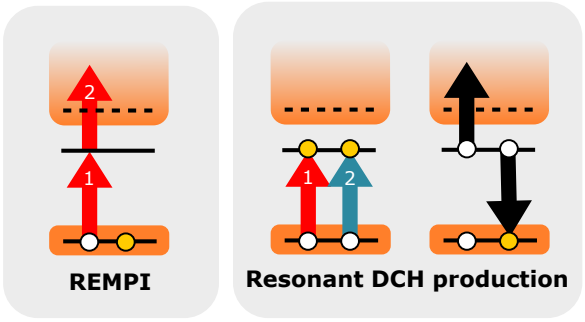

Figure 3.7. *Schematic representation of the resonance enhanced multiphoton ionization, REMPI (left) and the resonant ionization by means of double-core hole production (right).*

ray pulses. Such DCH states decay via autoionization typically within few femtoseconds due to the energetically more favorable ground state of the next higher charge state. The production of DCH has been extensively studied in atomic and molecular systems [61, 62] due their prospect of enabling enhanced control over molecular dynamics. In these studies, production of DCH states typically involves at least one non-resonant process. Still, fully resonant ionization by means of consecutive resonant excitation processes can be conceptualized. After the first photon resonantly excites an electron and produces a single-core hole (SCH) in an inner shell, all remaining electrons experience an increased Coulomb potential, effectively raising the energy required for subsequent electronic transitions. Consequently, to generate a second core hole through another resonant excitation, one would expect the second photon to need higher energy than the first.

We have performed atomic structure calculations using the Flexible Atomic Code [56] to find the positions of the resonances as well as their following DCH transitions along the isoelectronic sequence of neon-like ions from iron to yttrium. We have predicted the line positions and strengths of the respective 3C and 3D transitions (Fig. 3.8, black lines) and of the DCH producing transitions (Fig. 3.8, red and blue lines). The red lines depict all possible DCH transitions, the blue depict DCH transitions, which can be initiated from the upper level of 3C or 3D. As expected, for neon-like ions of low to medium atomic number the relevant DCH transitions are approximately 20 to 50 eV apart from the 3C line (See Fig. 3.8). But for increasing atomic number a significant fraction of the DCH transitions move towards the 3C transition and intersect it in the spectra of neon-like krypton, rubidium and strontium.

This tells us that entirely resonant DCH production is enabled at the energy of 3C within the bandwidth of a single color, which leads to an enhanced ionization probability. REMPI, however, due to its non-resonant property in its second part, is possible for both resonances 3C and 3D. This quantitative explanation seem to agree well with our experimental observation (Fig. 3.6).

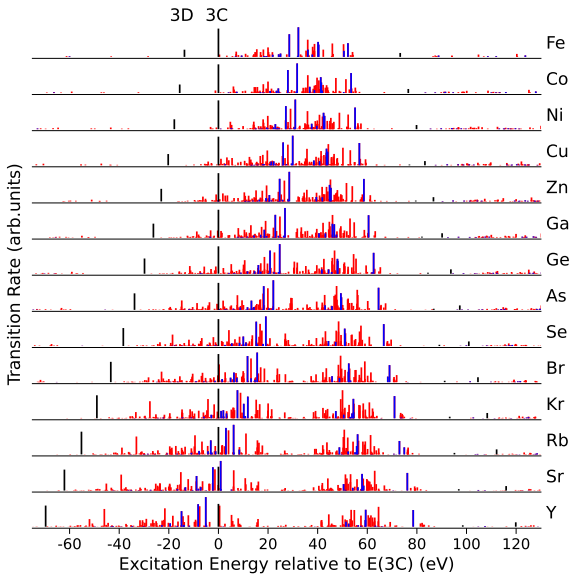

Figure 3.8. *Predicted spectra of neon-like ions from iron to yttrium. The prominent 3C and 3D transitions are depicted in black. Spectra are shifted to coincide energetically for 3C. DCH transitions are shown in red and blue. Red: All possible DCH transitions. Blue: DCH transitions with upper state of 3C or 3D as initial state. While significantly apart for iron, the DCH transitions gradually move into the 3C line for heavier elements crossing 3C at neon-like krypton.*

Spectral analysis

To provide a quantitative interpretation and to understand all the minute features, which we see in Fig. 3.6, we have developed a rate model to simulate the XFEL-HCI interaction. The presented model is in fact very similar to existing simulation tools as XMDYN and XATOM [63]. In terms of sophistication levels, it is inferior in all ways but one. The X-ray induced cross sections and transition probabilities are treated by XATOM in an approximate (nonrelativistic) manner. In this particular regard, there are other tools that can treat the processes, which are important for our experiment, in a more rigorous way. The Flexible Atomic Code (FAC) is a fully *ab initio* atomic structure calculation software, which we will utilize to produce all the necessary atomic data for the relevant interactions. This is possible because EBIT contains only highly charged ions, for which FAC is particularly effective and known to be precise.

With FAC, we take into account absorption (B_{ij}), stimulated emission (B_{ji}), radiative decay (A_{ji}), photoionization (σ_{ij}) as well as Auger-Meitner decays (A_{ji}^{AI}) in between levels, which we can categorize to ground states (GS), single core hole states (SCH) and double core hole states (DCH), for each charge state, respectively. Slow processes such as interactions involving the electron beam of SQS-EBIT are neglected. Non-sequential processes are not included. With all the necessary processes calculated, we solve the set of coupled rate equations

$$\frac{d}{dt}P_i(t) = \sum_{j\neq i}^{\text{all levels}} \left[\Gamma_{j\to i}P_j(t) - \Gamma_{i\to j}P_i(t)\right] \tag{3.3}$$

to simulate the time evolution of populations P. The rate $\Gamma_{i\to j}$ corresponds to the transition probability between levels i and j. In order to relate the the photoioniztion crosssection and Einstein B coefficients to the radiative and Auger-Meitner decays, which are photonenergy

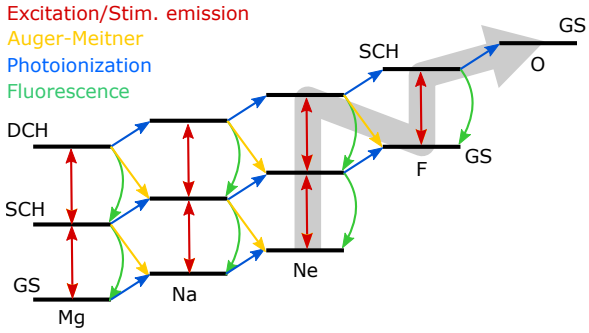

Figure 3.9. *Simplified level diagram of the highly charged krypton ions studied here, including their dominant electronic processes. The grey arrow depicts an exemplary ionization pathway for the production of oxygen-like krypton starting from the 3C SCH transition at approximately 1850 eV.*

and intensity dependent, we use the following estimated parameters: σ (focus, FWHM) = 2 μm, τ (pulse duration) = 30 fs, E_{max} (max. pulse energy) = 5 mJ. For the photon energy bandwidth, we find a value of 0.5% of the photon energy to be the most suitable. We further assume the spectral energy distribution to be Gaussian, neglecting any spectral properties arising from the SASE process. Additionally, we approximate the temporal profile as a square pulse with a duration of τ. We compare the model to experimental results by varying in the pulse energy as depicted in Fig. 3.6. and find that the simulated spectrum finds good agreement with the experiment. We identify four spectroscopic features A to D, labeled as in Fig. 3.6

The dominant ionization channels producing the features A and D in the photoion spectrum of fluorine-like krypton can be readily identified as:

$$A: \ \mathrm{Ne(GS)} \xrightarrow{\gamma} \mathrm{Ne(SCH)} \xrightarrow{\gamma} \mathrm{F(GS)} \tag{3.4}$$

and D:

$$D: \ \mathrm{Ne(GS)} \xrightarrow{\gamma} \mathrm{Ne(SCH)} \xrightarrow{\gamma} \mathrm{Ne(DCH)} \xrightarrow{\mathrm{AI}} \mathrm{F(GS)} \tag{3.5}$$

Both are two-photon processes, however D is associated with a significantly higher cross section, which becomes apparent due to its fully-resonant property. Spectral feature B is initiated by a SCH transition from the ground state of Kr^{24+} (Mg-like Kr):

$$B: \ \mathrm{Mg(GS)} \xrightarrow{\gamma} \mathrm{Mg(SCH)} \xrightarrow{\gamma} \mathrm{Mg(DCH)} \tag{3.6}$$

$$\xrightarrow{\mathrm{AI}} \mathrm{Na(GS)} \xrightarrow{\gamma} \mathrm{Na(SCH)} \xrightarrow{\gamma} \mathrm{Na(DCH)} \tag{3.7}$$

$$\xrightarrow{\mathrm{AI}} \mathrm{Ne(GS)} \xrightarrow{\gamma} \mathrm{Ne(SCH)} \xrightarrow{\gamma} \mathrm{F(GS)} \tag{3.8}$$

Spectral feature C is initiated by a SCH transition from the ground state of Kr^{24+} (Na-like Kr):

$$C: \ \mathrm{Na(GS)} \xrightarrow{\gamma} \mathrm{Na(SCH)} \xrightarrow{\gamma} \mathrm{Na(DCH)} \tag{3.9}$$

$$\xrightarrow{\mathrm{AI}} \mathrm{Ne(GS)} \xrightarrow{\gamma} \mathrm{Ne(SCH)} \xrightarrow{\gamma} \mathrm{F(GS)} \tag{3.10}$$

Spectral feature E is identified as a continuation of D with:

$$E: \ [\mathrm{D}] \xrightarrow{\gamma} \mathrm{F(SCH)} \xrightarrow{\gamma} \mathrm{O(GS)}, \tag{3.11}$$

which makes feature E with its entire process from Ne(GS) to O(GS) effectively a sequential four photon process, feature B and C a sequential six and 4 photon process, respectively. However, this model takes into account the interaction of the CSD with a single XFEL pulse. As our measurement scheme allowed only for Ion-ToF measurements after the arrival of an entire train of XFEL pulses (i.e. train-resolved), this model does not fully represent the recorded data, since the possibility of ions interacting repeatedly with photons from different pulses within the train is excluded. However, the good qualitative agreement of data and model confirms that the production of fluorine-like and oxygen-like krypton does occur mainly within one pulse. Accumulative effects can therefore be neglected.

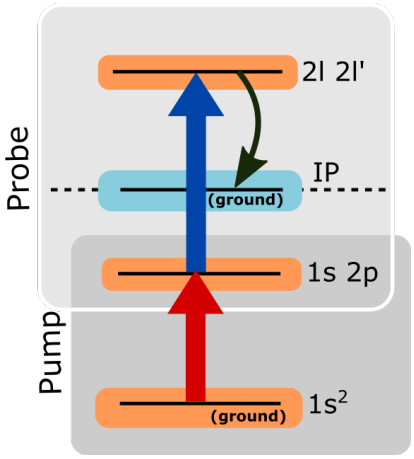

Figure 3.10. *Simplified level diagram of the here studied helium-like ions. The arrows depict an exemplary ionization pathway for the production of hydrogen-like ions starting from the SCH transition from the ground state.*

3.2 All X-ray pump probe spectroscopy in highly charged ions

Here, we present a measurement of the lifetime of the $1s2p\,^1P_1$ state in helium-like neon and fluorine. Their predicted lifetime of approximately 110 fs and 170 fs both corresponds to a linewidth of less than 10 meV. As discussed in Chapter 1.2.1, resolving such narrow features is plagued by many complications. By exploiting the few-femtosecond short X-ray pulses and the newly accessible two-color mode at the Small Quantum System Instrument of the European XFEL[64], a lifetime measurement in the time domain with an unprecedented precision for this range is enabled.
Our technique follows the well-known principle of pump-probe schemes (see Chapter 1.2.4). The first color, which will be the "pump", initiates the dynamics by resonant excitation of helium-like ions into the 1s2p $^1P_1$ state from their ground state. These collectively excited ions decay exponentially back to the ground state with a time constant given by the lifetime τ. This decay curve can be sampled by means of repeated measurements with a second "probe" X-ray pulse set at time interval t_{delay} with respect to the pump pulse.

Experimental set up

The experimental set up is identical to the previous one (see 3.1). The only difference is in the use of the novel two-color operation mode at EuropeanXFEL. In this operation mode two independent XFEL pulses are produced in the long SASE3 undulator. The wavelength and intensity of the pulses can be tuned independently. A variable delay of the two pulses can be introduced by means of a magnetic chicane set up within the undulator. We operate the EBIT under constant influx of a gas containing the target element (Ne, CF_4 for fluorine), with an electron beam energy of 900 eV, well under the production threshold of hydrogen-like neon (fluorine).

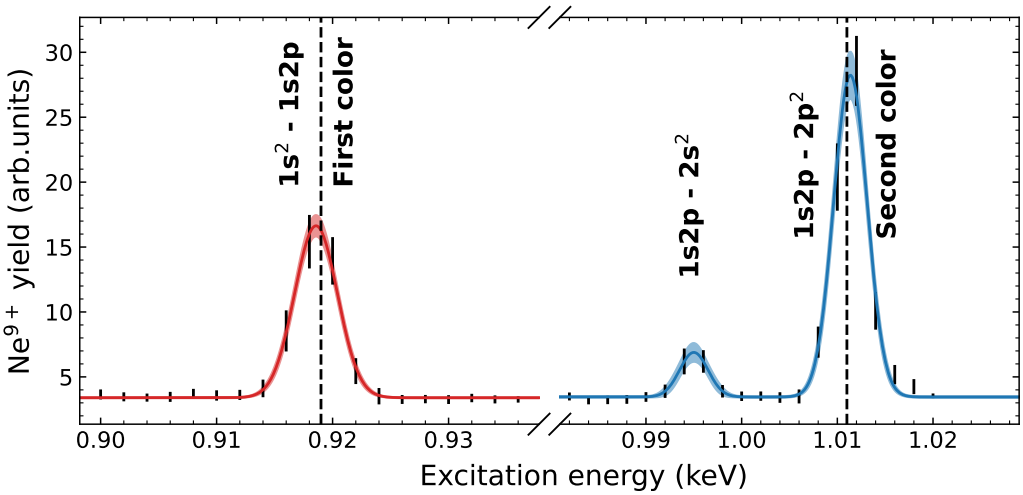

Figure 3.11. *We apply the DCH detection scheme by scanning one of the two XFEL colors, while keeping the other fixed on either a SCH or DCH resonance. Left: helium-like neon 1s - 2p resonance detected through the Ne^{9+} yield by scanning the first XFEL color. Second color fixed at approximately 1.01 keV. Right: DCH spectrum following helium-like neon 1s - 2p excitation is recorded by scanning the second XFEL color. First color fixed to neon 1s2p resonance at 0.920 keV.*

Ions are extracted and analyzed in sync with the ten-hertz train repetition rate.

Pump-probe measurement scheme

The XFEL pulse train comes with a repetition rate of 10 Hz with each train containing 400 pairs of pump and probe pulses pulses separated by τ_{delay}. The pump pulses are energetically tuned to selectively populate the $1s2p\,^1P_1$ from the ground state of the helium-like ion.

Concerning the interrogation process, an intuitive probe process might be the photoionization of the excited 2p electron, thereby producing hydrogen-like ions. This process would then be identical to the REMPI process discussed in Chapter 3.1. But making use of the variable gap undulators at SASE3, we can set the probe pulse to an energy different than the pump pulse. By revisiting the discussion on DCH transitions and their effectiveness in ionization, we can also employ a resonant DCH production process to photoionize the excited helium-like ion. Likewise to the REMPI process this one is also applicable as an interrogation mechanism because a DCH transition is only possible if the ion is still excited through the first resonant excitation. Therefore, for long time delays, ions are back in the ground state and become transparent to the probe pulse. The hydrogen-like ions N_H produced during this process work particularly well as a signal for tracking the dynamics as

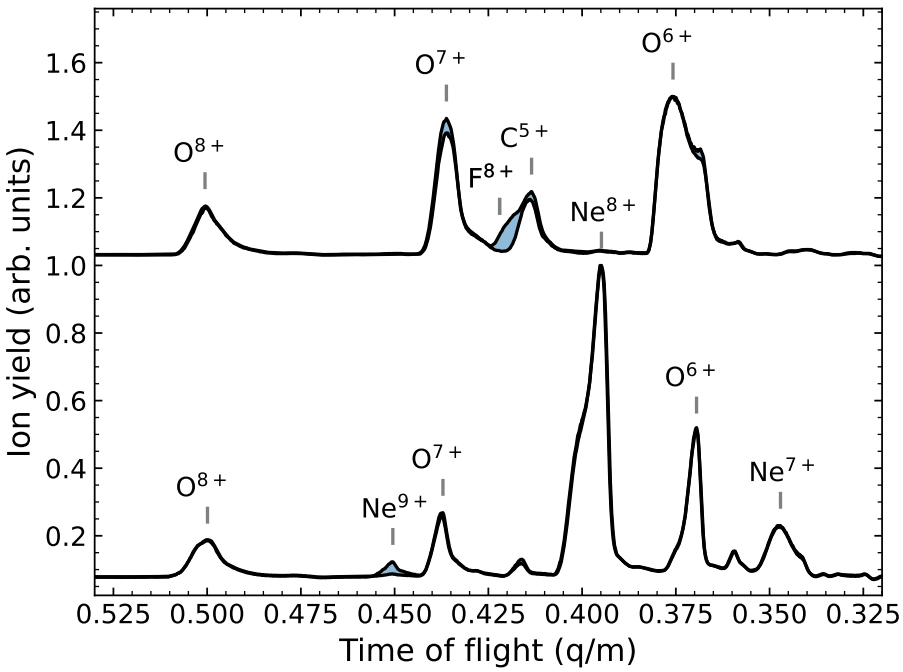

Figure 3.12. *Exemplary traces recorded by the ion ToF spectrometer for neon and fluorine measurements (Top: Fluorine, Bottom: Neon). The additional hydrogen-like fluorine and neon, which appears for short time delays is shaded in blue.*

they are directly proportional to the excited population of the helium-like ions:

$$N_H = \frac{A_{AI}}{A_{total}} \cdot N_{He}|_{excited} \tag{3.12}$$

with the branching ratio following DCH production $A_{AI}/A_{total} \approx 1$, the entire process has a high efficiency.

Zero delay pump probe spectroscopy

To set up the photon energies of the respective pump and probe pulse for maximum efficiency, the time interval between the pump and probe pulses are first fixed to nominal zero. This allows to perform scans of their respective photon energies. To emphasize, our detection signal is the yield of the hydrogen-like ions, which is at its maximum when both resonance conditions for the pump and probe process are fulfilled.

By scanning the first color (photon energy of pump pulse) while recording the hydrogen-like ion yield, we obtain the spectrum shown on the left in Fig. 3.11. This depicts the $1s^2\,{}^1S_0$ to $1s2p\,{}^1P_1$ transition. More interestingly, by scanning the second color (photon energy of probe pulse), we have access to the DCH transitions. Fig. 3.11 shows the two prominent DCH transitions accessible from the excited $1s2p\,{}^1P_1$ level. At approximately 995 eV, we see the 1s2p $^1P_1$ to 2s^2 $^1S_0$ transition. This is a so-called Two-Electron-One-Photon (TEOP) transition as it requires two electrons to change their orbital in order to satisfy conservation

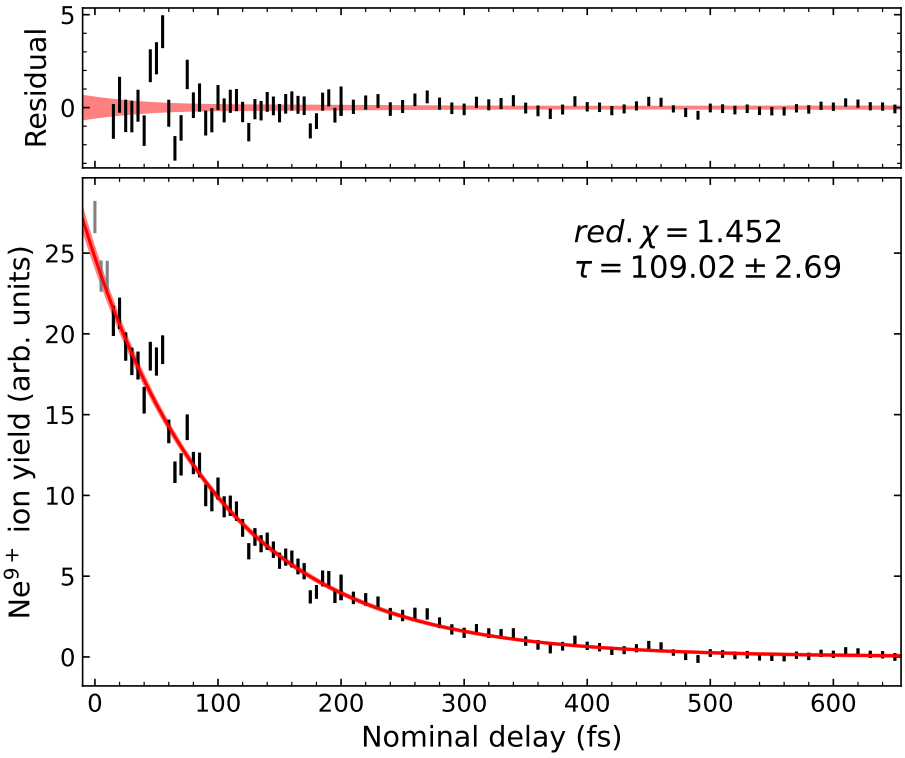

Figure 3.13. *An exemplary measurement showing the recorded H-like neon yield as a function of the nominal delay. Red line depicts an exponential function fitted to the data. Red shaded area indicates the one sigma uncertainty band. Data points below 10 fs are excluded from the fit. Top panel shows residuals and one sigma uncertainty band.*

of angular momentum. At approximately 1010 eV, we see the more prominent 1s2p $^1P_1$ to 2p^2 $^1D_2$ transition, which we use to fix the second color.

Lifetime measurement of the 1s2p $^1P_1$ level

With the two colors fixed at their respective resonances, we perform stepwise adjustments of the delay. To avoid hysteresis in the magnets of the chicane, the delay (and thereby the magnetic field within the chicane) is increased monotonically in discrete steps. At each step of the scan few hundred ion-ToF spectra are recorded (Fig. 3.12). Each datapoint of the ToF trace is associated with an error, which we determine from the standard deviation of those multiple measurements. We take a fixed region-of-interest (ROI) of the photoions in the ion-ToF spectrum (see Fig. 3.12 to determine the photoion yield for the respective time delay.

Decay curves are recorded multiple times per target ion. To determine the lifetime τ, we model the data by means of an exponential function with a constant offset (see Fig. 3.13). Model parameters are estimated by a least-squares minimization fit. From several sets of delay scans, we determine an average lifetime τ_{avg}. Their corresponding uncertainty

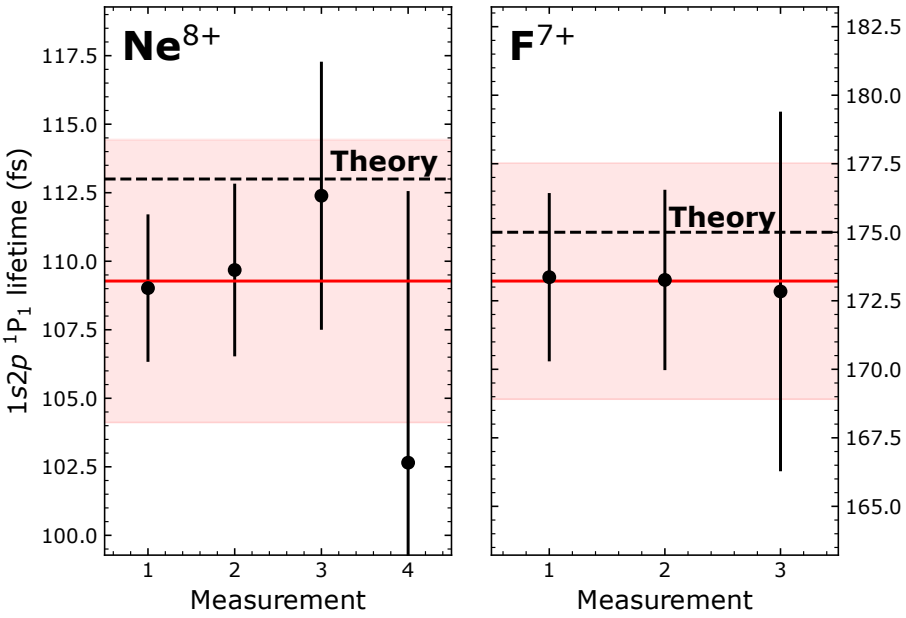

Figure 3.14. *We determine the average from repeated measurements of the 1s2p lifetime for helium-like neon and fluorine (red solid line). Their uncertainty is estimated from the average error of individual measurements (red shaded area). Black dashed lines depict theoretical predictions for neon from Ref. [65] and fluorine, for which we use FAC.*

is estimated from the average statistical uncertainty of all independent measurements (see Fig. 3.14).

Spectral analysis

We extend the spectral model presented in Chapter 3.1 for the pump-probe scheme. An exemplary simulation result for a time delay of 100 fs is shown in Fig. 3.15. The simulation models the population dynamics due to the illumination by the pump pulse (red shaded area in Fig. 3.15), the probe pulse (blue shaded area in Fig. 3.15) and the evolution of the population between the pulses and after the probe pulse. One can see how the exponential decrease of the SCH population, mainly consisting of the 1s2p $^1P_1$ level, (orange dash-dotted line) is stopped by the probe pulse and then partially converted into a population of Hydrogen-like ions (green line). The experimental time-delay measurement can be reproduced by means of the here developed model.

We use following parameters of the XFEL: Pulse duration of 5 fs, photon energy bandwidth of 0.5 %, Intensity of 85 μJ and 15 μJ for the pump and probe pulse, respectively and an estimated focus area of 5x5 μm^2. By simulating the time evolution of the populations at discrete time delays and taking the hydrogen-like ion yield at long time after the probe pulse, we can represent the results as shown in Fig. 3.16. The simulation allows to single out

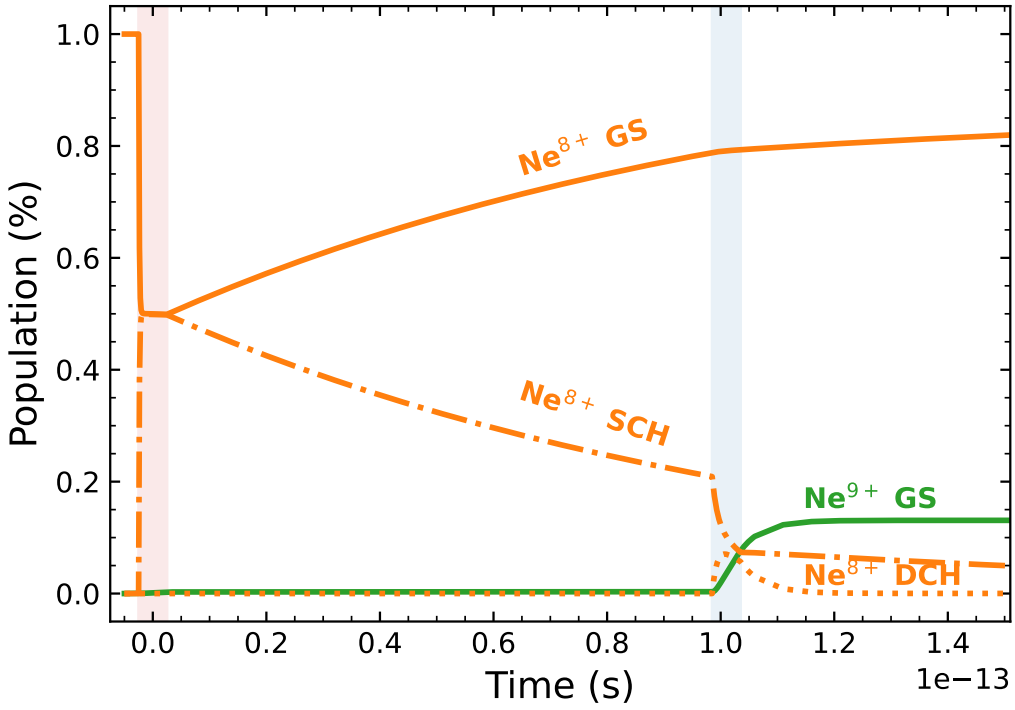

Figure 3.15. *Simulated pump-probe dynamics for a time delay of 100 fs. After an initial excitation by means of the pump pulse, up to 50% of the ground state population (solid orange curve) is excited. The excited SCH population (dash-dotted orange curve) decays back to the GS until the SCH states are interrogated by the probe pulse. The probe pulse populates DCH states (dotted orange curve), which lead to the production of H-like ions (solid green curve).*

contributions of several ionization channels. The dominating contribution comes from the Auger-Meitner decay after resonant production of DCH states (3.1). A noticable contribution originates from the non-resonant photoionization due to the probe pulse (orange shaded area in Fig. 3.16). The more than hundred-fold difference in signal strength, highlights the effectiveness the resonant DCH production as a means to interrogate the ion dynamics. A time-independent, constant offset in the signal is produced by non-resonant photoionization following resonant excitation due to the pump pulse (red area in Fig. 3.16). An increased signal at short time delays can be observed in the simulated spectrum. This coincides with the temporal overlap of the pump and probe pulse, which leads to an increased ionization efficiency.

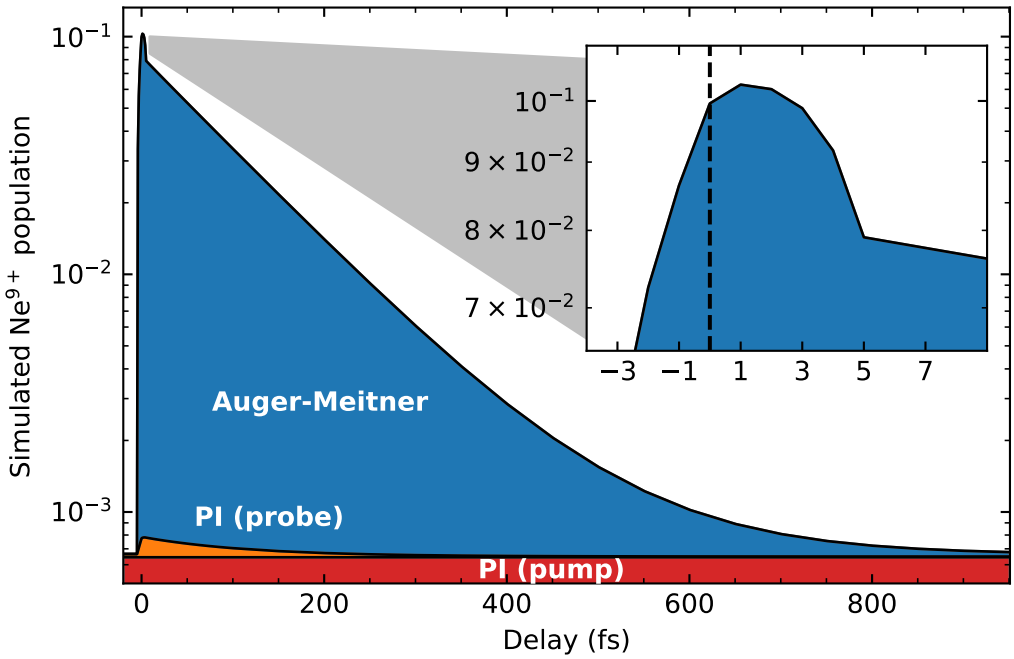

Figure 3.16. *Simulated decay spectrum. The exponential decay of the 1s2p $^1P_1$ state is shown in the population of the hydrogen-like Ne ions. Contributions due to non-resonant photoionization caused during the interrogation process (orange shaded area), as well as the baseline produced by the non-resonant photoionization during the pump process are highlighted (red shaded area). Inset shows the enhanced photo-ion population during temporal overlap of the two pulses.*

Chapter 4

Discussion & Outlook

The three publications in Chapter 2 as well as the two XFEL studies presented in Chapter 3 present various frontiers, where trapped HCI can be studied using synchrotron and XFEL radiation. The insights of this thesis pave the way for further investigations for precision transition energy of singly and multiply excited states and lifetime measurements.
In this chapter, I will discuss the main results of this work also in the context of present and future measurements.

Precision tests of highly charged ions in the soft X-ray regime

The publications presented in Chapters 2.1 and 2.2 address the challenges and issues encountered in spectroscopy using monochromatized soft X-ray synchrotron radiation. With ongoing technical advancements, such as reducing background noise via electron beam ramping, significant improvements in the signal-to-noise ratio of recorded spectra have been achieved (see Ref. [66, 20]). These improvements have led to more accurate centroid determinations of the measured transitions, but they also revealed a substantial discrepancy between the measured and predicted line positions. This mismatch is too large to be explained by either statistical experimental or theoretical uncertainties. We identified that a systematic uncertainty, caused by improper encoder calibrations (Encoder Interpolation Error [22]), is responsible for this discrepancy. A fundamental error, which is, to a certain degree, present in all equipment using rotary encoders. In the two publications, we have addressed this issue by implementing photoelectron spectroscopy downstream of the EBIT experiment to monitor the oscillations introduced by the monochromator encoders to the photon energy. By correcting the photon energy for this error, improvements of more than one order of magnitude in energy determinations have been made. Fig. 4.1 shows the achieved experimental precision $\Delta E/E$ of our work (black crosses) compared to previous investigations by others (black diamonds). As can be seen, our results lie well in the parts-per-million (ppm) accuracy realm. Schlesser *et al.* [11] and Machado *et al.* [15] did achieve even higher precision

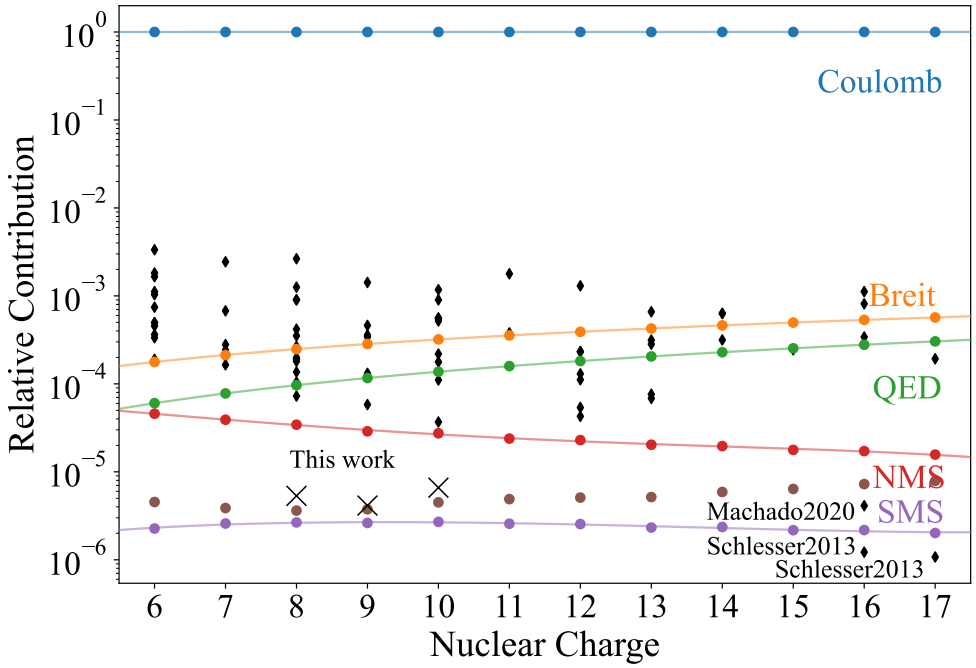

Figure 4.1. *Predicted relative contribution to the 1s2s2p ^2P energy levels of lithium-like HCIs (connected colored dots) in the Dirac Hamiltonian as a function of atomic number [67]. The dominating contributions come from Coulomb interaction (blue dots) independently of the atomic number. All other effects are several orders of magnitudes less significant, but show clear trends as a function of the atomic number. In order for experimental results to be sensitive to a given term in the Hamiltonian, the relative uncertainty $\Delta E/E$ must fall under the value of the relative contribution. The black diamonds depict the relative uncertainty $\Delta E/E$ of published experimental measurements from Ref. [68] and references therein. Results from this work Ref. [26] are marked with black crosses.*

by means of reference-free measurements (see Chapter 1.1.1), but it is important to highlight that their technique is not applicable in the soft X-ray regime below 1 keV due to limited efficiency of the utilized crystal spectrometer. The precision of our results on lithium-like ions are well below the minute contributions of QED, Breit-interaction and normal nuclear mass shift. Unfortunately, the total theoretical uncertainty is still dominated by electronic correlation, which makes it yet not possible to directly test the non-Coulomb contribution terms. Even better experimental results are necessary, an increase in precision by another order of magnitude, would conclusively determine if the tension between experiment and theory is true. Such experimental improvement in accuracy will most likely be feasible with increased measurement time as well as by incorporating high-resolution/-stability voltage sources and more accurate voltmeters at the downstream photoelectron spectrometer to eliminate systematic errors associated with knowledge of the bias voltages. Similar diagnostic approaches of tracking the photon energy have been pursued using a compact grating

spectrometer. This approach looses the advantage of PES offering high photon energy acceptance due to the variable biasing of the target (and thereby offsetting the kinetic energy of the photo electrons.) but due to its simplicity allows for extensive systematic error analysis [69].

Chapter 2.2 addresses experimental and theoretical efforts in another fundamental atomic system. Neon-like iron, with its closed-shell electronic structure, provides an excellent opportunity to showcase the capabilities of high-precision theoretical predictions. With ongoing X-ray satellite mission as XMM-Newton, Chandra and the newly launched XRISM, the study of this ion is also of great interest from an astrophysical perspective, as discussed in Chapter 1.1.2. Doppler velocity based diagnositcs of astrophysical plasma are enabled by reducing the restframe transition energy uncertainty to a corresponding velocity uncertainty of 5 km/s. This reduction of approximate one order of magnitude allows for rigorous testing of all previous calculations, including our own old calculations [66]. A key insight from the theoretical efforts is that predicted energies of the iron lines exhibit a noticeable shift when comparing the current theoretical values with earlier predictions, which were based on a smaller configuration space, even though configurations up to n=17 have been included. This highlights the difficulty in treating electron correlation. Theoretical predictions of transitions between n=2 to n=3 required the inclusion of all possible single and double excitation of more than n=20 to reach satisfactory convergence of the calculations. These issues underline the problems of theoretical treatment of multielectron systems. High-precision measurements are critical to guide these theoretical efforts. However, the benchmarking of the level energies of doubly excited states, which are essential for predicting ground-state transitions, remains a challenge. Additionally, the potential need to include triply excited states and the uncertainty surrounding their impact on configuration interaction calculations are key issues. These topics are addressed in the following discussion.

Probing transient multiply-excited states

Probing multiply excited states with high efficiency is challenging, but the ultrashort, ultraintense X-ray pulses generated by XFELs enable access to these transient states, which cannot be explored using X-ray pulses from storage ring facilities (see Fig. 3.1). In Chapter 3.1, I have presented results of trapped HCIs illuminated by XFEL radiation. In contrast to previous similar experiments [70, 71, 72, 73, 46], we obtain data, where the interpretation is not reliant on large scale calculation involving all, from neutral to highly ionized, charge states. The theoretical analysis is based on coupled differential equations on the basis of atomic structure calculations with the Flexible Atomic Code ([56]), which allows the reproduction of the experimental spectrum. Not only did the model help us to identify the various ionization channels leading to the production of higher charge state beyond the

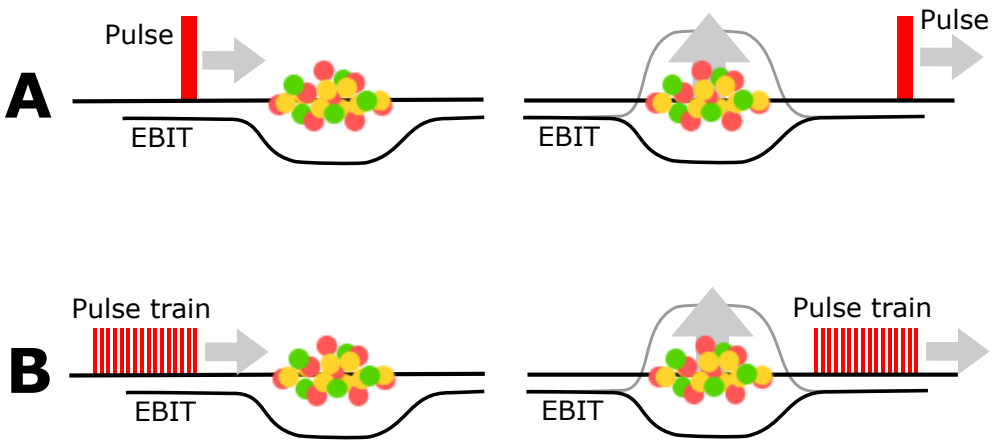

Figure 4.2. *A: The idealized experimental set up. A single XFEL pulses is introduced to the cloud of highly charged ions. After illumination, the ions are ejected from the trap for further charge state analysis. B: Representation of the present measurement scheme. Several hundred XFEL pulses separated by approximately one microsecond illuminate the ion cloud.*

single-photon ionization limit, it also verified that the measured spectrum can be largely explained by a single pulse simulation. Accumulative effects due to the train structure of the incoming XFEL pulses seem to be relatively minor. I.e., the idealized view of the experiment shown in Fig. 4.2 A) is sufficient to fully describe the underlying physics although reality is represented by the more complex train structure of the EuXFEL (see Fig. 4.2 B). Future experiments involving the two-color operation mode at the European XFEL will enable the investigation of resonantly produced triple core-hole states, where the first color produces the double-core hole levels and a second color resonantly produces an additional vacancy. Such investigations combined with proper calibration of the photon energy by means transitions of simple hydrogen or helium-like HCIs would enable valuable atomic data, which is so far non-existent.

Lifetime measurement in the picosecond range

The Hanle effect has been adapted for use in the X-ray regime, achieving experimental uncertainties below ten percent. While this is the first implementation of the soft X-ray Hanle effect and the data quality is not yet ideal, the results are competitive and, in some cases, even surpass the accuracy of lifetime measurements obtained through beam-foil spectroscopy. The limitations of beam-foil spectroscopy are discussed in Chapter 1.2.3, with the primary technical constraint being the ability to perform reliable micrometer-scale translations of the foil. In contrast, the precision of lifetime measurements using the soft X-ray Hanle effect is limited by the precision of the magnetic field characterization in the EBIT and the statistical quality of the data. The implementation of dedicated diagnostics for the

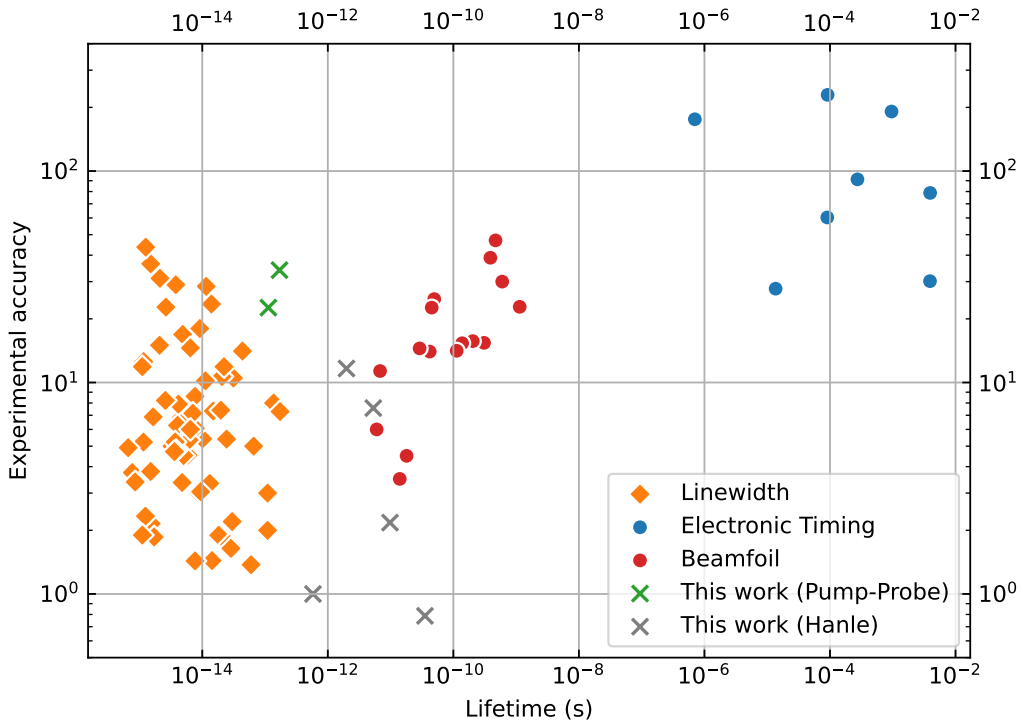

Figure 4.3. *A compilation of lifetime measurements of X-ray transitions by means of electronic timing (blue dots), beamfoil spectroscopy (red dots) and natural linewidth measurements (orange diamonds). Green cross depicts the results from X-ray pump-probe measurements. Grey cross depicts the results by means of Soft-Xray Hanle effect.*

polarization degree of the incident radiation would further reduce potential sources of systematic error. For magnetic sublevels that are nearly degenerate, such as in the case of the 1s2p $^1P_1$ level, acquiring high-quality data requires a significant amount of time. Repeating and extending this technique at high-flux synchrotron radiation facilities, such as PETRA III at DESY, could help address this challenge. But ultimately it is yet difficult to claim a definite time range, where the soft X-ray Hanle effect is best applied. More studies are needed for this very promising, novel approach of lifetime measurements.

Lifetime measurement in the femtosecond range

In Chapter 3.2, an all X-ray pump-probe experiment has been established to measure lifetimes of E1 transitions in X-rays. We have demonstrated that the excellent total temporal resolution offered by the two-color operation mode allows to resolve atomic lifetimes of fast decaying E1 transtions in the soft X-rays. Other established techniques e.g. an X–ray pump and optical probe set-up are known to be limited by the temporal jitter of the two independent laser sources and would therefore be more challenging. The here measured lifetimes lie in a time window, which can be hardly probed by other techniques as for ex-

ample linewidth measurements 1.2.1 and beamfoil spectroscopy 1.2.3. Fig. 4.3 shows our achieved experimental accuracy in comparison with other methods and their respective accuracy. It highlights that the accuracy of linewidth and beamfoil measurements significantly declines as one approaches the femtosecond timescale. In contrast, our X-ray pump-probe scheme excels in this domain, offering promising prospects for even more precise measurements in the future. Upcoming developments at EuXFEL will also commission an optical chicane to allow zero crossing of the X-ray pump and probe pulses. This will increase data quality and therefore decrease lifetime uncertainty. Furthermore, by employing the two-color mode at the SASE2 undulator would make the 5-25 keV range accessible, allowing investigations of lifetimes in the 1 - 10 fs range, which have been measured by Rudolph *et al.* [28] by means of linewidth measurements but with improved precision provided by the pump-probe scheme.

Future prospects

Implementing a pulsed gas injection system synchronized with the 10 Hz repetition rate of the XFEL would enhance the charge-state distribution in the EBIT. Additionally, incorporating a grating spectrometer or, ideally, a microcalorimeter for improved fluorescence diagnostics would further refine the experimental setup. With recent advancements at SQS, including the implementation of a variable polarization undulator, this setup could be further enhanced. By combining it with the Hanle effect, it would be possible to resolve the coherent beating of magnetic sublevels in real time. These are just a few of the potential experimental investigations that could build upon the foundational work presented in this thesis.

Chapter 5

Summary

A physicist is just an atom's way of looking at itself.

Niels Bohr

This cumulative thesis summarizes the work that was done in the years between 2021 and 2024, starting with the idea to employ an Electron Beam Ion Trap at the European XFEL to facilitate studies on highly charged ions with ultraintense and ultrafast X-ray pulses. Within this collaborative effort between the European XFEL and the Max-Planck Institute for Nuclear Physics, I have constructed a new Electron Beam Ion Trap of the Heidelberg Compact EBIT design with few additional changes in design due existing spatial and technical constraints. This instrument has been integrated into the infrastructure at European XFEL, specifically the Small Quantum System Instrument [74]. These efforts culminated in two successful experiments performed with the new EBIT (Chapter 3):

- An investigation of multiply excited states in highly-charged krypton has been performed with ultrahigh intensity XFEL radiation. The production of two electron vacancies in the inner shell of the HCI was enabled by an accidental degeneracy of several resonant transitions, allowing the production of multiply excited states at a single photon energy. This unique feature of krypton has been exploited to study various ionization channels revealing sequential ionization pathways involving up to six photons.

- By utilizing the novel two-color operation mode at European XFEL, another experiment has been conducted to measure femtosecond-long lifetimes of singly excited highly charged oxygen and fluorine. Lifetimes have been determined with few femtosecond uncertainty, resulting in a relative uncertainty of a few percent in excellent agreement with theoretical predictions. Such precision is unprecedented in this investigated time and energy range. The developed measurement scheme, based on the

established pump-probe technique, is broadly applicable and holds promise for future investigations.

The EBIT is now a fully commissioned part of the SQS instrument, providing research groups worldwide with the opportunity to propose ideas for further experiments and to conduct a measurement campaign using it.
Parallel efforts at other synchrotron radiation sources, such as PETRA III, ELETTRA, and SPRING8 have been pursued with EBITs of similar design. Precision measurements of transition energies and lifetimes have been achieved in the framework of this thesis.

- A systematic error generally effecting monochromator based X-ray absorption spectroscopy at synchrotron radiation facilities has been addressed. The so called encoder interpolation error causes minute oscillations of the incident photon energy [22]. It introduces a systematic uncertainty to transition energy determinations if not corrected for. We track this with an additional photon energy diagnostic chamber downstream of the EBIT experiment. Implementing such extention to the established precision X-ray absorption spectroscopy technique, spectroscopic accuracy has been improved by at least one order of magnitude. This has been demonstrated for light lithium-like ions, where we reached experimental precision comparable to current *ab initio* predictions.

- Furthermore, this technique has been employed to measure the prominent 3C and 3D soft X-ray lines of Fe^{16+}, which are crucial diagnostic lines in astrophysical plasma. This application has led to an improvement in energy determination by one order of magnitude. The improved energy determination has enabled the benchmarking of large-scale, high-precision theoretical calculations, allowing for tests of QED contributions to the involved energy levels. The excellent agreement between theory and experiment boosts confidence in predicting energy levels in systems lacking experimental data, with wide-ranging applications in astrophysics, plasma physics, and atomic clock development.

- Finally, a novel lifetime measurement method based on the Hanle-effect has been successfully demonstrated in the theoretically well-predictable helium-like nitrogen. We have demonstrated the feasibility of the soft X-ray Hanle effect for lifetime determination across three orders of magnitude, ranging from hundreds of femtoseconds to tens of picoseconds. Future measurement campaigns targeting more complex ions will offer valuable tests of theory in a time range so far scarcely investigated.

Appendix A

Full publication list of the author

Journal Articles

[1] **Togawa, Moto**, Steffen Kühn, Chintan. Shah, Pedro Amaro, Rene Steinbrügge, Jacob Stierhof, Natalie Hell, Michael Rosner, Keisuke Fujii, Michael Bissinger, Ralf Ballhausen, Moritz Hoesch, Joern Seltmann, SungNam Park, Filipe Grilo, F. Scott Porter, J. P. Santos, Moses Chung, Thomas Stöhlker, Joern Wilms, Thomas Pfeifer, Greg Brown, Maurice A. Leutenegger, Sonja Bernitt, and José R. Crespo López-Urrutia. "Observation of strong two-electron–one-photon transitions in few-electron ions". In: *Phys. Rev. A* 102 (5 Nov. 2020), p. 052831. DOI: 10.1103/PhysRevA.102.052831. URL: https://link.aps.org/doi/10.1103/PhysRevA.102.052831.

[2] **Togawa, Moto**, Steffen Kühn, Chintan Shah, Vladimir A. Zaytsev, Natalia S. Oreshkina, Jens Buck, Sonja Bernitt, René Steinbrügge, Jörn Seltmann, Moritz Hoesch, Christoph H. Keitel, Thomas Pfeifer, Maurice A. Leutenegger, and José R. Crespo López-Urrutia. "High-accuracy measurements of core-excited transitions in light Li-like ions". In: *Phys. Rev. A* 110 (3 Sept. 2024), p. L030802. DOI: 10.1103/PhysRevA.110.L030802. URL: https://link.aps.org/doi/10.1103/PhysRevA.110.L030802.

[3] **Togawa, Moto**, Jan Richter, Chintan Shah, Marc Botz, Joshua Nenninger, Jonas Danisch, Joschka Goes, Steffen Kühn, Pedro Amaro, Awad Mohamed, Yuki Amano, Stefano Orlando, Roberta Totani, Monica de Simone, Stephan Fritzsche, Thomas Pfeifer, Marcello Coreno, Andrey Surzhykov, and José R. Crespo López-Urrutia. "Hanle effect for lifetime determinations in the soft X-ray regime". In: *Physical review letters* (2024). arXiv: 2408.12227 [physics.atom-ph]. URL: https://arxiv.org/abs/2408.12227.

[4] Chintan Shah, **Togawa, Moto**, Marc Botz, Jonas Danisch, Joschka J. Goes, Sonja Bernitt, Marleen Maxton, Kai Köbnick, Jens Buck, Jörn Seltmann, Moritz Hoesch, Ming Feng Gu, F. Scott Porter, Thomas Pfeifer, Maurice A. Leutenegger, Charles Cheung, Marianna S. Safronova, and José R. Crespo López-Urrutia. "High-precision Transition Energy Measurements of Neon-like Fe xvii Ions". In: *The Astrophysical Journal* 969.1 (June 2024), p. 52. DOI: 10.3847/1538-4357/ad454b. URL: https://dx.doi.org/10.3847/1538-4357/ad454b.

[5] René Steinbrügge, Steffen Kühn, Fabrizio Nicastro, Ming Feng Gu, **Togawa, Moto**, Moritz Hoesch, Jörn Seltmann, Ilya Sergeev, Florian Trinter, Sonja Bernitt, et al. "X-Ray Photoabsorption of Density-sensitive Metastable States in Ne VII, Fe XXII, and Fe XXIII". In: *The Astrophysical Journal* 941.2 (2022), p. 188. DOI: 10.3847/1538-4357/ac9c00.

[6] Steffen Kühn, Chintan Shah, José R Crespo López-Urrutia, Keisuke Fujii, René Steinbrügge, Jakob Stierhof, **Togawa, Moto**, Zoltán Harman, Natalia S Oreshkina, Charles Cheung, et al. "High resolution photoexcitation measurements exacerbate the long-standing Fe XVII oscillator strength problem". In: *Physical review letters* 124.22 (2020), p. 225001. DOI: 10.1103/PhysRevLett.124.225001.

[7] Steffen Kühn, Charles Cheung, Natalia S Oreshkina, René Steinbrügge, **Togawa, Moto**, Sonja Bernitt, Lukas Berger, Jens Buck, Moritz Hoesch, Jörn Seltmann, et al. "New measurement resolves key astrophysical Fe XVII oscillator strength problem". In: *Physical review letters* 129.24 (2022), p. 245001. DOI: 10.1103/PhysRevLett.129.245001.

[8] Chintan Shah, Steffen Kühn, Sonja Bernitt, René Steinbrügge, **Togawa, Moto**, Lukas Berger, Jens Buck, Moritz Hoesch, Jörn Seltmann, Mikhail G. Kozlov, Sergey G. Porsev, Ming Feng Gu, F. Scott Porter, Thomas Pfeifer, Maurice A. Leutenegger, Charles Cheung, Marianna S. Safronova, and José R. Crespo López-Urrutia. "Natural-linewidth measurements of the $3C$ and $3D$ soft-x-ray transitions in Ni xix". In: *Phys. Rev. A* 109 (6 June 2024), p. 063108. DOI: 10.1103/PhysRevA.109.063108. URL: https://link.aps.org/doi/10.1103/PhysRevA.109.063108.

Conference Papers

[9] Moritz Hoesch, Jörn Seltmann, Florian Trinter, Steffen Kühn, **Togawa, Moto**, René Steinbrügge, Sonja Bernitt, and José R Crespo López-Urrutia. "Highly Charged Ions for High-Resolution Soft X-ray Grating Monochromator Optimisation". In: *Journal of Physics: Conference Series*. Vol. 2380. 1. IOP Publishing. 2022, p. 012086. DOI: 10.3847/1538-4357/ac9c00.

Bibliography

[1] Joseph Fraunhofer. Bestimmung des brechungs-und des farbenzerstreungs-vermögens verschiedener glasarten, in bezug auf die vervollkommnung achromatischer fernröhre. *Annalen der Physik*, 56(7):264–313, 1817. URL: https://doi.org/10.1002/andp.18170560706.

[2] G. Kirchhoff and R. Bunsen. Chemische analyse durch spectralbeobachtungen. *Annalen der Physik*, 186(6):161–189, 1860. DOI: https://doi.org/10.1002/andp.18601860602. eprint: https://onlinelibrary.wiley.com/doi/pdf/10.1002/andp.18601860602. URL: https://onlinelibrary.wiley.com/doi/abs/10.1002/andp.18601860602.

[3] JR Crespo López-Urrutia. The very hot periodic table, 2024. URL: https://www.physi.uni-heidelberg.de/Veranstaltungen/Vortraege/Abstract%5C_Crespo.pdf. Accessed: 2024-10-10.

[4] Polydore Swings. Edlén's identification of the coronal lines with forbidden lines of fe x, xi, xiii, xiv, xv; ni xii, xiii, xv, xvi; ca xii, xiii, xv; ax, xiv. *Astrophysical Journal*, 98, 1943. URL: https://adsabs.harvard.edu/full/1943ApJ....98..116S.

[5] A. Gumberidze, Th. Stöhlker, D. Bana ś, K. Beckert, P. Beller, H. F. Beyer, F. Bosch, S. Hagmann, C. Kozhuharov, D. Liesen, F. Nolden, X. Ma, P. H. Mokler, M. Steck, D. Sierpowski, and S. Tashenov. Quantum electrodynamics in strong electric fields: the ground-state lamb shift in hydrogenlike uranium. *Phys. Rev. Lett.*, 94:223001, 22, June 2005. DOI: 10.1103/PhysRevLett.94.223001. URL: https://link.aps.org/doi/10.1103/PhysRevLett.94.223001.

[6] P. Beiersdorfer, H. Chen, D. B. Thorn, and E. Träbert. Measurement of the two-loop lamb shift in lithiumlike U^{89+}. *Phys. Rev. Lett.*, 95:233003, 23, December 2005. DOI: 10.1103/PhysRevLett.95.233003. URL: https://link.aps.org/doi/10.1103/PhysRevLett.95.233003.

[7] R Loetzsch, HF Beyer, L Duval, U Spillmann, D Banaś, P Dergham, FM Kröger, J Glorius, RE Grisenti, M Guerra, et al. Testing quantum electrodynamics in extreme

fields using helium-like uranium. *Nature*, 625(7996):673–678, 2024. URL: https://doi.org/10.1038/s41586-023-06910-y.

[8] J Morgner, B Tu, CM König, T Sailer, F Heiße, H Bekker, B Sikora, C Lyu, VA Yerokhin, Z Harman, et al. Stringent test of qed with hydrogen-like tin. *Nature*, 622(7981):53–57, 2023. URL: https://doi.org/10.1038/s41586-023-06453-2.

[9] J. Suleiman, H. G. Berry, R. W. Dunford, R. D. Deslattes, and P. Indelicato. Observations of doubly excited states in lithiumlike calcium. *Phys. Rev. A*, 49:156–160, 1, January 1994. DOI: 10.1103/PhysRevA.49.156. URL: https://link.aps.org/doi/10.1103/PhysRevA.49.156.

[10] Kunihiro Shima, Noriyoshi Kuno, Mikio Yamanouchi, and Hiroyuki Tawara. Equilibrium charge fractions of ions of z = 4–92 emerging from a carbon foil. *Atomic Data and Nuclear Data Tables*, 51(2):173–241, 1992. ISSN: 0092-640X. DOI: https://doi.org/10.1016/0092-640X(92)90001-X. URL: https://www.sciencedirect.com/science/article/pii/0092640X9290001X.

[11] S. Schlesser, S. Boucard, D. S. Covita, J. M. F. dos Santos, H. Fuhrmann, D. Gotta, A. Gruber, M. Hennebach, A. Hirtl, P. Indelicato, E.-O. Le Bigot, L. M. Simons, L. Stingelin, M. Trassinelli, J. F. C. A. Veloso, A. Wasser, and J. Zmeskal. High-accuracy x-ray line standards in the 3-kev region. *Phys. Rev. A*, 88:022503, 2, August 2013. DOI: 10.1103/PhysRevA.88.022503. URL: https://link.aps.org/doi/10.1103/PhysRevA.88.022503.

[12] K Kubicek, J Braun, H Bruhns, JR Crespo López-Urrutia, PH Mokler, and J Ullrich. High-precision laser-assisted absolute determination of x-ray diffraction angles. *Review of Scientific Instruments*, 83(1), 2012.

[13] W. L. Bond. Precision lattice constant determination. *Acta Crystallographica*, 13(10):814–818, October 1960. DOI: 10.1107/S0365110X60001941. URL: https://doi.org/10.1107/S0365110X60001941.

[14] P. Amaro, C.I. Szabo, S. Schlesser, A. Gumberidze, E.G. Kessler, A. Henins, E.O. Le Bigot, M. Trassinelli, J.M. Isac, P. Travers, M. Guerra, J.P. Santos, and P. Indelicato. A vacuum double-crystal spectrometer for reference-free x-ray spectroscopy of highly charged ions. *Radiation Physics and Chemistry*, 98:132–149, 2014. ISSN: 0969-806X. DOI: https://doi.org/10.1016/j.radphyschem.2014.01.015. URL: https://www.sciencedirect.com/science/article/pii/S0969806X1400019X.

[15] J. Machado, Guojie Bian, Nancy Paul, M. Trassinelli, P. Amaro, M. Guerra, C. I. Szabo, A. Gumberidze, J. M. Isac, J. P. Santos, J. P. Desclaux, and P. Indelicato. Reference-free measurements of the $1s2s2p\,^2P^o_{1/2,3/2} \rightarrow 1s^2 2s\,^2S_{1/2}$ and $1s2s2p\,^4P_{5/2} \rightarrow 1s^2 2s\,^2S_{1/2}$ transition energies and widths in lithiumlike sulfur and argon ions. *Phys. Rev. A*, 101:062505, 6, June 2020. DOI: 10.1103/PhysRevA.101.062505. URL: https://link.aps.org/doi/10.1103/PhysRevA.101.062505.

[16] S. W. Epp, J. R. Crespo López-Urrutia, G. Brenner, V. Mäckel, P. H. Mokler, R. Treusch, M. Kuhlmann, M. V. Yurkov, J. Feldhaus, J. R. Schneider, M. Wellhöfer, M. Martins, W. Wurth, and J. Ullrich. Soft x-ray laser spectroscopy on trapped highly charged ions at flash. *Phys. Rev. Lett.*, 98:183001, 18, May 2007. DOI: 10.1103/PhysRevLett.98.183001. URL: https://link.aps.org/doi/10.1103/PhysRevLett.98.183001.

[17] MA Leutenegger, Steffen Kühn, P Micke, R Steinbrügge, Jakob Stierhof, Chintan Shah, N Hell, M Bissinger, M Hirsch, R Ballhausen, et al. High-precision determination of oxygen k α transition energy excludes incongruent motion of interstellar oxygen. *Physical review letters*, 125(24):243001, 2020. URL: https://link.aps.org/doi/10.1103/PhysRevLett.125.243001.

[18] Moto Togawa, Steffen Kühn, Chintan Shah, Pedro Amaro, René Steinbrügge, Jakob Stierhof, Natalie Hell, Michael Rosner, Keisuke Fujii, Matthias Bissinger, et al. Observation of strong two-electron–one-photon transitions in few-electron ions. *Physical Review A*, 102(5):052831, 2020. URL: https://link.aps.org/doi/10.1103/PhysRevA.102.052831.

[19] Moritz Hoesch, Jörn Seltmann, Florian Trinter, Steffen Kühn, **Togawa, Moto**, René Steinbrügge, Sonja Bernitt, and José R Crespo López-Urrutia. Highly charged ions for high-resolution soft x-ray grating monochromator optimisation. In *Journal of Physics: Conference Series*, volume 2380 of number 1, page 012086. IOP Publishing, 2022.

[20] Steffen Kühn, Charles Cheung, Natalia S Oreshkina, René Steinbrügge, Moto Togawa, Sonja Bernitt, Lukas Berger, Jens Buck, Moritz Hoesch, Jörn Seltmann, et al. New measurement resolves key astrophysical fe xvii oscillator strength problem. *Physical review letters*, 129(24):245001, 2022. DOI: 10.1103/PhysRevLett.129.245001.

[21] Chintan Shah, Steffen Kühn, Sonja Bernitt, René Steinbrügge, **Togawa, Moto**, Lukas Berger, Jens Buck, Moritz Hoesch, Jörn Seltmann, Mikhail G. Kozlov, Sergey G. Porsev, Ming Feng Gu, F. Scott Porter, Thomas Pfeifer, Maurice A. Leutenegger, Charles Cheung, Marianna S. Safronova, and José R. Crespo López-Urrutia. Natural-

linewidth measurements of the $3C$ and $3D$ soft-x-ray transitions in ni xix. *Phys. Rev. A*, 109:063108, 6, June 2024. DOI: 10.1103/PhysRevA.109.063108. URL: https://link.aps.org/doi/10.1103/PhysRevA.109.063108.

[22] Rolf Follath and Andreas Balzer. Heydemann Algorithm for Energy Scale Linearisation. In R. Garrett, I. Gentle, K. Nugent, and S. Wilkins, editors, *Sri 2009, 10th International Conference on Synchrotron Radiation Instrumentation*, volume 1234 of *American Institute of Physics Conference Series*, pages 657–660. AIP, June 2010. DOI: 10.1063/1.3463292.

[23] J. Krempaský, R. Follath, V. N. Strocov, T. Schmitt, and U. Flechsig. Heydemann interpolation correction for energy linearization of soft x-ray monochromators. In *Society of Photo-Optical Instrumentation Engineers (SPIE) Conference Series*, volume 8139 of *Society of Photo-Optical Instrumentation Engineers (SPIE) Conference Series*, 81390K, 81390K, September 2011. DOI: 10.1117/12.893464.

[24] Chintan Shah, **Togawa, Moto**, Marc Botz, Jonas Danisch, Joschka J. Goes, Sonja Bernitt, Marleen Maxton, Kai Köbnick, Jens Buck, Jörn Seltmann, Moritz Hoesch, Ming Feng Gu, F. Scott Porter, Thomas Pfeifer, Maurice A. Leutenegger, Charles Cheung, Marianna S. Safronova, and José R. Crespo López-Urrutia. High-precision transition energy measurements of neon-like fe xvii ions. *The Astrophysical Journal*, 969(1):52, June 2024. DOI: 10.3847/1538-4357/ad454b. URL: https://dx.doi.org/10.3847/1538-4357/ad454b.

[25] René Steinbrügge, Steffen Kühn, Fabrizio Nicastro, Ming Feng Gu, **Togawa, Moto**, Moritz Hoesch, Jörn Seltmann, Ilya Sergeev, Florian Trinter, Sonja Bernitt, et al. X-ray photoabsorption of density-sensitive metastable states in ne vii, fe xxii, and fe xxiii. *The Astrophysical Journal*, 941(2):188, 2022. DOI: 10.3847/1538-4357/ac9c00.

[26] Moto Togawa, Steffen Kühn, Chintan Shah, Vladimir A. Zaytsev, Natalia S. Oreshkina, Jens Buck, Sonja Bernitt, René Steinbrügge, Jörn Seltmann, Moritz Hoesch, Christoph H. Keitel, Thomas Pfeifer, Maurice A. Leutenegger, and José R. Crespo López-Urrutia. High-accuracy measurements of core-excited transitions in light li-like ions. *Phys. Rev. A*, 110:L030802, 3, September 2024. DOI: 10.1103/PhysRevA.110.L030802. URL: https://link.aps.org/doi/10.1103/PhysRevA.110.L030802.

[27] P Beiersdorfer, AL Osterheld, V Decaux, and K Widmann. Observation of lifetime-limited x-ray linewidths in cold highly charged ions. *Physical review letters*, 77(27):5353, 1996. URL: https://link.aps.org/doi/10.1103/PhysRevLett.77.5353.

[28] JK Rudolph, S Bernitt, SW Epp, R Steinbr, C Beilmann, GV Brown, S Eberle, A Graf, Z Harman, N Hell, et al. Jr crespo l. opez-urrutia. *Phys. Rev. Lett*, 111(10):103002, 2013. URL: https://link.aps.org/doi/10.1103/PhysRevLett.111.103002.

[29] Naoki Kimura, Yoshiki Miya, Daiki Ito, Daiji Kato, Masaaki Baba, Susumu Kuma, Toshiyuki Azuma, Nobuyuki Nakamura, et al. Laboratory transition-rate measurement of the coronal intercombination line of ar xv by time-resolved laser spectroscopy. *The Astrophysical Journal*, 972(1):12, 2024. URL: https://iopscience.iop.org/article/10.3847/1538-4357/ad643e.

[30] Gunter Brenner, JR Crespo López-Urrutia, Sven Bernitt, Daniel Fischer, Rainer Ginzel, K Kubiček, V Mäckel, Paul H Mokler, Martin C Simon, and J Ullrich. On the transition rate of the fe x red coronal line. *The Astrophysical Journal*, 703(1):68, 2009. DOI: 10.1088/0004-637X/703/1/68.

[31] PA Neill, E Träbert, P Beiersdorfer, GV Brown, CL Harris, SB Utter, and KL Wong. Improved electron-beam ion-trap lifetime measurement of the 1s2s 3s1 level in n5+ and f7+. *Physica Scripta*, 62(2-3):141, 2000. DOI: 10.1238/Physica.Regular.062a00141.

[32] JR Crespo López-Urrutia, P Beiersdorfer, Daniel Wolf Savin, and K Widmann. Precision measurement of the lifetime of the 1 s 2 s 3 s 1 metastable level in heliumlike o 6+. *Physical Review A*, 58(1):238, 1998. DOI: 10.1103/PhysRevA.58.238.

[33] BJ Wargelin, P Beiersdorfer, and SM Kahn. Radiative lifetime of the long-lived 1s2s 3 s 1 state in heliumlike neon by electron-beam excitation of trapped ions. *Physical review letters*, 71(14):2196, 1993. DOI: 10.1103/PhysRevLett.71.2196.

[34] E Träbert, P Beiersdorfer, GV Brown, AJ Smith, SB Utter, MF Gu, and Daniel Wolf Savin. Improved electron-beam ion-trap lifetime measurement of the ne 8+ 1 s 2 s 3 s 1 level. *Physical Review A*, 60(3):2034, 1999. DOI: 10.1103/PhysRevA.60.2034.

[35] GS Stefanelli, P Beiersdorfer, V Decaux, and K Widmann. Measurement of the radiative lifetime of the 1s2s 3 s 1 level in heliumlike magnesium. *Physical Review A*, 52(5):3651, 1995. DOI: 10.1103/PhysRevA.52.3651.

[36] JR Crespo López-Urrutia, P Beiersdorfer, and K Widmann. Lifetime of the 1 s 2 s s 1 3 metastable level in he-like s 14+ measured with an electron beam ion trap. *Physical Review A—Atomic, Molecular, and Optical Physics*, 74(1):012507, 2006. DOI: 10.1103/PhysRevA.74.012507.

[37] Elmar Träbert. On atomic lifetimes and environmental density. *Atoms*, 10(4), 2022. ISSN: 2218-2004. DOI: 10.3390/atoms10040114. URL: https://www.mdpi.com/2218-2004/10/4/114.

[38] Ahmed H Zewail. Femtochemistry. *The Journal of Physical Chemistry*, 97(48):12427–12446, 1993. DOI: https://doi.org/10.1021/j100150a001.

[39] Ahmed H Zewail. Femtochemistry: atomic-scale dynamics of the chemical bond. *The Journal of Physical Chemistry A*, 104(24):5660–5694, 2000. DOI: https://doi.org/10.1021/jp001460h.

[40] Shuai Li, Lixin Lu, Swarnendu Bhattacharyya, Carolyn Pearce, Kai Li, Emily T. Nienhuis, Gilles Doumy, R. D. Schaller, S. Moeller, M.-F. Lin, G. Dakovski, D. J. Hoffman, D. Garratt, Kirk A. Larsen, J. D. Koralek, C. Y. Hampton, D. Cesar, Joseph Duris, Z. Zhang, Nicholas Sudar, James P. Cryan, A. Marinelli, Xiaosong Li, Ludger Inhester, Robin Santra, and Linda Young. Attosecond-pump attosecond-probe x-ray spectroscopy of liquid water. *Science*, 383(6687):1118–1122, 2024. DOI: 10.1126/science.adn6059. eprint: https://www.science.org/doi/pdf/10.1126/science.adn6059. URL: https://www.science.org/doi/abs/10.1126/science.adn6059.

[41] Zhaoheng Guo, Taran Driver, Sandra Beauvarlet, David Cesar, Joseph Duris, Paris L Franz, Oliver Alexander, Dorian Bohler, Christoph Bostedt, Vitali Averbukh, et al. Experimental demonstration of attosecond pump–probe spectroscopy with an x-ray free-electron laser. *Nature Photonics*:1–7, 2024. DOI: https://doi.org/10.1038/s41566-024-01419-w.

[42] Robert Williams Wood and Alexander Ellett. On the influence of magnetic fields on the polarisation of resonance radiation. *Proceedings of the Royal Society of London. Series A, Containing Papers of a Mathematical and Physical Character*, 103(722):396–403, 1923. DOI: https://doi.org/10.1098/rspa.1923.0065.

[43] RW Wood. Lxvii. selective reflexion, scattering and absorption by resonating gas molecules. *The London, Edinburgh, and Dublin Philosophical Magazine and Journal of Science*, 23(137):689–714, 1912. DOI: https://doi.org/10.1080/14786440508637267.

[44] Robert John Strutt. Polarisation of the light scattered by mercury vapour near the resonance periodicity. *Proceedings of the Royal Society of London. Series A, Containing Papers of a Mathematical and Physical Character*, 102(715):190–196, 1922. DOI: https://doi.org/10.1098/rspa.1922.0080.

[45] Robin Santra and Linda Young. Interaction of intense x-ray beams with atoms. *Synchrotron Light Sources and Free-Electron Lasers: Accelerator Physics, Instrumentation and Science Applications*:1435–1462, 2020. DOI: https://doi.org/10.1007/978-3-319-14394-1_25.

[46] Benedikt Rudek, Koudai Toyota, Lutz Foucar, Benjamin Erk, Rebecca Boll, Cédric Bomme, Jonathan Correa, Sebastian Carron, Sébastien Boutet, Garth J Williams, et al. Relativistic and resonant effects in the ionization of heavy atoms by ultra-intense hard x-rays. *Nature communications*, 9(1):4200, 2018. DOI: https://doi.org/10.1038/s41467-018-06745-6.

[47] Aljoscha Rörig, Sang-Kil Son, Tommaso Mazza, Philipp Schmidt, Thomas M Baumann, Benjamin Erk, Markus Ilchen, Joakim Laksman, Valerija Music, Shashank Pathak, et al. Multiple-core-hole resonance spectroscopy with ultraintense x-ray pulses. *Nature Communications*, 14(1):5738, 2023. DOI: https://doi.org/10.1038/s41467-023-41505-1.

[48] Henry N. Chapman. X-ray free-electron lasers for the structure and dynamics of macromolecules. *Annual Review of Biochemistry*, 88(Volume 88, 2019):35–58, 2019. ISSN: 1545-4509. DOI: https://doi.org/10.1146/annurev-biochem-013118-110744. URL: https://www.annualreviews.org/content/journals/10.1146/annurev-biochem-013118-110744.

[49] Sven Bernitt, GV Brown, Jan K Rudolph, René Steinbrügge, A Graf, M Leutenegger, SW Epp, Sita Eberle, K Kubiček, Volkhard Mäckel, et al. An unexpectedly low oscillator strength as the origin of the fe xvii emission problem. *Nature*, 492(7428):225–228, 2012. DOI: https://doi.org/10.1038/nature11627.

[50] M Altarelli. From third-to fourth-generation light sources: free-electron lasers in the uv and x-ray range. In *Magnetism and Synchrotron Radiation: New Trends*, pages 407–419. Springer, 2010. DOI: https://doi.org/10.1007/978-3-642-04498-4_15.

[51] G Margaritondo and Primoz Rebernik Ribic. A simplified description of x-ray free-electron lasers. *Journal of synchrotron radiation*, 18(2):101–108, 2011. DOI: 10.1107/S090904951004896X.

[52] Jochen R. Schneider. Photon science at accelerator-based light sources. *Reviews of Accelerator Science and Technology*, 03(01):13–37, 2010. DOI: 10.1142/S1793626810000348. eprint: https://doi.org/10.1142/S1793626810000348. URL: https://doi.org/10.1142/S1793626810000348.

[53] N Hell, P Beiersdorfer, GV Brown, ME Eckart, RL Kelley, CA Kilbourne, MA Leutenegger, TE Lockard, FS Porter, and J Wilms. Highly charged ions in a new era of high-resolution X-ray spectroscopy. Technical report, Lawrence Livermore National Lab.(LLNL), Livermore, CA (United States), 2019. DOI: https://doi.org/10.1002/xrs.3107·.

[54] AH Gabriel. Dielectronic satellite spectra for highly-charged helium-like ion lines. *Monthly Notices of the Royal astronomical society*, 160(1):99–119, 1972. DOI: https://doi.org/10.1093/mnras/160.1.99.

[55] Chensheng Wu and Xiang Gao. Change of the relative line strengths due to the resonance induced population transfer between fe xvii and fexvi ions. *Scientific Reports*, 9(1):7463, 2019. DOI: https://doi.org/10.1038/s41598-019-43916-x.

[56] Ming Feng Gu. The flexible atomic code. *Canadian Journal of Physics*, 86(5):675–689, 2008. DOI: https://doi.org/10.1139/p07-197.

[57] Peter Micke, S Kühn, L Buchauer, JR Harries, Thore Mainart Bücking, K Blaum, A Cieluch, A Egl, Daniel Hollain, S Kraemer, et al. The heidelberg compact electron beam ion traps. *Review of Scientific Instruments*, 89(6), 2018. DOI: https://doi.org/10.1063/1.5026961.

[58] Theophilos Maltezopoulos, Florian Dietrich, Wolfgang Freund, Ulf Fini Jastrow, Andreas Koch, Joakim Laksman, Jia Liu, Marc Planas, Andrey A Sorokin, Kai Tiedtke, et al. Operation of x-ray gas monitors at the european xfel. *Journal of synchrotron radiation*, 26(4):1045–1051, 2019. DOI: https://doi.org/10.1107/S1600577519003795.

[59] Andrey A Sorokin, Yilmaz Bican, Susanne Bonfigt, Maciej Brachmanski, Markus Braune, Ulf Fini Jastrow, Alexander Gottwald, Hendrik Kaser, Mathias Richter, and Kai Tiedtke. An x-ray gas monitor for free-electron lasers. *Journal of synchrotron radiation*, 26(4):1092–1100, 2019. DOI: 10.1107/S1600577519005174.

[60] Eiji Shigemasa, Mitsuru Nagasono, Hiroshi Iwayama, James R Harries, and Lisa Ishikawa. Resonance-enhanced three-photon single ionization of ne by ultrashort extreme-ultraviolet pulses. *Journal of Physics B: Atomic, Molecular and Optical Physics*, 46(16):164020, 2013. DOI: 10.1088/0953-4075/46/16/164020.

[61] T. Mazza, M. Ilchen, M. D. Kiselev, E. V. Gryzlova, T. M. Baumann, R. Boll, A. De Fanis, P. Grychtol, J. Montaño, V. Music, Y. Ovcharenko, N. Rennhack, D. E. Rivas, Ph. Schmidt, R. Wagner, P. Ziolkowski, N. Berrah, B. Erk, P. Johnsson, C. Küstner-Wetekam, L. Marder, M. Martins, C. Ott, S. Pathak, T. Pfeifer, D. Rolles, O. Zatsarinny, A. N. Grum-Grzhimailo, and M. Meyer. Mapping resonance structures in transient core-ionized atoms. *Phys. Rev. X*, 10:041056, 4, December 2020. DOI: 10.1103/PhysRevX.10.041056. URL: https://link.aps.org/doi/10.1103/PhysRevX.10.041056.

[62] LS Cederbaum, Francesco Tarantelli, Antonio Sgamellotti, and J Schirmer. On double vacancies in the core. *The Journal of chemical physics*, 85(11):6513–6523, 1986. DOI: https://doi.org/10.1063/1.451432.

[63] Zoltan Jurek, S-K Son, Beata Ziaja, and Robin Santra. Xmdyn and xatom: versatile simulation tools for quantitative modeling of x-ray free-electron laser induced dynamics of matter. *Journal of Applied Crystallography*, 49(3):1048–1056, 2016. DOI: 10.1107/S1600576716006014.

[64] Svitozar Serkez, Winfried Decking, Lars Froehlich, Natalia Gerasimova, Jan Grünert, Marc Guetg, Marko Huttula, Suren Karabekyan, Andreas Koch, Vitali Kocharyan, et al. Opportunities for two-color experiments in the soft x-ray regime at the european xfel. *Applied Sciences*, 10(8):2728, 2020. DOI: https://doi.org/10.3390/app10082728.

[65] I.M. Savukov, W.R. Johnson, and U.I. Safronova. Multipole (e1, m1, e2, m2) transition wavelengths and rates between states with n≤6 in helium-like carbon, nitrogen, oxygen, neon, silicon, and argon. *Atomic Data and Nuclear Data Tables*, 85(1):83–167, 2003. ISSN: 0092-640X. DOI: https://doi.org/10.1016/S0092-640X(03)00056-1. URL: https://www.sciencedirect.com/science/article/pii/S0092640X03000561.

[66] Steffen Kühn, Chintan Shah, José R Crespo López-Urrutia, Keisuke Fujii, René Steinbrügge, Jakob Stierhof, Moto Togawa, Zoltán Harman, Natalia S Oreshkina, Charles Cheung, et al. High resolution photoexcitation measurements exacerbate the long-standing fe xvii oscillator strength problem. *Physical review letters*, 124(22):225001, 2020. URL: https://link.aps.org/doi/10.1103/PhysRevLett.129.245001.

[67] V. A. Yerokhin, A. Surzhykov, and A. Müller. Relativistic configuration-interaction calculations of the energy levels of the $1s^2 2l$ and $1s2l2l'$ states in lithiumlike ions: carbon through chlorine. *Phys. Rev. A*, 96:042505, 4, October 2017. DOI: 10.1103/PhysRevA.96.042505. URL: https://link.aps.org/doi/10.1103/PhysRevA.96.042505.

[68] V.I. Azarov, A. Kramida, and Yu. Ralchenko. A critical compilation of experimental data on the 1s2l2l′ core-excited states of li-like ions from carbon to uranium. *Atomic Data and Nuclear Data Tables*, 149:101548, 2023. ISSN: 0092-640X. DOI: https://doi.org/10.1016/j.adt.2022.101548. URL: https://www.sciencedirect.com/science/article/pii/S0092640X22000481.

[69] J. Danisch. Search for the ^{16}o – ^{18}o isotope shift in the photoionization of be-like oxygen with monochromatic soft x-ray synchrotron radiation. 2024. In preparation.

[70] AA Sorokin, SV Bobashev, T Feigl, K Tiedtke, H Wabnitz, and Mathias Richter. Photoelectric effect at ultrahigh intensities. *Physical review letters*, 99(21):213002, 2007. DOI: 10.1103/PhysRevLett.99.213002.

[71] Linda Young, Elliot P Kanter, Bertold Kraessig, Yongjin Li, AM March, ST Pratt, Robin Santra, SH Southworth, Nina Rohringer, LF DiMauro, et al. Femtosecond electronic response of atoms to ultra-intense x-rays. *Nature*, 466(7302):56–61, 2010. DOI: 10.1038/nature09177.

[72] Laurent Mercadier, A Benediktovitch, C Weninger, MA Blessenohl, S Bernitt, Hendrik Bekker, S Dobrodey, A Sanchez-Gonzalez, B Erk, C Bomme, et al. Evidence of extreme ultraviolet superfluorescence in xenon. *Physical review letters*, 123(2):023201, 2019. DOI: 10.1103/PhysRevLett.123.023201.

[73] Benedikt Rudek, Sang-Kil Son, Lutz Foucar, Sascha W Epp, Benjamin Erk, Robert Hartmann, Marcus Adolph, Robert Andritschke, Andrew Aquila, Nora Berrah, et al. Ultra-efficient ionization of heavy atoms by intense x-ray free-electron laser pulses. *Nature photonics*, 6(12):858–865, 2012. DOI: https://doi.org/10.1038/nphoton.2012.261.

[74] Scientific instrument sqs. https://www.xfel.eu/facility/instruments/sqs/index_eng.html, 2024. Accessed: 2024-10-10.